MgB_2 thin films and Josephson devices

Ph.D. committee:

Chairman
Prof. Dr. D. Feil (University of Twente)

Secretary
Prof. Dr. D. Feil (University of Twente)

Supervisors
Prof. Dr. H. Rogalla (University of Twente)
Prof. Dr. Ing. D.H.A. Blank (University of Twente)

Assistant supervisors
Dr. Ing. A.J.H.M. Rijnders (University of Twente)
Dr. Ir. J.W.M.Hilgenkamp (University of Twente)

Members
Prof. Dr. X. X. Xi (Penn State University)
Prof. Dr. R. Kleiner (University of Tübingen)
Prof. Dr. Ir. B. Poelsema (University of Twente)
Prof. Dr. J. Aarts (Leiden University)

***Cover**: Plasma formed by pulsed-laser ablation of Mg target in Ar ambient gas and MgB_2 crystal structure*

The work described in this thesis has been financially supported by the Strategic orientation Materials Science of Interfaces, MESA$^+$ Institute for Nanotechnology It was carried out in the Low Temperature Division at the Faculty of Science and Technology and MESA$^+$ Institute for Nanotechnology at the University of Twente, P.O. Box 217, 7500 AE Enschede, The Netherlands.

D. Mijatovic
MgB_2 thin films and Josephson devices
Ph.D. thesis University of Twente, Enschede, The Netherlands.

ISBN 90-365-2038-x

Print: PrintPartners Ipskamp, Enschede

MgB_2 THIN FILMS AND JOSEPHSON DEVICES

PROEFSCHRIFT

ter verkrijging van
de graad van doctor aan de Universiteit Twente,
op gezag van de rector magnificus,
prof. dr. F.A. van Vught,
volgens besluit van het College voor Promoties
in het openbaar te verdedigen
op donderdag 3 juni 2004 om 15.00 uur

door

Dragana Mijatović (Rakić)
geboren op 8 oktober 1973
te Novi Sad (Servië)

Dit proefschrift is goedgekeurd door:

Prof. Dr. H. Rogalla (promotor)
Prof. Dr. Ing. D.H.A. Blank (promotor) en
Dr. Ing. A.J.H.M. Rijnders (assistent-promotor)
Dr. Ir. J.W.M. Hilgenkamp (assistent-promotor)

Table of Contents

1 Introduction

The discovery of superconductivity with a critical temperature (T_C) of 39 K in magnesium diboride (MgB_2), announced in January 2001 [1,2], has triggered an intensive worldwide research on this compound that was first synthesized in the 1950's [3]. In 1970 superconductivity was discovered by *Cooper et al.* [4] in NbB_2 with critical temperature of 3.87 K and in $Zr_{0.13}Mo_{0.87}B_2$ with T_C around 11 K. In systematic studies of diborides MeB_2 (*Me* = Ti, Zr, Hf, V, Nb, Ta, Cr and Mo) in the late seventies *Leyarovska et al.* [5] found that only NbB_2 was showing superconductivity [6]; in their studies MgB_2 was not investigated. Therefore, this unexpected property of this material has been waiting for several decades to be discovered. The history of superconductivity would probably have turned a different direction if the superconductivity of MgB_2 had been discovered already in the 1970's or even earlier before Nb_3Sn and Nb-Ti alloys were developed as practical superconductors [7].

The remarkable properties of MgB_2 open a new window in superconductivity for fundamental as well as applied research. MgB_2 is a very simple binary compound, but with surprising properties. It was found to be an electron-phonon superconductor with a much higher critical temperature and a significantly smaller isotope shift than Bardeen-Cooper-Schrieffer (BCS) theory would predict [7]. Furthermore, whereas the concept of two superconducting gaps present in a superconductor has been considered before [8,9], MgB_2 is the first example where this effect is strongly expressed.

The critical temperature of MgB_2 at 39 K enables the realization of electronic circuits based on this material to operate at 20-25 K, achievable by a compact

cryocooler [10], which gives a significant advantage to this material compared to the low-temperature superconductors. Compared to the high-temperature superconductors, MgB_2 is simpler, cheaper, and more stable over time. The nature of the superconductivity in MgB_2 and the advantageous properties of this material are briefly discussed in Chapter 2.

To realize superconducting Josephson devices based on this material that can be implemented further in electronic circuits, crystalline grown MgB_2 thin films are preferred. Ideally, the epitaxial MgB_2 thin films are needed for Josephson junction fabrication to ensure the tunneling in the *a*-*b* plane where the higher superconducting gap is present.

Chapter 3 briefly reviews the main features of the deposition techniques used in thin film fabrication and analysis tools needed for thin film structure and morphology investigation.

The high vapor pressure of magnesium and the high affinity of magnesium and boron to oxidation are necessary to overcome during the fabrication of MgB_2 thin films. To find the optimum conditions and parameters for MgB_2 deposition in vacuum techniques, several aspects of MgB_2 thin film growth are analyzed and they will be discussed in Chapter 4.

Chapter 5 describes two methods used for the preparation of MgB_2 thin films. The films were made by Pulsed Laser Deposition (PLD) and Hybrid Physical-Chemical Vapor Deposition (HPCVD). This Chapter discusses the properties of the fabricated films as well.

The fabrication of weak links made in MgB_2 films is described and analyzed in Chapter 6. The films prepared by PLD were used for the first realization of all-MgB_2 ramp-type Josephson junctions. In films made by HPCVD and PLD, nanobridges were structured as another approach for the formation of weak links. This Chapter gives an insight into the properties of the weak links as well as outlooks for improvement of the Josephson junctions.

MgB_2 ring-structures incorporating nanobridges display Josephson quantum interference effects, which forms the basis for the creation of all-MgB_2 Superconducting Quantum Interference Devices (SQUIDs). The experimental realization of nanobridge-based MgB_2 SQUIDs made from both, PLD and HPCVD films, and their properties are presented in Chapter 7.

References:

[1] J. Akimitsu, Symposium on Transition Metal Oxides, Sendai, January 10 (2001).
[2] J. Nagamatsu, N. Nakagawa, T. Muramaka, Y. Zenitani and J. Akimitsu, Nature **410**, 63 (2001).
[3] M. Jones and R. Marsh, J. Appl. Chem. Soc. **76**, 1434 (1953).
[4] A. S. Cooper, E. Corenzerst, L. D. Longinotti, B. T. Matthias and W. H. Zachaariasen, Proc. Natl. Acad. Sci **67**, 313 (1970).
[5] L. Leyarovska and E. Leyarovski, J. Less-Common Metals **67**, 249 (1979).
[6] D. Kaczorowski, J. Klamut and A. J. Zaleski, cond-mat/0104479 (2001).
[7] P. C. Canfield and G. W. Crabtree, Physics Today **56**, 34 (2003).
[8] H. Suhl, B. T. Matthias and L.R. Walker, Phys. Rev. Lett. **3**, 552 (1959).
[9] G. Binnig *et al*., Phys. Rev. Lett. **45**, 1352 (1980).
[10] R. Dagani, Chemical and Engineering News **80**, 11 (2002).

Magnesium - diboride (MgB_2)

2

Abstract

The intermetallic compound magnesium-diboride (MgB_2) exhibits superconductivity with a transition temperature of T_C = 39 K, which is the highest up to now discovered among intermetallic compounds. Although a very simple binary compound, MgB_2 is an unusual electron-phonon BCS superconductor with the simultaneous existence of two energy gaps. The advantageous properties compared to other superconductors, like an unexpectedly high critical temperature, relatively long coherence length and the high critical current density make this material favorable for, among others, thin film electronic device applications.

2.1 Introduction

MgB_2 has the highest critical temperature among the borides in which superconductivity has been investigated up to now, owing it to its specific electronic structure and strong coupling of electrons within the boron layers to an in-plane vibrational mode. This Chapter gives a description of the MgB_2 structure and the origin of its superconductivity. It gives also a glance on the advantageous properties of this material, which make it very interesting for investigation of its fundamental properties as well as promising material for applied superconductivity.

2.2 Crystal and electronic structure of MgB_2

The crystal structure of MgB_2 is given by a hexagonal (AlB_2 type, space group *P6/mmm* [1,2]) structure. It consists of alternating hexagonal layers of Mg atoms and graphite-like honeycomb layers of B atoms (Fig. 2.1). The unit cell lattice parameters for MgB_2 are ***a*** = 3.08489 (3) Å and ***c*** = 3.52107 (5) Å [3]. The intraplanar B-B bonds are much shorter than the distance between the planes, and hence the B-B bonding is strongly anisotropic [4,5].

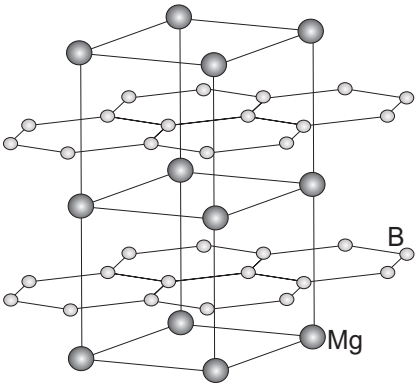

Fig. 2.1 *MgB_2 crystal structure*

MgB_2 is a strongly anisotropic phonon-mediated BCS *s-wave* superconductor. It has three σ and two π bands (Fig. 2.2) [6]. The σ bands are formed by covalent bonding of the two B sp^2 hybrids, which are directed along a B-B bond. The π-bands are formed by the overlap of B p_z and Mg *s* orbitals. Mg donates its electrons to each of the π bands, i.e. p_z orbitals, of two neighboring B atoms and therefore Mg is fully ionized. The attractive potential from the Mg^{2+}

ions is felt much stronger by a p_z electron than by electrons from the σ bands. This lowers the energy of the π bands resulting in electrons being transferred from σ bands to π bands. This drives the hole doping of the σ bands [6,7]. The holes at the top of these σ bands manifest two-dimensional properties and are localized in boron sheets. On the other hand, mostly three-dimensional electrons and holes in the π-bands are delocalized over the whole crystal. Thus, one can say that MgB_2 is held together by strongly covalent bonds within the boron layers and by 'metallic-type' bonds between these sheets. These 2D covalent and 3D metallic type states contribute almost equally to the total density of states (DOS) at the Fermi level [4].

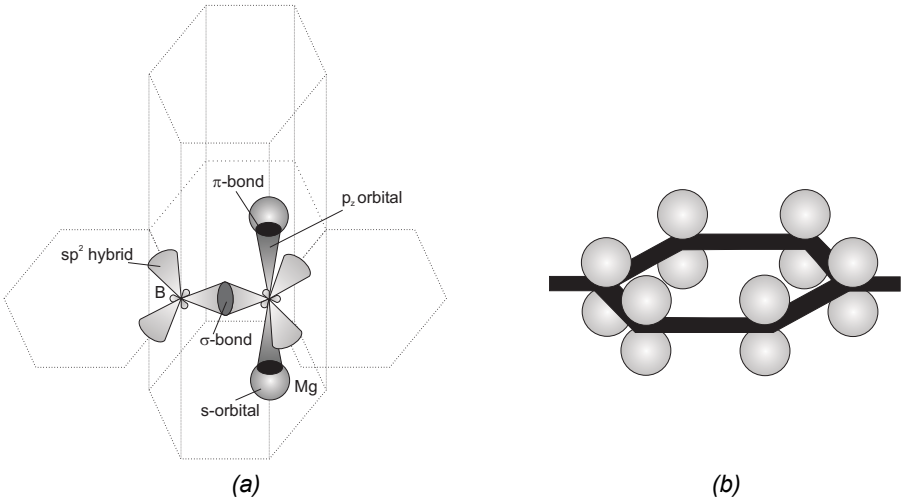

Fig. 2.2 *Schematic representation of the electronic structure of MgB_2. (a) The σ bonds are formed by overlapping sp^2 boron orbitals and the π bonds are made by overlapping p_z boron and s magnesium orbitals. (b) The black hexagonal network represents the σ bands i.e. a two-dimensional network of the σ bonds. Gray lobes correspond to the π bands i.e. a three-dimensional network of the π bonds (from [8]).*

2.3 Superconductivity in MgB_2

Being an electron-phonon superconductor, MgB_2 has a higher T_C than expected. Starting from the BCS formula:

$$k_B T_C = 1.13\hbar\omega_D \exp\left[-1/VN(E_F)\right], \tag{2.1}$$

T_C depends only on three material parameters: the characteristic phonon energy $\hbar\omega_D$, the electronic density of states $N(E_F)$, and the electron-phonon interaction giving rise to electron-electron attractive interaction V. The $VN(E_F)$-product is

denoted as an electron-phonon coupling constant λ. The phonon energies, although very high[1], are not especially different from other borides and light-element binary compounds that have much lower T_C. The density of states is low, since MgB_2 has no *d* electrons. Therefore, only one parameter in the BCS formula can influence such a high T_C: the electron-phonon coupling as expressed through *V* [8].

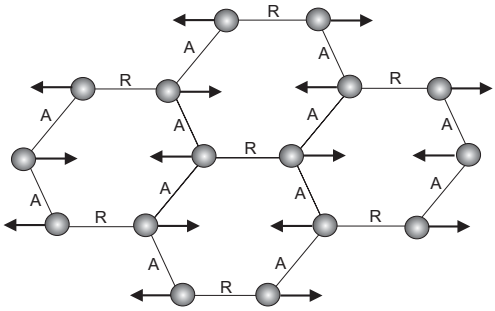

Fig 2.3 *Schematic view of the E_{2g} (vibrational in-plane) phonon mode of boron atoms strongly coupled to electrons from the σ bands at the Fermi level. As boron atoms move in the arrow directions, shortened bonds ('A') become attractive to electrons, whereas elongated bonds ('R') become repulsive (from [9]).*

In conventional superconductors, the electron-phonon interaction creates Cooper pairs of approximately equal pair strength, distributed evenly over the Fermi surface. In MgB_2, there is one high-energy (about 515 cm^{-1}) optical phonon mode (E_{2g}), which couples very strongly to electrons in the 2D σ band [8]. The strong coupling originates in the special covalent nature of the σ band. The σ band has the charge concentrated along the B-B axis. Thus, when the B atoms move in the plane, the charge must redistribute significantly to accommodate the change and the charge in the plane becomes substantially distorted (Fig. 2.3) [8]. This distortion couples strongly to the electrons.

2.3.1 Two superconducting bands and isotope effect

The strong electron-phonon coupling in the 2D σ bands and weak coupling in the 3D π bands lead to the simultaneous existence of two energy gaps in this

[1] In a simple model of a solid, the atoms can be presented as masses *m* connected by springs with spring constant *k*. The characteristic frequency of such a model is $\omega = (k/m)^{1/2}$, which has for light atoms a very high value.

material [8,10]. From the value of the electron-phonon coupling constant $\lambda_\sigma = 1$ [5,7,11,12] it implies that the electron-phonon coupling reaches the strong coupling regime of the σ electrons. On the other hand, the electron-phonon coupling of the π electrons remains in the weak coupling regime $\lambda_\pi = 0.44$ [13]. As a result, the properties of superconductivity are proposed to be different in both bands. The σ band shows a large gap, $\Delta_\sigma = 7.09$ meV, whereas the π band shows a small gap $\Delta_\pi = 2.70$ meV (Table 2.1), both closing at a joint critical temperature, T_C. This holds for the clean limit, where the coherence length is much smaller than the electron mean-free path. The double-gap nature has been verified by tunneling experiments (e.g. [14-17]), specific heat measurements [18] and spectroscopy [19-21] (Table 2.1).

The two sets of electrons (from σ and π bands) interact, although weakly, through scattering from states in one band to the states in the other one and through Coloumb repulsion. This small interaction causes, for example, both bands to become superconducting at the same temperature. In contrast, a large interaction would mix the two bands thoroughly and wash out the different size and the distinction of the two superonducting gaps present in this material.

If the existence of different bands in MgB_2 is neglected then, following [11], one can calculate electron-phonon coupling constant λ averaged over the whole Fermi surface. Further, T_C can be calculated using the equation (2.1) and T_C of about 25 K would be obtained, which is much lower than the maximum observed value of 39 K. Taken into account two-band nature of the superconductivity in MgB_2, keeping the average λ the same, T_C is not determined by the average λ anymore, but by the maximum eigenvalue of λ matrix (λ_{max}). λ_{max} is always larger than average λ, which results in the larger T_C (more detailed discussion is in [10]).

In the dirty limit (where coherence length is larger than the electron mean-free path), only one gap of intermediate magnitude is expected to be observed, closing at a reduced T_C (see e.g. [13,21,22]). Especially the electron mean-free path depends on the material properties determined by the preparation technique, as we will describe in Chapter 5.

2.4 Basic properties

Table 2.1 gives an overview of some MgB_2 parameters that determine basic properties of this unusual superconductor. The data originate from the experiments and theory published up to now. The experimental data show some spread, partly because they are collected from different types of MgB_2 samples (bulk, wires, films etc.) and different methods of investigation of their properties.

Table 2.1 *List of some superconducting parameters of MgB_2.*

Parameter	Experimental values	Theoretical values
Coherence length	ξ_{ab} (0) = 3.7 – 12 nm * ξ_c (0) = 1.6 - 3.6 nm *	
Penetration depths	λ (0) = 85 - 180 nm *	λ_{ab}^{clean} (0) = 39.2 nm ** λ_c^{clean} (0) = 39.7 nm ** λ_{ab}^{dirty} (0) = 105.7 nm ** λ_c^{dirty} (0) = 316.5 nm **
Energy gaps	Δ_σ (0) = 5.5 - 8.2 meV *** Δ_π (0) = 1.5 - 3.5 meV ***	Δ_σ (0) = 7.09 meV Δ_π (0) = 2.70 meV
Upper critical field	$H_{C2}\|ab(0)$ = 14 - 39 T * $H_{C2}\|c(0)$ = 2 - 24 T *	
Lower critical field	$H_{C1}(0)$ = 27 - 48 T *	
Irreversibility field	$H_{irr}(0)$ = 6 - 35 T *	

* [22]

** [24]

*** [3,9,15,19-21,30-33]

BCS type II superconductors are characterized by a lower critical magnetic field (H_{C1}) and an upper critical magnetic field (H_{C2}). The value of H_{C1} for MgB_2 ranges from 27-48 mT (Table 2.1) [23]. The values for the penetration depth $\lambda(0)$ deduced from the lower critical field data range between 85 and 180 nm [23]. The theoretical values of the penetration depths for the clean case are smaller than the smallest experimental value. On the other hand the values for the dirty case are in a good agreement with experiment. Nearly all measured penetration depths fall within the theoretical limiting cases (clean and dirty) [24]. The upper critical field in the direction parallel to *a*-*b* plane ($H_{C2}\|ab(0)$) can vary from 14-39 T, whereas in the direction parallel to *c*-plane ($H_{C2}\|c(0)$) can be 2-24 T (Table 2.1) [23], depending if the measurements were performed on single crystals, bulk, films or wires.

Coherence length $\gamma_\xi = \xi_{ab}/\xi_c$ [24-27] and penetration depth anisotropy $\gamma_\lambda = \lambda_c/\lambda_{ab}$ is observed [28,29]. Anisotropy is very important for a basic understanding of this material as well as for practical applications, strongly affecting the flux pinning and the critical currents. At low temperatures γ_ξ is about 6 (for polycrystalline samples as well as for single crystal), which is close to the theoretically expected value from the geometry of the Fermi surface associated

with the σ band. This suggests that the low-temperature, high-field superconducting state is dominated by just the σ band [6,8].

In the case of the intermetallic superconductors a high T_C is associated with large room-temperature resistivity originating from the strong electron-phonon scattering of electrons in the normal state. MgB_2, however, has a low room-temperature resistivity (about 10 $\mu\Omega$cm) and a very low resistivity just above T_C (around 0.5 $\mu\Omega$cm) in comparison to Nb_3Sn that has room-temperature resistivity of 80 $\mu\Omega$cm and 10 $\mu\Omega$cm just above its T_C [8]. The low resistivity of MgB_2 is a consequence of having two bands with very different electron-phonon coupling strengths. The 3D π band, which has the smaller electron-phonon coupling, dominates the high-temperature resistivity, whereas the superconductivity is primarily due to the larger coupling in the 2D σ band. This simplified picture implies a moderate anisotropy in the normal-state resistivity, with a larger resistivity in the *c*-direction than in the basal plane [8].

2.4.1 Doping and reactivity of MgB_2

From the BCS formula given above (eq. (2.1)), it can be noticed that a change in $N(E_F)$ or ω_D results in a change of T_C. It is possible to tune $N(E_F)$ and ω_D by varying the chemical composition. In the high-T_C superconductors (HTS) studies the effect of chemical substitution have been highly productive in enhancing the physical properties, such as critical temperature, as well as in investigating the mechanism for superconductivity. This motivated the researchers to investigate the effect of chemical substitution in MgB_2 bulk compounds.

From many experiments done with substitution, only Al and Mn substitution for Mg and C substitution for B have been substantiated. All of these successful substitutions (Al, C and Mn) decreased T_C. The solubility limit (x in $Mg_{1-x}M_xB_2$) for Li as 0.3 [33] or 0.015 [34], for Na as 0.2 [34], for Zn as 0.1 [35], for Ir as 0.06 [36], for Mn as 0.03 [35] and for Cu as 0 [37] did not increase T_C as well [38]. MgB_2 is found to be very resistant to solubility.

The severe limitation in substitutional chemistry of MgB_2 is, in one sense, advantageous, as MgB_2 would be expected to display limited chemical reactivity with materials that it would come in contact with in electronics application. ***He et al***. [39] summarizes their results in Table 2.2 (from [39]) to determine the chemical compatibility of MgB_2 with various electronic materials at temperatures between 600 and 800°C, temperature relevant for the fabrication of electronic devices. It shows that MgB_2 is chemically compatible (i.e., does not react) with many electronic materials in that temperature range.

Table 2.2 *Reactivity of MgB_2 with various electronic materials (from [39]).*

Electronic material	600°C anneal	800°C anneal
ZrO_2	No reaction	No reaction
YSZ	No reaction	Small amounts of MgO
MgO	No reaction	No reaction
Al_2O_3	No reaction	MgB_2 with altered cell size (Al doped), MgO
SiO_2	MgB_2, MgO, Si	MgO, Mg_2Si, Si, MgB_2, MgB_4
$SrTiO_3$	No reaction	MgB_2, $SrTiO_3$, MgO, SrB_6, TiB_2
Si	MgB_2, Mg_2Si	MgB_2, Mg_2Si, MgB_4
TiN	No reaction	No reaction
TaN	No reaction	No reaction
AlN	No reaction	No reaction
SiC	No reaction	MgB_2 with altered cell size (carbon doped)

They found that MgB_2 is inert for many common electronic and substrate materials at 600°C (only MgB_2 and the starting material was observed in the XRD patterns). At these temperatures, a clear reaction was found for SiO_2 and Si. At 800°C, MgB_2 was found to be inert with respect to ZrO_2, YSZ, MgO, TiN and AlN up to 700-800°C. However, MgB_2 was highly reactive toward some of the most common substrate materials, i.e., Al_2O_3 and $SrTiO_3$, showing their limitations if high fabrication temperatures must be used during film deposition.

2.5 Possible applications of MgB_2

MgB_2 material is a good candidate for many applications due to its attractive properties. Its critical temperature of 39 K enables electronic circuits and devices based on this material to operate at 20-25 K or even 30 K, which gives a significant advantage to this material compared to low-temperature superconductors, such as Nb. Current niobium-based superconductor circuits must operate at temperatures close to 4.2 K, which requires cryocoolers with several kilowatts of input power, which is not acceptable for most electronic applications. Circuits based on high-temperature superconductors (HTS) would solve this problem, but up to now, the fabrication of reproducible HTS Josephson junctions with sufficiently small variations in device parameters has been proven to be problematic. An MgB_2-based circuit will operate at about 25 K, achievable by a compact cryocooler with roughly one-tenth of the mass and the power consumption of a 4.2 K cooler of the same cooling capacity [40].

Nb-based superconductor integrated circuits using rapid single-flux quantum logic (RSFQ) have demonstrated the potential to operate at clock frequencies above 700 GHz [41,42]. The ultimate limit on device and circuit speed is proportional to $I_C R_N$ i.e. the product of the junction critical current, I_C, and the junction normal-state resistance, R_N. Because $I_C R_N$ is proportional to the energy gap of the superconductor [43], the larger energy gap in MgB_2 could lead to even higher speeds than in Nb-based superconductor integrated circuits [44]. As noted above, MgB_2 has two gaps and even the smaller one, $2\Delta \sim 5$ meV, is larger than that of Nb, $2\Delta \sim 3$ meV [43]. As pointed out by *Brinkman et al*. [22], large $I_C R_N$ products are feasible, because both band contribute to $I_C R_N$. In the *a-b* plane an $I_C R_N$ product of 5.9 mV at $T = 4.2$ K is predicted and 4.0 mV in the *c*-axis direction.

MgB_2 is simpler, cheaper and more stable over time compared to high-temperature superconductors, making it attractive for a number of applications. For example, in the case of Superconducting Quantum Interference Devices (SQUIDs) based on MgB_2 less noise is expected, giving a certain advantage for electronic circuits made in MgB_2 technology. It was noticed that in the case of dc-SQUIDs, the low-frequency noise, is 2-3 orders of magnitude lower than that of $YBa_2Cu_3O_{7-x}$ SQUIDs early in their development [45]. This result suggests that low-frequency noise due to thermal activation of trapped flux vortices is less of an issue in MgB_2 SQUIDs than in HTS-based SQUIDs. *Burnell et al.* [46] have measured the noise of a SQUID operating at 20 K and found that it is consistent with that reported for SQUIDs made by point contact junctions [44] and comparable to HTS SQUIDs improved by years of experiments. We measured a white noise level of 76 $\mu\phi_0/\sqrt{Hz}$ in the frequency range from 1 Hz until 1 kHz at 34.5 K for magnetometer based on MgB_2 nanobridges made on epitaxial films [47]. This corresponds to an effective flux noise of 1 $pT/\sqrt{Hz}$, which makes magnetometer sensitive enough for measuring the adult magnetocardiogram (MCG) (see Chapter 7, Section 7.4.2). These results are very encouraging for the development of superconducting electronics and devices operating at 20-30 K based on MgB_2. It was found that MgB_2 is capable of transporting high critical currents (currently in order of mid-10^7 A/cm^2 in epitaxial thin films [46] to 10^8 A/cm^2 [48] at 4.2 K and ~ 10^6 A/cm^2 in commercial MgB_2 powder [49] at 10 K), because, unlike the ceramic (HTS) superconductors, the grain boundaries between crystals do not obstruct current flow. Further increase in the critical current density value will make this material even more desirable for electrotechnical device application.

Modern large current carrying conductors are made from Nb-Ti ($T_C = 9$ K, H_{C2} (4.2 K) = 10 T), Nb_3Sn ($T_C = 18$ K, H_{C2} (4.2 K) = 28 T) and the high-temperature superconductors $Bi_2Sr_2CaCu_2O_{8-x}$ ($T_C \sim 90$ K) and $(Bi, Pb)_2Sr_2Ca_2Cu_3O_{10-x}$ ($T_C \sim 110$ K). At low temperatures the HTS polycrystals have

H_{C2} above 50 T, but their main disadvantages are the high anisotropy ($H_{C2}^{\parallel} / H_{C2}^{\perp} > 20$) and weakly linked grain boundaries that obstruct the current [50,51]. Complicated and expensive texture processes are designed to enlarged critical current density (J_C). Additionally, MgB_2 offers the advantages of round-wire geometry, low raw-material cost, high strength and high J_C. Moderate H_{C2} anisotropy compared to HTS materials would possibly allow efficient pinning of vortices [51,52].

The continuous improvement in quality of MgB_2 thin films and the first promising results in SQUID fabrication [53,47] make their implementation in the electronic circuits possible. Taking into account that the mass density of this material and its electrical resistivity of the normal state is low, magnets and cables made of MgB_2 may be significantly lighter and cheaper than those of Nb_3Sn and Nb-Ti [8]. Such potentials look very promising especially combined with a T_C of almost 40 K.

2.6 Summary

The advantageous properties of MgB_2 (addressed above) are favorable for, e.g., thin film electronic device application. Important aspects in the thin film growth, like stability and reactivity of this material (as briefly mentioned here) will be addressed in Chapter 4. The reactivity of MgB_2 limits the choice of the substrates for thin film deposition and will be discussed in the same Chapter.

The fabrication of thin films will be presented in Chapter 5 together with their properties. The electron mean-free path, as one of the material properties, will be determined in that Chapter and used to appoint whether the film is in the clean or dirty limit (which are defined in Section 2.3.1), i.e., it is dependent on the amount of impurities present in the film.

The unusual superconducting nature of MgB_2, i.e., the existence of two superconducting gaps, as described in this Chapter, is of importance for fabrication of the Josephson junctions and, subsequently, for electronic devices. First results on the weak link formation and their implementation in SQUIDs will be presented in this thesis.

References:

[1] J. Hlinka *et al*., Phys. Rev. B **64**, 140503R (2001).
[2] J. Akimitsu and T. Muranaka, Physica C **388**, 98 (2003).
[3] J. D. Jorgensen, D. G. Hinks and S. Short, Phys. Rev. B **63**, 224522 (2001).
[4] I. I. Mazin and V. P. Antropov, Physica C **385**, 49 (2003).
[5] J. Kortus, I. I. Mazin, K. D. Belashchenko, V. P. Antropov and L. L. Boyer, Phys. Rev. Lett. **86**, 4656 (2001).
[6] I. I. Mazin *et al*., Phys. Rev. B **89**, 107002 (2002).
[7] J. M. An and W. E. Pickett, Phys. Rev. Lett. **86**, 4366 (2001).
[8] P. C. Canfield and G. W. Crabtree, Phys. Today **56**, 34 (2003).
[9] H. J. Choi, D. Roundy. H. Sun, M. L. Cohen, S. G. Loule, Nature **418**, 758 (2002).
[10] A. Y. Liu, I. I. Mazin and J. Kortus, Phys. Rev. Lett. **87**, 087005 (2001).
[11] Y. Kong, O. V. Dolgov, O. Jepsen, and O. K. Andersen, Phys. Rev. B **64**, 020501 (R) (2001).
[12] T. Yildirin *et al*., Phys. Rev. Lett. **87**, 37001 (2001).
[13] A. A. Golubov *et al*., J. Phys.: Condens. Matter. **14**, 1353 (2002).
[14] R. S. Gonnelli *et al*., Phys. Rev. Lett. **89**, 247004 (2002).
[15] F. Giubileo *et al*., Phys. Rev. Lett. **87**, 177008 (2001).
[16] M. Iavarone et al., Phys. Rev. Lett. **89**, 187002 (2002).
[17] H. Schmidt, J. F. Zasadzinski, K. E. Gray and D. G. Hinks, Phys. Rev. Lett. **88**, 127002 (2002).
[18] F. Bouquet *et al*., Phys. Rev. Lett. **87**, 047001 (2001); Europhys. Lett. **56**, 856 (2001).
[19] X. K. Chen *et al*., Phys. Rev. Lett. **87**, 157002 (2001).
[20] P. Szabo *et al*., Phys. Rev. Lett. **87**, 137005 (2001).
[21] H. Schmidt, J. F. Zasadzinski, K. E. Gray and D. G. Hinks, Physica C **385**, 221 (2003).
[22] A. Brinkman *et al.*, Phys. Rev. B **65**, 180517 (R) (2002).
[23] C. Buzea and T. Yamashita, Superond. Sci. Technol. **14**, R115 (2001).
[24] A. A. Golubov *et al*., Phys. Rev. B **66**, 054524 (2002).
[25] P. Miranovic *et al*., J. Phys. Soc. Jpn. **72**, 221 (2003).
[26] A. Gurevich, Phys. Rev. B **67**, 184515 (2003).
[27] T. Dahm and N. Schopohl, Phys. Rev. Lett. **91**, 017001 (2003); T. Dahm, S. Graser and N. Schopohl, cond-mat/0304194.
[28] V. G. Kogan, Phys. Rev B **66**, 020509 (R) (2002); Phys. Rev. Lett. **89**, 237005 (2002).
[29] A. A. Golubov and A. Koshelev, Phys. Rev. B **68**, 104503 (2003).

[30] M. H. Badr *et al.*, Physica C **388-389**, 139 (2003).
[31] S. Lee *et al*., Physica C **377**, 202 (2002).
[32] P. Szabo *et al*., Physica C. **388**, 145 (2003).
[33] J. S. Slusky *et al.*, Physica C **361**, 91 (2001).
[34] S. Y. Li *et al*., Physica C **363**, 219 (2001).
[35] S. M. Kozakov *et al.*, Solid State Commun. **119**, 1 (2001).
[36] M. M. A. Sekkina and K. M. Elsabawy, Physica C **391**, 217 (2003).
[37] S. Xu, Y. Moritomo, K. Kato, A. Makamura, J. Phys. Soc. Jpn. **70**, 1889 (2001).
[38] D. G. Hinks, J. D. Jorgensen, H. Zheng and S. Short, Physica C **382**, 166 (2002).
[39] T. He, R. J. Cava and J. M. Rowell, Appl. Phys. Lett. **80,** 291 (2002).
[40] R. Dagani, Chemical and Engineering News **80**, 11(2002).
[41] T. van Duzer and C. W. Turner, *Principles of Superconductive Devices and Circuits*, 2nd ed., Prentice-Hall PTR (1999).
[42] D. K Brock, E. K. Track and J. M. Rowell, IEEE Spectrum **37**, 40 (2000).
[43] A. W. Kleinsasser, IEEE Trans. Appl. Supercond. **11**, 1043 (2001).
[44] X. H. Zeng *et al*., Nature Materials **1**, 1 (2002).
[45] Y. Zhang *et al*., Appl. Phys. Lett. **79**, 3995 (2001).
[46] G. Burnell *et al*., Superond. Sci. Technol. **16**, 254 (2003).
[47] D. Mijatovic *et al*., unpublished
[48] S. Y. Xu *et al*., Phys. Rev. B **68**, 224501 (2003).
[49] A. D. Caplin *et al*., Supercond. Sci. Technol. **16**, 176 (2003).
[50] D. Dimos, P. Chaudhari, J. Mannhart and F. K. LeGoues, Phys. Rev. Lett. **61**, 219 (1988).
[51] A. Gurevich *et al*., Supercond. Sci. and Technol. **17**, 278 (2004).
[52] M. H. Jung *et al*., Chem. Phys. Lett. **343**, 447 (2001).
[53] A. Brinkman *et al*., Appl. Phys. Lett. **79**, 2420 (2001).

Deposition techniques and analysis tools

3

Abstract

Pulsed-Laser Deposition (PLD), RF magnetron sputter deposition and Chemical Vapor Deposition (CVD) techniques are very powerful tools in thin film fabrication and can be employed in in-situ MgB_2 thin film growth.

The surface morphology, composition, and crystal structure of the deposited films are important thin film properties. These properties are characterized by Atomic Force Microscopy (AFM), Scanning Electron Microscopy (SEM), X-ray Diffraction (XRD), and X-ray Photoelectron Spectroscopy (XPS). AFM and SEM are used for monitoring the surface of the thin film, XRD for determining the film structure, and XPS for the film composition.

3.1 Introduction

This Chapter addresses the basic properties of PLD, RF magnetron sputter deposition and CVD techniques that have been used in MgB_2 thin film growth as well as a number of analysis tools used for thin film characterization. AFM and SEM were employed in investigation of the thin film morphology, whereas XRD was utilized in determining the film structure and crystallinity and XPS in investigating the thin film composition.

3.2 Experimental techniques

3.2.1 Pulsed-laser deposition (PLD)

Basic principles

In PLD, a pulsed laser beam is focused on a target, resulting in an ablation of the target material [1,2]. At the beginning of the laser pulse, a dense layer of vapor is formed in front of the target. Absorbed energy during the laser pulse causes an increase of the temperature and pressure of the vapor, resulting in partial ionization. Due to the high pressure gradient in the vapor near the target surface the evaporated material expands, forming a plasma. Placing the substrate on the opposite side of the plasma, the material can be deposited on it in the form of a film [2].

A number of unique features of the PLD technique makes it advantageous over conventional thin-film deposition techniques like sputtering, Molecular-Beam Epitaxy (MBE) and CVD. One of them is the relatively easy removal of species from stoichiometric targets that enables the fabrication of complex multicomponent films. A large number of variable parameters in this technique, such as laser characteristics (e.g., wavelength, pulse duration, beam profile), target properties (e.g., density, melting temperature, absorption coefficient, thermal conductivity), target-laser interaction (e.g., ablation rate, target surface morphology, volatility of materials), substrate properties (e.g., material, crystallinity, temperature), target-substrate geometry, and deposition ambient (gas, its purity and pressure), make PLD a very complex technique with a great possibility of tailoring the film properties. For example, during plasma expansion, internal thermal and ionization energies are converted into kinetic energies of the ablated particles. The mass and pressure of the ambient gas determine the interaction with the ablated particles, i.e., attenuation of the kinetic energy occurs during expansion caused by multiple collisions. This results in a wide range of kinetic energies of the ablated species - from high energy (typically up to 100 eV)

in vacuum to low energies (typically 0.1 eV) in sufficiently large ambient pressure. This feature of PLD can be used to modify the film growth since a change in the kinetic energies of the ablated species influences the kinetic energy of the particles arriving at the substrate.

The PLD technique allows a stoichiometric transfer of the target material to the substrate. However, in the case of deposition of a very volatile element the target with additional amount of the volatile element is needed to compensate for the loss due to the volatility of the material. The very high Mg vapor pressure determines a high volatility of Mg. To compensate for Mg loss, a target with additional amount of Mg is needed. As we will see in Chapter 4, color of the plasma originating from a Mg and/or Mg-enriched MgB_2 targets is used as an indicator for the presence of the ionic Mg necessary to achieve superconducting films.

Another unique characteristic of PLD is a relatively high deposition rate per pulse compared to other thin-film deposition techniques [2]. During relatively long intervals between two pulses, which are determined by the laser pulse repetition rate, the instantaneous deposition of the ablated material is followed by the growth of the film through rearrangement, migration and nucleation of adatoms. A high deposition rate achieved by PLD is beneficial in reduction of impurities (such as oxygen) in the films.

PLD set-up

A schematic view of the PLD system is presented in Fig. 3.1. The experiments were performed with the KrF excimer lasers (Lambda Physik Compex 205 and LPX 210 iF, wavelength λ = 248 nm) with a pulse duration of about 25 ns (FWHM) and a maximum pulse repetition rate of 50 Hz for Lambda Physik Compex 205 (maximum energy 650 mJ) and 100 Hz for LPX 210 iF lasers (maximum energy 700 mJ). The laser beam, focused by the optical lens (focal length is 453 mm), enters the chamber under the angle of 45° with respect to the target normal. The mirror, lens, and vacuum chamber window accounted for about 20% energy loss of the laser beam.

A multi-target holder and a substrate holder including heater were inserted in the vacuum chamber using a load-lock system without breaking the vacuum. The system base pressure was ranging from 10^{-7} to 10^{-9} mbar depending on the deposition system used. The PID controlled temperature of the heater (resistively heated using thermo-coax wires) was measured using a K-type thermocouple. Argon (purity 99.995%) and two gas mixtures of argon and 4% hydrogen (purity 99.995% and 99.9999%) were used as ambient gases. The deposition pressure (0.1-0.22 mbar) is controlled by the effective pump speed and the total gas mass flow (Brooks Instruments, 0-40 ml/min at 10^5 Pa). The

effective pump speed is adjusted through a variable restriction between the deposition chamber and turbo-molecular drag pump.

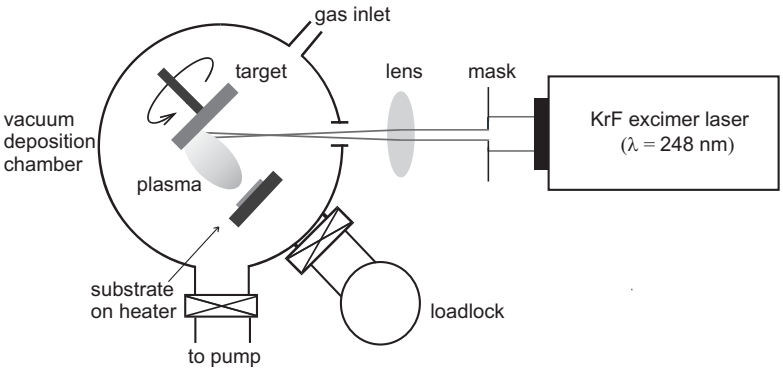

Fig. 3.1 *A schematic view of the PLD set-up.*

Combined technique: PLD and RF magnetron sputter deposition set-up

Although most of MgB_2 thin films were fabricated using PLD, first attempts were made with a combined technique: PLD of Mg and RF magnetron sputter deposition of B. This enables the control of the independent fluxes of Mg and B, both originating from very pure targets. The low heat conductivity of boron easily causes splashing during PLD of a B target. Therefore, sputter deposition seems to be a better way for boron deposition.

In Fig. 3.2 a schematic view of the combined deposition technique: PLD and RF magnetron sputter deposition is presented. Sputter deposition can be combined with PLD in thin film growth allowing tuning the ratio of independent fluxes coming from sputter and PLD target. This combined technique could be suitable for MgB_2 growth. RF magnetron sputter deposition of B target could be combined with PLD of Mg target. RF sputtering of B is needed due to the low conductivity of B, whereas magnetron sputtering allows implementation of more effective power into the system and the increase of the efficiency of the Ar ions. The substrate was placed under the angle of $\alpha = 45°$ or 60° with respect to the heater normal and opposite to the PLD target, which makes it possible that the arrival of both, sputter B and laser ablated Mg particles at the same time at the substrate. RF magnetron power was ranging from 50 to 150 W for 2” diameter target. The heater temperature and gases pressures are controlled in the same way as described in PLD set-up.

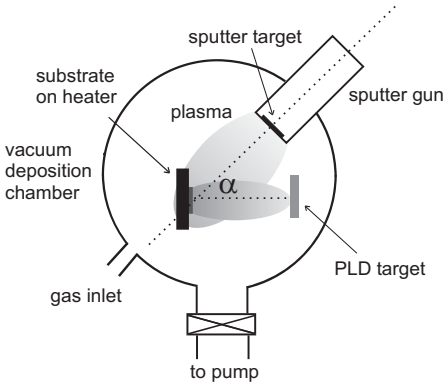

Fig. 3.2 *A schematic view of the combined technique: PLD and RF magnetron sputter deposition set-up.*

3.2.2 Chemical-Vapor Deposition (CVD)

Basic principles

In CVD a chemical reaction of a volatile compound of a material to be deposited occurs with other gases, to produce a non-volatile solid that deposits on a substrate [3]. Precursor gases are often diluted in carrier gases and delivered into the reaction chamber at ambient temperatures. As they pass over or come into contact with a heated substrate, they react or decompose forming a solid phase, which is deposited onto the substrate. The substrate temperature is critical and can influence what reactions will take place.

The advantage of this technique is the ability to produce a large variety of films and coatings of metals, semiconductors, and compounds in either crystalline or vitreous form, possessing high purity and desirable properties and it allows a controllable creation of films of widely varying stoichiometry. Hence, many variants of CVD processing have been developed. Hybrid processes combining features of both physical and chemical vapor deposition have also emerged, so called Hybrid Physical-Chemical Deposition (HPCVD), since CVD involves depositing a solid material from a gaseous phase and is similar in some respects to physical vapor deposition (PVD). PVD differs in that, because the precursors are solid, with the material to be deposited being vaporized from a solid target and deposited onto the substrate.

HPCVD set-up

A schematic representation of the HPCVD method has been depicted in Fig. 3.3. This method has been used in the fabrication of epitaxial MgB_2 thin films at Penn State University [4]. As a precursor gas 1000 ppm B_2H_6 in H_2 has been used together with evaporated solid Mg. The external inductor coil was used to vary the temperature of the substrate as well as the solid Mg. These temperatures are very important parameters in the process. Gas introduced in the chamber reacts with evaporated Mg. The reaction could be controlled by stopping the gas flow into the chamber. The pressure in the system during deposition is 100 Torr. More information about the set-up will be given in Chapter 5.

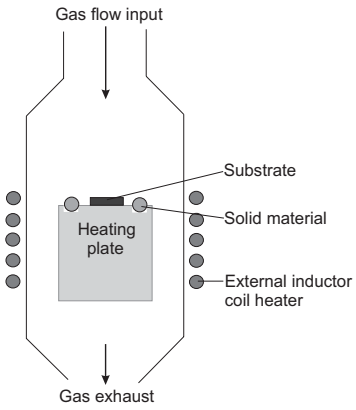

Fig. 3.3 *A schematic view of the HPCVD set-up (adapted from [4]).*

3.3 Analysis tools

Atomic-force microscopy (AFM) and Scanning-electron microscopy (SEM) were used for surface morphology investigation, X-ray diffraction (XRD) for crystalline structure analyses and X-ray photoelectron spectroscopy (XPS) for determination of the elemental composition of the samples. The experimental settings of these techniques are briefly addressed below.

Atomic Force Microscopy (AFM)

A Nanoscope III instrument (DI, Santa Barbara, CA) was used for atomic force microscopy experiments in ambient conditions, in contact or tapping mode

imaging. Standard Si_3N_4 triangular contact mode tips (k = 0.58 Nm^{-1}) and sharper rectangular tapping mode tips (k = 20-100 Nm^{-1}) were used.

Scanning Electron Microscopy (SEM)

A SEM type JSM-5610 (JEOL, Japan) was used with the accelerating voltage of the electron gun in the range of 2.4 to 15 kV.

X-ray Diffraction (XRD)

X-ray diffraction measurements *(θ-2θ and ϕ scans)* in the normal Bragg-reflection geometry were performed on a four-circle single-crystal diffractometer (CAD4, Enraf Nonius Delft, The Netherlands), using CuK_α radiation. The lattice parameters of the films were calculated from XRD data employing 10-12 reflections by least squares fitting technique. By determining the position in reciprocal space of some specific reflections, the orientation matrix of the substrate crystal can be determined. Since all the films were expected to be epitaxialy grown, the θ-2θ scans were performed in the *(00l)* direction of the substrate. Low-angle reflectivity measurements were performed as well in order to determine film thickness.

The instrumental broadening was estimated from the substrate peaks to be 0.2°. The θ-2θ scans showed additional peaks corresponding to spectral λ/2 and λ/3 lines originating from the strong *(00l)* reflection of the substrates.

X-ray Photoelectron Spectroscopy (XPS)

XPS measurements were carried out with a Physical Electronics Quantum2000 equipment and Quantera with a spherical sector analyzer and a multichannel plate detector (16 detector elements for Quantum2000 and 32 detector elements for Quantera). Analyzer Mode was constant pass energy. For the survey scan pass energy is 280 eV and for element scans 112 eV. Excitation Source was Al K_α monochromatic with source energy of 1486.7 eV. X-ray beam 100 μm diameter/25 W. Take-off angle is 45° (analyzer angle to sample surface). Temperature during analysis was 298 K. Pressure during analysis was 1-3x10^{-8} Torr. Argon ions were used for charge control and etching. For etching the sample ion gun with energy of 500 eV Ar-ions was employed (raster size 3 mm x 3 mm; incident angle: 45°).

For atomic concentration the Shirley background subtraction was used. The sensitivity factors were provided by Physical Electronics MultiPack software version 6.1A. The oxygen O1s (B_2O_3) signal at 533.3 eV [5] was used as a reference for surface charge correction.

References:

[1] D.B. Chrisey, G. K. Hubler, *Pulsed Laser Deposition of Thin Films*, John Wiley & Sons Inc., New York (1994).
[2] G. Rijnders, *The Initial Growth of Complex Oxides: Study and Manipulation*, Ph.D. Thesis, University of Twente, Enschede, The Netherlands (2001).
[3] M. Ohring, *The materials Science of Thin Films*, Academic Press (1992).
[4] J. Rowell, Nature Materials **1**, 6 (2002).
[5] V. I. Nefedov *et al*., Zh. Neorg. Khim. **20**, 2307 (1975).

Aspects of MgB_2 thin film growth

4

Abstract

Complicating factors in the fabrication of superconducting MgB_2 thin films are: a high vapor pressure of magnesium and a very low Mg sticking coefficient at elevated temperatures, requiring the compensation for its loss, and the high sensitivity of magnesium and boron to oxidation, requiring very low oxygen partial pressures in the deposition system as well as very high purity of the ambient gas used. To reduce Mg and B oxidation, a background pressure in vacuum-deposition systems lower than 10^{-9} mbar is needed. It is found that oxidation can be further reduced by adding H_2 to Ar as an ambient gas. In preparation of the films by PLD, the superconducting phase is achieved by tuning the deposition parameters to reach a blue Mg or Mg-enriched MgB_2 plasma.

To obtain epitaxial films, the choice of the substrate is of utmost importance focusing attention to the significant parameters such as lattice misfit and the reactivity with the film. The most suitable substrates are SiC, AlN and TaN due to their hexagonal surface, a low lattice misfit and a low or absence of the reactivity with the film at high deposition temperature.

4.1 Introduction

Smooth, single-phase, crystalline grown superconducting MgB_2 thin films are desired for Josephson device fabrication and their implementation in electronic circuits (as it will be more discussed in Chapter 5). To achieve a stable MgB_2 phase and crystalline films a deposition at high substrate temperatures (e.g. 600-800°C) is necessary. This brings up a number of difficulties that need to be surpassed. The high Mg vapor pressure makes this element very volatile and a very high Mg pressure is needed to overcome the Mg loss. Furthermore, the very low Mg sticking probability at temperatures higher than 300°C requires even higher Mg overpressure. Additionally, Mg and B show very pronounced affinity to the residual oxygen in the deposition chamber, making the realization of MgB_2 films more complicated.

A major materials issue in MgB_2 thin film growth is the MgB_2 phase stability. Magnesium has an extremely high vapor pressure at relatively low temperatures as given in Fig. 4.1(a), making this material very volatile. As the melting point of Mg is 649°C, generally Mg vapor sublimes from the solid, rather than evaporating from the melt [1]. As a result, a certain Mg vapor pressure is necessary to make MgB_2 thermodynamically stable at high temperatures. The volatility of Mg, however, also brings a benefit. It allows the automatic composition control in the so-called adsorption-controlled growth [2]. As long as the Mg to B ratio is large enough, the composition in the film will remain 1:2 and extra Mg will be in the gas phase and pumped away.

From the phase diagram (Fig. 4.1(b), from [3]) it can be concluded that the deposition of single-phase MgB_2 becomes possible when the growth conditions (substrate temperature and overpressure) fall within a window, where the thermodynamically stable phases - the desired MgB_2 phase and gas phase are formed. Within this window MgB_2 does not decompose and excess Mg does not condense on the surface. To ensure crystalline growth, the deposition should take place at sufficiently high temperature. The optimum temperature for epitaxial growth is typically about half the melting temperature (expressed in Kelvin) [4]. Thermodynamic calculation shows that MgB_2 melts at 2430°C (~ 2700 K) with an equilibrium vapor pressure exceeding 49000 Torr [3]. Therefore, the optimum temperature for the epitaxial MgB_2 deposition should be ~ 1080°C (1350 K). To stabilize MgB_2 at this temperature, an Mg partial pressure of at least 11 Torr is required [3]. This pressure corresponds to a Mg deposition rate of 0.5 mm/s (if all Mg atoms would stick), which is not possible for most thin film deposition techniques [3]. It can be seen from the phase diagram that already for a growth temperature of 600°C, the necessary Mg overpressure is 0.9 mTorr, which corresponds to a Mg growth rate of 500 Å/s. These conditions favor

deposition techniques that can maintain a high Mg overpressure during the deposition.

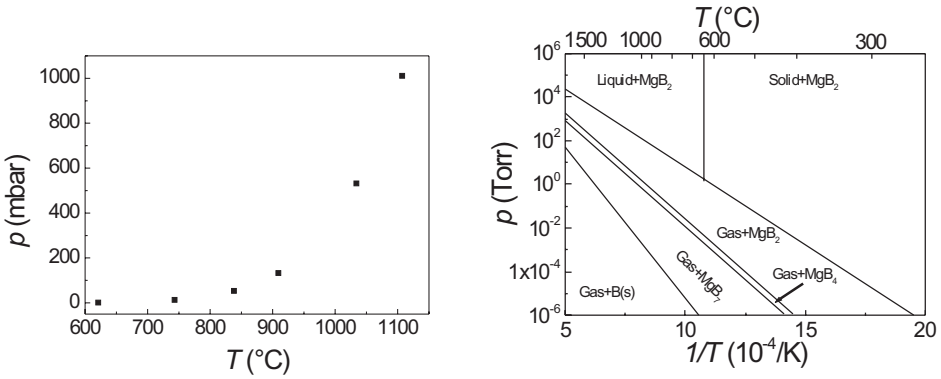

(a) *(b)*

Fig. 4.1 *(a) Vapor pressure of Mg at different temperatures. Data originates from Handbook of Chemistry and Physics [5]; (b) The 'Gas + MgB_2' region is the thermodynamic stability window for the deposition of MgB_2 films in the pressure-temperature phase diagram for Mg:B atomic ratio $x_{Mg}/x_B \geq ½$. (from [3]).*

Kim et al. [1] investigated the sticking coefficient of Mg during MgB_2 thin film fabrication (Fig. 4.2(a)). The Mg sticking coefficient drops to almost zero above 300°C. On the other hand, boron shows no change in the sticking coefficient as temperatures changes. The low sticking probabilities imply that there is only a small probability that Mg reacts with B to form the non-volatile MgB_2 compound. Therefore, a very high Mg flux is needed to ensure enough Mg to react with B.

The reactivity of Mg to oxygen is illustrated in Fig. 4.2(b) [6]. This Figure presents the Gibbs energy of Mg reacting with oxygen to form MgO. Compared to silicon, which oxidizes very easily, the value of the Gibbs energy is even more negative indicating that Mg reacts very strongly with oxygen. This reaction reduces the effective Mg vapor pressure (if oxygen is present) thus pushing the system to the thermodynamically unstable region [3] and forming MgO, which incorporates in the films and limits the MgB_2 grain growth. In the case of vacuum-deposition techniques, an ultra-high vacuum system is needed to make the deposition successful, because the oxygen contamination in non-UHV systems can severely influence the deposition of MgB_2 films [3].

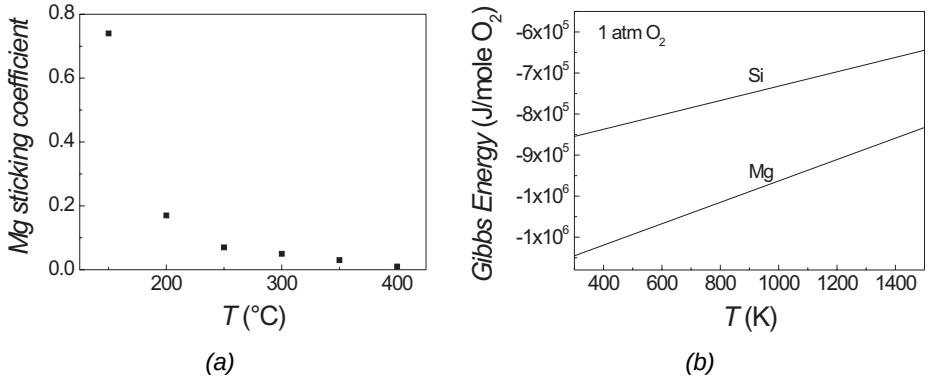

Fig. 4.2 *(a) Sticking coefficient of Mg at different temperatures at a Mg flux of 1 Å/s in MgB_2 thin film deposition by PLD of B and evaporation of Mg from a Knudsell cell (from [1]); (b) Reactivity of Mg with oxygen (from [6]).*

Ueda et al. [7] reported the role of the residual gases in the growth of MgB_2 by Molecular Beam Epitaxy (MBE). Their experiments showed that the residual oxygen is very harmful to the film growth even with a partial pressure as low as $1x10^{-9}$ mbar. Residual hydrogen and nitrogen, on the other hand, have a negligible or even a slightly favorable effect on the MgB_2 film growth. The introduction of H_2 (in order of 10^{-6} Torr) improved the T_C by about 1 K, although the origin of this slight improvement is unclear. It is conceivable that hydrogen may prevent Mg from oxidation.

This Chapter explores the aspects of MgB_2 thin film growth. They are essential in fabrication of superconducting thin films, whose importance for electronic application is addressed in Chapter 2.

To grow MgB_2 we supply Mg and B during the deposition. In this Chapter we want to investigate the aspects of the deposition: the plasma formed by pulsed-laser ablation of Mg and Mg-enriched MgB_2 targets, and the influence of impurities by investigating the oxidation of B.

4.2 Properties of Mg and Mg-enriched MgB_2 plasma

From our first experiments [8] it was noticed that the color of the plasma (formed by pulsed-laser ablation of Mg and Mg-enriched MgB_2 target) was dependent on deposition conditions and varied from intense blue to green. We noticed that the color of the plasma can be used as an indicator for the species inside the plasma and it was found to be important for achieving the superconducting phase in the films. In the papers [9-11] it was presented that the

blue plasma is due to the presence of an ionic Mg II line (blue line at 448 nm), whereas the green color is attributed to the presence of a neutral Mg I line (green line at 518 nm) in the spectra. Our experiments showed that in the range of the deposition parameters where the plasma was blue, the superconducting films were achieved [8].

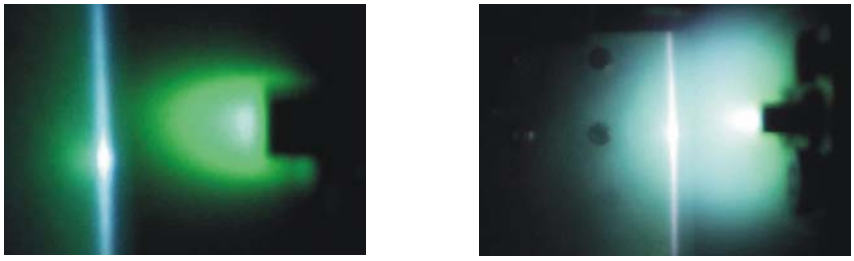

(a) *(b)*

Fig. 4.3 *Ablation of Mg target at 6 J/cm^2: (a) Green plasma color in Ar pressure of 10^{-3} mbar; (b) Blue plasma color in Ar pressure of 0.22 mbar. The bright blue line is a reflection from a stainless steal plate in the chamber.*

The color of the plasma depends on the ambient gas, its pressure and laser energy density (Table 4.1) [12]. By varying the background-pressure of argon gas, the color of the plasma-plume is altered from intense green for low pressures, to a bright blue for intermediate pressures (Fig. 4.3) and a mixture of green and blue for higher Ar pressures [8]. In the case of ablation of Mg-enriched MgB_2 targets, the color of the plasma varied also from green to blue, since the spectra consist mainly of neutral B and Mg lines (B I and Mg I lines), with some contributions from their excited ions (B II and Mg II lines). The plasma emission in the visible range can be mainly attributed to Mg I and Mg II lines, because the most intense B lines are in the UV spectral range [9]. *Amoruso et al*. [13] studied the dynamics of the plasma generated by pulsed-laser irradiation of a MgB_2 target, both, in vacuum and at different Ar pressures, by optical emission spectroscopy. Their analysis of the time-resolved emission of selected species shows that the Ar background gas strongly influences the plasma dynamics. Above 0.1 mbar, the plasma propagation into Ar leads to the formation of blast waves causing, both, an increase of the fraction of excited Mg atoms and a simultaneous reduction of their kinetic flux energy. This was accomplished by a change in the color of the plasma, indicating the importance of this parameter.

Table 4.1 *Dependence of the color of Mg plasma on ambient gas, its pressure and laser energy density; 4.5 and 6.0 correspond to gas purity of 99.995% and 99.9999%, respectively. Similar effects have been observed for Ar + 4% H_2 (purity 99.995%).*

Gas	***p*** **(mbar)**	$E_{density}$ **(J/cm^2)**	**Spot size (mm^2)**	**Plasma color**	
Ar (4.5)	0.10	6	5.96	Green	
	0.20			Blue	
	0.30			Green, blue*	
Ar + 4% H_2 (6.0)	0.05	6	5.25	Green	
	0.10			Blue, green**	
	0.15			Blue, green**	
	0.20			Blue	
	0.25			Blue	
	0.30			Blue	
	0.35			Blue, green**	
	0.40			Blue, green**	
Ar + 4% H_2 (6.0) Ar (4.5)	0.10	13	2.95	Bright blue Blue, green**	
Ar + 4% H_2 (6.0)	0.10	13	2.95	Bright blue	Increa-sing green contrib-ution ↓
		10		Blue, green**	
		8		Blue, green**	
		6		Blue, green**	
		4		Blue, green**	
Ar + 4% H_2 (6.0)	0.10	10	2.95	Blue, green**	Increa-sing green contrib-ution ↓
			1.23	Blue, green**	

** Denotes a mixture of dominating green plasma and some blue parts*

*** Denotes a blue plasma color with a presence of green color in outer shell as well as sometimes in its core*

The use of additional H_2 into Ar ambient gas (both purities 99.995% and 99.9999%) has broadened the range of pressures where the Mg plasma was blue (Table 4.1). This broadening can be attributed to the getter effect of hydrogen towards residual oxygen lowering the oxygen partial pressure in the chamber. The blue plasma with green parts at 13 J/cm^2 laser energy density in Ar environment turned into a bright blue at the same energy density in Ar + 4%

H_2 (purity 99.9999%, Table 4.1), which clearly demonstrates that the additional hydrogen-gas significantly increases the blue component in the plasma. Decreasing of the laser energy density at the target caused the increase of a green halo in the plasma. Reducing the spot size, while keeping the other parameters constant, resulted in an increased amount of green color present in plasma. A smaller spot size requires an increase of the energy density to ensure the blue plasma.

The optimal Ar or mixture of Ar and H_2 pressures to obtain the desired blue plasma depends on the system used (i.e. due to the difference in the laser parameters), which explains the different pressure values achieved in systems used by different researchers. From our experiments we concluded that a certain threshold of both, laser energy density and deposition pressure, is needed to achieve a higher degree of ionization of the plasma. A higher ambient pressure leads to an increase in recombination of Mg ions and, therefore, an increase of the neutral Mg I line present in the plasma. However, more spectroscopic measurements should be done on Mg plasma to confirm these anticipations.

To summarize, the color of the Mg plasma is very sensitive to deposition parameters, i.e., laser energy density, ambient gas and its pressure, and should be adjusted to allow for sufficient ionic emission. The pressure of the ambient gas (Ar or Ar + 4% H_2) also strongly influences the plasma dynamics in plasmas originating from Mg or Mg-enriched MgB_2 targets. According to experimental observations, the gas pressure for certain laser energy should be tuned to achieve the blue color that is favorable for formation of the superconducting phase in MgB_2 thin film deposition.

4.3 Boron oxidation

To study the influence of impurities, both, coming from the ambient gas and the deposition system, we investigated oxygen incorporation in the boron films. As mentioned in the Introduction, the oxidation of boron influences the formation of the superconducting MgB_2 phase.

To investigate the sensitivity of boron to oxidation, films deposited by pulsed-laser deposition and RF magnetron sputtering from pure boron targets were analyzed by XPS. First, the films were prepared by pulsed-laser deposition using a 99.9% pure boron target (Table 4.2) for 10 min at 25 Hz laser frequency in 0.22 mbar of Ar or in 0.2 mbar of Ar + 4% H_2 (purity 99.995% and 99.9999%). The target-substrate distance was 4.2 cm, resulting in a deposition rate of ~ 10 nm/min. We chose a Si substrate with removed native oxide layer to avoid the reaction of oxygen with B. The native oxide layer on the Si wafer was removed by etching the substrate in 1% hydrofluoric acid (HF). We used systems with

different background pressures to investigate the sensitivity of B to residual oxygen [12,14].

Table 4.2 *Boron to oxygen ratio (from XPS data) in the films prepared by PLD of boron target in different background pressures and ambient gases at room temperature; 4.5 and 6.0 correspond to gas purities of 99.995% and 99.9999%, respectively. The presented results are determined from the XPS depth profile, i.e., inner part of the film (about 4 nm under the film surface)[1] when the amount of B and other elements saturate to avoid the surface effect.*

Substrate	$p_{background}$ **(mbar)**	**Gas**	p_{dep} **(mbar)**	**Ratio (B:O)**
	1×10^{-7}	Ar	0.22	0:1
Si	3×10^{-8}	Ar + 4 % H_2 (4.5)		0.77:0.23
(1 % HF etched)	5×10^{-9}	Ar + 4 % H_2 (4.5)	0.2	0.82:0.18
	5×10^{-9}	Ar + 4 % H_2 (6.0)		0.89:0.11

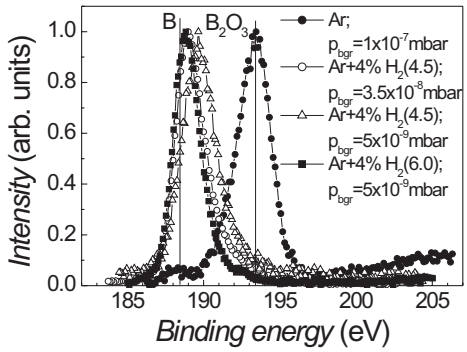

Fig. 4.4 *XPS measurement of the samples deposited by PLD on Si in different background pressures and ambient gases (shown in Table 4.2). The intensities of the B1s peak are normalized. p_{bgr} notes the background pressure. Solid lines present the literature values for B (188.3 eV) and B_2O_3 (193.3 eV) peaks from NIST XPS Database [15].*

The ablation in Ar resulted in the formation of B_2O_3 films, as revealed by XPS measurements on the films, which leads to the conclusion that the oxygen is mainly originating from the background atmosphere in the chamber, possibly in the form of residual water vapor.

[1] The results presented in Table 4.3 and Table 4.4 are determined from the XPS depth profile in the same way.

XPS measurements of films prepared in a base pressure of 10^{-8} mbar prior to deposition and Ar + 4% H_2 (purity 99.995%) as ambient gas resulted in an intensity ratio of the boron 1s line to the oxygen 1s line of 0.77:0.23 (Table 4.2 and Fig. 4.4). The addition of hydrogen-gas to Ar significantly reduces the amount of residual oxygen and consequently the amount of B_2O_3 present in the film, allowing the formation of B. The higher vacuum conditions prior to deposition (base pressure of $5x10^{-9}$ mbar) resulted in an increase of the B:O ratio of 0.82:0.18. A significant increase of the amount of B (almost 0.9:0.1 of B to O ratio), was achieved in Ar + 4% H_2 (purity 99.9999%) using a background pressure of $5x10^{-9}$ mbar.

We noticed a shift of the position of the B peak compared to values mentioned in literature. A O1s peak[2] originating from B_2O_3 (533.0 eV [16]) was taken as a reference peak in the XPS analysis. An inaccuracy in its determination could cause the shift of the boron peak from literature value of B (188.3 eV [15]) in Fig. 4.4. There is also a possibility that oxygen does not entirely come from the B_2O_3 compound, which could be an additional reason for the inaccuracy, i.e., shift of the B peak.

The broadening of the peaks can be attributed to the possible reaction of B with carbon (up to 10%) and oxygen (making other oxides than B_2O_3) and formation of some compounds, which peaks overlap or superposition with the B peak. For example, the binding energy of B_4C is 186.9 eV [15] and that of B_xO ($1<x<6$) is 188.0 eV [15]. The presence of these compounds could not be detected in XPS data due to their overlap and/or superposition with the B peak.

A similar effect was observed in films obtained by RF magnetron sputter deposition from a 99.9% pure B target. The films were deposited for 30 min on Si (1% HF etched) substrates with an RF power of 100 W on the target with a diameter of 2" and analyzed by XPS. The target to substrate distance was about 4 cm and the angle between target and substrate was 60°[3]. The effect of different ambient gases, their purity, and background pressure has been presented in Table 4.3 and Fig. 4.5. The additional H_2 in the Ar gas significantly reduces the amount of B_2O_3 in the film. The purity of Ar + 4% H_2 gas is important as well, since the film deposited in the purer gas contains more boron. However, the base pressure of $2x10^{-7}$ mbar is not sufficient for the deposition of the film that contains more than 0.7:0.3 boron to oxygen ratio.

Table 4.4 and Fig. 4.6 illustrate the dependence of the RF magnetron sputtering power, ambient gas, its pressure and substrate temperature on boron to oxygen ratio present in the films deposited on Si (1% HF etched substrate)

[2] The maximum positions of all O1s peaks from the depth profile were determined. The average of these maximum positions was taken as a reference position of O1s peak.

[3] The sputter gun was under the angle of 60° with respect to the heater surface normal, since this configuration was used for the experiments in MgB_2 thin film deposition with combined technique: PLD of Mg and sputter deposition of B (as it will be further described in Section 5.2.4).

under the angle of 45°[4] with target normal. Target-substrate distance was about 7.5 cm. Due to the different geometry of this system compared to the geometry of the system where the previous sputter deposition has been done (longer target-substrate distance and smaller target-substrate angle) a lower deposition rate of the film is expected. To obtain approximately the same film thickness, the deposition time was longer: 1h for samples prepared at room temperature and 2 h for a sample made at 500°C. The deposition rate at room temperature was about 0.7 nm/min.

Table 4.3 *Boron to oxygen ratio from XPS data of the films made by RF magnetron sputtering of boron target in different background pressures and ambient gases at room temperature; 4.5 and 6.0 correspond to gas purity of 99.995% and 99.9999%, respectively. Angle between target and substrate is 60°.*

Substrate	$p_{background}$ **(mbar)**	**Gas**	p_{dep} **(mbar)**	**Ratio (B:O)**
Si (1 % HF etched)	4×10^{-7}	Ar (4.5)	0.14	0:1
	2×10^{-7}	Ar + 4 % H_2 (4.5)		0.56:0.44
	2×10^{-7}	Ar + 4 % H_2 (6.0)		0.70:0.30

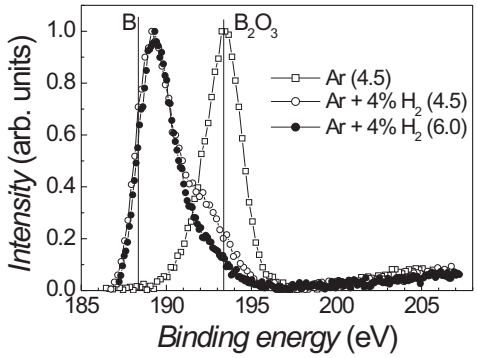

Fig. 4.5 *XPS measurement of the samples presented in Table 4.3. The intensities of B1s peak are normalized. Solid lines present the literature values for B and B_2O_3 peaks from NIST XPS Database [15].*

Higher RF power enlarges the B flux and in this way enables a shorter exposure of sputtered B to the residual oxygen and, subsequently, a higher amount of B present in the film. This caused the increase of about 0.06 of boron

[4] The deposition was done under the different angle compared to the previously described one, since the different deposition system for the combined technique is used.

in B to O ratio in the base pressure lower than $5x10^{-9}$ mbar. The film made at an RF power of 150 W in the base pressure of 10^{-8} mbar contains more B_2O_3 than the film made in 10^{-9} mbar. The background pressure should be lower than 10^{-9} mbar to avoid the formation of B_2O_3. Taking into account that the melting point of B_2O_3 is 450°C, the substrate temperature of 500°C (Table 4.4) significantly increases the B to O ratio compared to the ratio in the films prepared at room temperature.

Table 4.4 *Boron to oxygen ratio from XPS data of the films prepared by RF magnetron sputter deposition of boron target in different background pressures, RF power densities and substrate temperature. Angle between target and substrate is 45°; 6.0 denotes the gas purity of 99.9999%; RT stands for room temperature.*

Subs-trate	**RF power (W)**	***T*** **(°C)**	$p_{background}$ **(mbar)**	**Gas**	p_{dep} **(mbar)**	**Ratio (B:O)**
Si (1 % HF etched)	50	RT	$< 5 \times 10^{-9}$	Ar + 4 % H_2 (6.0)	0.1	0.71:0.29
	150	RT	1×10^{-8}			0.72:0.28
		RT	$< 5 \times 10^{-9}$			0.77:0.23
		500	$< 5 \times 10^{-9}$			0.97:0.03

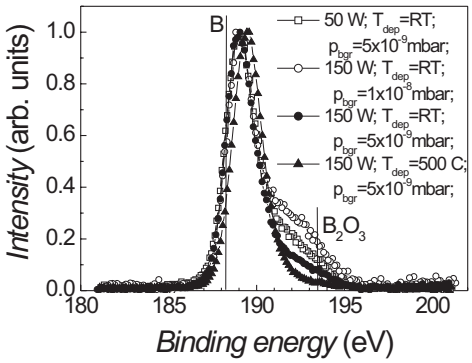

Fig. 4.6 *XPS measurement of the samples given in Table 4.4. The intensities of B1s peak are normalized. Solid lines present the literature values for B and B_2O_3 peaks from NIST XPS Database [15].*

The highest boron to oxygen ratio is present in the films prepared in the high-vacuum conditions prior to deposition and with the use of Ar + 4% H_2 gas with the highest purity. However, the B to O ratio is not as high as in the films prepared by PLD of a B target at room temperature. It is beneficial to have a higher deposition rate, which is achievable by PLD. Different system geometries

play a significant role as well. The deposition done under the angle of 45° or 60° (in the case of sputter deposition) reduces the deposition rate compared to on-axis deposition as in the case of PLD of B. The low deposition rate allows the material more time to react with residual oxygen in the chamber and with other impurities. The fabrication of films at temperatures higher than the melting temperature of B_2O_3 resulted in 0.97:0.03 boron to oxygen ratio even by sputter deposition.

Summarizing the results, the large affinity of boron and magnesium to oxygen emphasizes the need of a base pressure in the chamber smaller than 10^{-9} mbar. This is also in line with the experiments of *Ueda et al*. [17], who obtained up to now the highest T_C of 36 K for *in-situ* grown MgB_2 thin films by MBE and e-beam evaporation in systems with a base pressure of 10^{-9} to 10^{-10} mbar. The work of *van Erven et al.* [18] supports this. They found that, independent of the growth parameters, all the films grown by MBE at a pressure higher than ~ $3x10^{-8}$ Torr showed insulating behavior. The specific window of growth parameters in which superconducting films were formed became larger with a lower background pressure. In addition, our results show that the use of high purity Ar + 4% H_2 as an ambient gas could improve the film quality by minimizing the amount of impurities in the films.

4.4 Substrate selection

Although some applications of MgB_2 thin films do not require epitaxial growth, it is strongly desired in the case one wants to make use of the exceptionally large I_CR_N product for tunneling in the *a-b* direction [19] and the low-resistive behavior in the normal state. Furthermore, the reproducibility and reliability of all Josephson devices will rely on the degree of epitaxy and smoothness of the MgB_2 thin films, underlining the need for an epitaxial growth procedure [20]. To achieve epitaxial growth, the films need to be grown at high substrate temperature (e.g. 600-800°C). Therefore, it is necessary to choose a substrate, which does not react with MgB_2 film at the elevated temperatures.

In epitaxial growth, the substrate choice is of utmost importance. MgB_2 has a hexagonal structure, with Mg and B planes stacked alternately along the c-axis, and therefore, it is understandable that the substrates with a hexagonal lattice at the surface provide better results [7]. Table 4.5 gives an overview of materials with hexagonal structure, which are suitable as substrates or interlayers to ensure the epitaxial growth of MgB_2. The *a*-to-*a* alignment between MgB_2 and Al_2O_3 results in ~ 23 % lattice misfit being unfavorable for the epitaxial growth. But, a 30° angular off the *a*-to-*a* alignment between the basal plane of MgB_2 and Al_2O_3 results in a smaller lattice misfit (~ 10%) between the MgB_2 thin

film and the (0001) Al_2O_3 substrate that possibly allows the epitaxial growth [22]. Because of the smallest lattice misfit SiC is the most suitable material. Its elementary structural unit is a C-Si tetrahedron. SiC has over 170 polytypes, determined by the stacking sequence of the C-Si bilayer with a hexagonal structure [23]. If the first bilayer is called the ''*A*'' position, the next bilayer can be placed in ''*B*'' position. The stacking sequences for the polytypes 4H-SiC are *AABB* and for 6H-SiC are *AAABBB* [24]. Both have a hexagonal structure with the *a* lattice parameters close to the *a* lattice parameter of MgB_2 (Table 4.5). An (0001) orientation (c-cut) of both polytypes provides a hexagonal lattice with a close lattice match to MgB_2.

Table 4.5 *The list of some substrates and/or interlayers with a hexagonal structure, their lattice parameters and lattice misfit with a-axis lattice parameter of MgB_2. A positive sign of the lattice misfit denotes that the epitaxial film will be stretched in tension and a negative one means the film comprehension. The lattice parameters data originate from Inorganic Crystal Structure Database [21].*

Material	**Lattice parameters (Å)**	**Lattice misfit for *a*-to-*a* alignment**
MgB_2	a = 3.086 c = 3.524	-
Al_2O_3	a = 4.77 c = 13.04	-23 %
TaN	a = 5.170 c = 2.890	-6.5 %
GaN	a = 3.190 c = 5.189	-3.3 %
AlN	a = 3.110 c = 4.980	-0.8 %
Si	a = 3.800 c = 6.269	23 %
TiB_2	a = 3.028 c = 3.228	1.8 %
SiC (4H)	a = 3.073 c = 10.053	0.42 %
SiC (6H)	a = 3.081 c = 15.12	0.16 %

The substrate cut defines the shape of the surface and its importance can be illustrated in the following example. Si (111), SiC, Al_2O_3 (c-plane) and MgO

(111) have a hexagonal surface, which makes them more suitable for MgB_2 growth compared to, for instance, Al_2O_3 (r-plane), $SrTiO_3$ (100) and MgO (100), which have square or rectangular surface crystallinity.

Table 4.6 *The reactivity of the Mg vapor with various substrates (from [25]). Calculated reactivity was in the temperature range of about 830-1250℃ [25]. bcc stands for body-centered cubic, hcp-hexagonal close packed and fcc-face-centered cubic structure. S2 denotes the middle temperature structure (the structure in the temperature range of 930-1050℃) and S3 the high temperature structure (the structure in the temperatures higher than 1050℃).*

Classification	**Substrates**	**Calculated Reactivity**	**Experiments [26]**	
			873 K	**1073 K**
Non-reactive	MgO	No reaction	No reaction	No reaction
	SiC	No reaction	No reaction	MgB_2 with altered size
	AlN	No reaction	No reaction	No reaction
	TaN	No reaction	No reaction	No reaction
Semi-reactive	Si	Mg_2Si or no reaction	Mg_2Si	Mg_2Si, MgB_4
	ZrO_2	MgO, bcc, hcp or no reaction	No reaction	No reaction
	TiN	Mg_3N_2 or no reaction	No reaction	No reaction
Reactive	SiO_2	MgO, Mg_2Si, Si	MgO, Si	Mg_2Si, MgB_4, MgO, Si
	Al_2O_3	MgO, Al_2MgO_4, fcc	No reaction MgO, Al_2MgO_4 (from [22])	MgO, unknown
	GaN	Mg_3N_2_S2, Mg_3N_2_S3	-	-

Besides lattice matching, the reactivity between substrate and thin film also has to be taken into account. Table 4.6 gives an overview of the calculated reactivity of the substrates with Mg vapor [25] and the experimental observations [26]. *Liu et al*. [25] divided the substrates into 3 categories depending on their reactivity with Mg vapor. They concluded that MgO, SiC, AlN and TaN substrates are stable substrates for MgB_2 deposition with no reaction between Mg vapor

and the substrate. Additionally, AlN and TaN have a rather small misfit with MgB_2 (Table 4.5). The Mg vapor partially reacts with the Si, ZrO_2 and TiN substrates. However, if the Mg pressure is low enough these substrates can remain stable in the Mg vapor. There are reactions between Mg vapor and SiO_2, Al_2O_3 and GaN substrates.

It can be concluded that one of the most promising candidates of the substrates for epitaxial MgB_2 growth is SiC because of its perfect lattice match with MgB_2. *He et al.* [25] found MgB_2 with altered cell size deposited on SiC at 1073 K (Table 4.6). This could be explained by the possible doping of carbon, which decreased the superconducting temperature [27]. To prevent carbon doping TiB_2 could be used as a buffer layer. Zhai *et al.* [28] fabricated high quality layers on SiC by PLD, which forms the low lattice misfit. Owing to the strong similarities of MgB_2 with TiB_2 (both with respect to crystalline structure, lattice parameter and bonding nature), low-resistive TiB_2 could be a promising material for MgB_2-based heterostructures (superconductor-metal-superconductor junctions) and can be used as a protective coating for MgB_2 (as required by rapid degradation of MgB_2 in contact with water [29] etc.). However, its stability in MgB_2 thin film fabrication should be further investigated.

4.5 Conclusions

For achieving the epitaxial growth of MgB_2 thin films, needed for multilayered structures to be used in electronic devices, deposition at elevated temperatures is a prerequisite. A number of difficulties in thin film fabrication are faced then.

The high Mg vapor pressure i.e. volatility of this element and low Mg sticking probability at elevated temperatures significantly limits the deposition temperature and subsequently influences the epitaxial growth. A high deposition temperature requires a very high Mg overpressure, i.e., high Mg flux, to compensate for its loss. This favors deposition techniques that can provide such a high Mg overpressure during deposition.

We showed that B is very sensitive to residual oxygen in the chamber and in ambient gas. A higher B flux is obtained in PLD from a B target compared to sputter deposition of B, which reduces the oxidation of B. To form MgB_2 with a very high B flux, even higher Mg fluxes are needed, which is not achievable by PLD. In very high purity systems, the B flux does not have to be very high, which implies that high enough Mg flux can be achieved. An essential aspect to attain superconductivity in the films is to prevent oxidation of the Mg and B in the plasma and deposited film by the use of ultra-high vacuum systems (background

pressure need to be lower than 10^{-9} mbar) and the high purity mixture of Ar and 4% H_2 as an ambient gas.

The color of the plasmas originating from Mg and Mg-enriched MgB_2 targets is an indicator of its constituents. The superconducting MgB_2 phase is reached by preparing the films in a blue plasma, which is achieved by tuning the deposition parameters, such as the pressure of the ambient gas (Ar or mixture Ar and H_2 gases) in the deposition chamber and laser energy density at the target. The optimum deposition parameters were about 0.2 mbar of the ambient gas at 6 J/cm^2.

References:

[1] J. Kim, R. K. Singh, N. Newman and J. M. Rowell, IEEE Trans. Appl. Supercond. **13**, 3238 (2003).

[2] X. X. Xi *et al*., IEEE Trans. on Appl. Supercond. **13**, 3233 (2003).

[3] X. X. Xi *et al*., Supercond. Sci. and Technol. **15**, 451 (2002).

[4] M. H. Yang and C. P. Flynn, Phys. Rev. Lett. **62**, 2476 (1989).

[5] *Handbook of Chemistry and Physics*, 55th edition, CRC Press, (1974).

[6] X. X. Xi and Z. K. Liu, private communication; X. X. Xi, *Progress in the Deposition of MgB_2 Thin Films*, oral presentation at EUCAS conference (2003).

[7] K. Ueda and M. Naito, J. Appl. Phys. **93**, 2113 (2003).

[8] A. Brinkman *et al*., Physica C **353,** 1 (2001).

[9] V. Ferrando *et al*., Supercond. Sci. Technol. **16**, 241 (2003).

[10] L. Dirnberger, P. E. Dyer, S.R. Farra and P.H. Key, Appl. Phys. A **59**, 311 (1994).

[11] V. N. Tsaneva, N. A. Stelmashenkom, I. N. Martev, Z. H. Barber, M. G. Blamire, Vacuum **69**, 267 (2003).

[12] D. Mijatovic *et al*., Appl. Phys. A (COLA03 proceedings) (2004), in press.

[13] S. Amoruso *et al*., Appl. Phys. Lett. **80**, 4315 (2002).

[14] D. Mijatovic *et al*., IEEE Trans. on Appl. Supercond. **13**, 3245 (2003).

[15] From National Institute of Standards and Technology (NIST) XPS Database: www.nist.gov.

[16] V. I. Nefedov *et al*., Zh. Neorg. Khim. **20**, 2307 (1975).

[17] K. Ueda and M. Naito, Appl. Phys. Lett. **79**, 2046 (2001).

[18] A. J. M. van Erven T. H. Kim, M. Muezenberg and J. S. Moodera, Appl. Phys. Lett. **81**, 4982 (2002).

[19] A. Brinkman *et al.*, Phys. Rev. B **65**, 180517 (R) (2002).

[20] A. Brinkman *et al*., Supercond. Sci. Technol. **16**, 246 (2003).

[21] ICSD-Inorganic Crystal Structure Database available at the Center for Molecular and Biomolecular Informatics, University of Nijmegen, The Netherlands.

[22] W. Tian *et al*., Appl. Phys. Lett. **81**, 685 (2002).

[23] A. R. Powell and L. B. Rowland, Proc. IEEE **90**, 942 (2002).

[24] A. F. Wells, *Structural Inorganic Chemistry*, Clarendon Press, Oxford (1962).

[25] Z.-J. Liu, S. H. Zhou, X. X. Xi and Z.- K. Liu, Physica C **397**, 3678 (2001).

[26] T. He, R. J. Cava and J. M. Rowell, Appl. Phys. Lett. **80,** 291 (2002).

[27] T. Takenobu *et al*., Phys. Rev. B **64**, 134513 (2001).

[28] H. Y. Zhai, H. M. Christen, C. Cantoni, A. Goyal and D. H. Lowndes, Appl. Phys. Lett. **80,** 1963 (2002).

[29] H. Y. Zhai *et al*., Supercon. Sci. Techol. **14,** 425 (2001).

MgB_2 thin films: fabrication and properties

5

Abstract

In the deposition of the superconducting MgB_2 thin films a number of difficulties, such as the high Mg vapor pressure, the high Mg and B affinity to oxygen, and the low sticking coefficient of Mg at elevated temperatures, are faced.

MgB_2 thin films were made by PLD in a two-step in-situ method: depositing the films at low substrate temperature followed by high-temperature annealing. The films had reduced critical temperatures compared to the bulk value, which can be attributed to the presence of impurities in the films (such as O, C…), very small grain sizes of MgB_2 etc. Determination of the electron mean-free path showed that these films are in the dirty limit.

In the HPCVD, a high Mg overpressure is easily attained. This enables epitaxial growth at high temperatures. Epitaxial films with a bulk-like value of the critical temperature have been obtained by this method. The estimated value of the electron mean-free path showed that these films are in the clean limit.

5.1 Introduction

The availability of superconducting thin films is of a great importance for Josephson junction fabrications and further implementations in electronic circuits. Smooth and crystalline thin films are desired for fabrication of superconducting devices relying on multilayer technology. For example, the barrier thickness in trilayer Josephson junctions is in the range of a few nanometers. The surface roughness of the film should be smaller than this. Furthermore, the films should be homogeneous without precipitates.

Ideally *in-situ* epitaxially grown MgB_2 thin films with bulk-like T_C values are desired. To achieve epitaxial growth, the films must be deposited at a high substrate temperature. The deposition conditions that are needed for fabrication of the films that would fulfill all the requirements are not easy to obtain due to a high Mg vapor pressure and a low sticking coefficient at high temperatures (as discussed in Chapter 4). A high Mg and B sensitivity to oxygen additionally complicate the MgB_2 formation.

Several deposition procedures are used to fabricate superconducting MgB_2 thin films. Roughly speaking, there are six different approaches that led to successful deposition of MgB_2 [1]:

1. *ex-situ* post-anneal of boron films in magnesium overpressure (e.g., [2-4]);
2. *ex-situ* post-anneal of Mg-B films in magnesium overpressure (e.g., [5]);
3. *in-situ* post-anneal of Mg-B films (e.g., [6-10]);
4. *in-situ* post-anneal of Mg-B multilayers (e.g., [11,12]);
5. *in-situ* vacuum techniques (such as sputter deposition, Molecular-Beam Epitaxy (MBE)) deposition with high Mg flux (e.g., [13-15]);
6. *in-situ* Chemical-Vapor Deposition (CVD) (such as Hybrid Physical-CVD method (HPCVD)) deposition with high Mg flux (e.g., [16,17]).

In approach 1 a boron layer is deposited with, for instance, MBE or PLD, at elevated temperatures. The film is annealed in a high-pressure cell (typically 7-10 Torr of Ar [3]) with a Mg pellet at 900-950°C for 1 h. The obtained T_C are comparable with bulk values, namely ~ 39 K. During the diffusion of the Mg into the boron film, large grains and outgrowths occur. This morphology and the large surface roughness are clearly illustrated by the SEM pictures in [18]. The surface roughness is too large to use these films in multilayer configurations.

In approach 2 the starting film is usually made by PLD or sputter deposition using a composite MgB_2 target. The obtained film, often made at room temperature, already contains both constituents, Mg and B. These films are annealed similar to the first approach, resulting in T_C of ~ 35 K. The somewhat suppressed T_C is partially due to impurities originating from the composite target.

The surface quality reported is often better than the films made with the first approach, despite the lower T_C.

Approach 3, known as the two-step *in-situ* deposition process, is the most used one up to now and will be discussed in more detail in the next Section. The obtained T_C is suppressed (~ 30-34 K), but the surface roughness is much better than the post-annealed films. Approach 4 looks very promising, but only a few attempts have been reported till now. The main advantage is the use of the two targets, i.e. boron and magnesium targets, that are purer than the sintered ones.

Approach 5, deposition without any anneal step, has been reported by a few groups. Using MBE, *Ueda and Naito* [14] and *Jo et al.* [15] succeeded in MgB_2 thin film deposition. The success of this approach is in the low background pressure and a very high magnesium flux. However, the maximum deposition temperature was about 300°C, since it was not possible to achieve a sufficiently high Mg flux at higher temperatures. The films reached T_C up to 35 K. Approach 6 employs Hybrid Physical-Chemical Vapor Deposition (HPCVD) [16,17] and results in an epitaxial MgB_2 thin film growth at elevated substrate temperature (720-760°C) with a bulk-like value of the critical temperature.

PLD (approaches 3 and 4) and HPCVD (approach 6) methods are described in more details. During the deposition, it is necessary to compensate for the Mg loss. In the PLD technique a high Mg flux at a high laser repetition rate can be used for it as well as Mg enriched targets. In the HPCVD method a high Mg pressure achieved by the evaporation of solid Mg allow the deposition at high temperatures and therefore the epitaxial growth. The electrical and structural properties and the morphology of the films prepared by those two techniques have been investigated, compared and presented here.

5.2 In-situ MgB_2 thin film fabrication

In this Section two ways of *in-situ* deposition of superconducting MgB_2 thin films are described. In PLD the superconducting phase is achieved by a two-step deposition process: deposition at low temperature ranging from room temperature till 200°C, followed by a high-temperature (~ 600°C) annealing step. The HPCVD method assures higher Mg fluxes, which enables the fabrication of superconducting epitaxial films in one-step at elevated temperatures.

5.2.1 Two-step *in-situ* MgB_2 deposition by PLD

To obtain superconducting films by PLD the so-called two-step *in-situ* method is mostly used. The films have been prepared in two ways: by deposition from a Mg-enriched MgB_2 target (approach 3) and as a multilayer deposition

from Mg and B targets (approach 4). The experiments were performed in a system with a background pressure of 10^{-7} mbar and in Ar ambient gas (detailed analysis of the influence of the background pressure and type of the ambient gas was presented in Chapter 4).

Deposition from a Mg-enriched MgB_2 target

Targets composed of MgB_2 powder enriched with Mg have been used to compensate for the loss of magnesium during the deposition. Targets were prepared from a mixture of 50 vol% Mg powder (Alfa Aesar, purity 99.6%) and 50 vol% MgB_2 powder (Alfa Aesar, purity 98.0%) [6]. These powders were carefully mixed and uniaxially pressed in the form of a pellet. Next, the pellets were sintered in a nitrogen flow for 3 h at 640°C and subsequently for 10 h at 500°C followed by a cool down to room temperature for about an hour. The obtained targets are very dense due to the melting of magnesium during target fabrication.

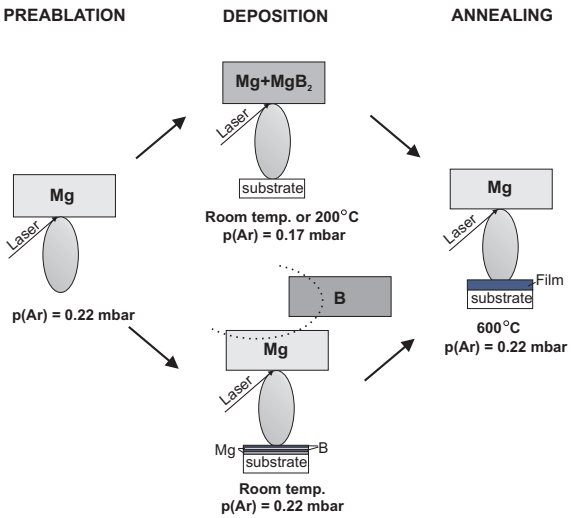

Fig. 5.1 *Schematic view of two different routes to deposit MgB_2 in the two-step in-situ method. This method includes pre-ablation of magnesium to getter the oxygen and post-annealing to form the right phase [1].*

Table 5.1 *Typical deposition parameters in MgB_2 thin film growth by two-step in-situ PLD method.*

Target	Substrate	$E_{density}$ (J/cm^2)	Spot size (mm^2)	T_{dep} (°C)	Annealing temperature (°C)	Annealing time (min)	$T_{C,0}$ (K)
"Mg+MgB_2"	MgO (100) $SrTiO_3$ (100) Si (100) SiC (6H) Al_2O_3 (c-plane)	6	6-8	RT-300	500-600	5-90	20-27
Mg and B (multilayers)	MgO (100) $SrTiO_3$ (111) Al_2O_3 (r-plane)	6	6	RT	600	5	22-28

A typical deposition run is as follows (Fig. 5.1): first a Mg target is pre-ablated for 2 min at 10 Hz in 0.2 mbar of Ar to reduce the oxygen background pressure in the chamber by the getter action of oxygen by Mg. Subsequently, the target composed of a Mg and MgB_2 mixture is pre-ablated for 2 min at 10 Hz in Ar pressure of 0.17 mbar. This pressure is optimized for this target to obtain the blue-colored plasma. The energy density at the target was about 6 J/cm^2. The substrate was placed in front of the target at a distance of 4.5 cm (on-axis geometry). The films are deposited at a repetition rate of 10 Hz for 6 min, yielding an approximate layer thickness of 220 nm. A high temperature-annealing step is needed to form the superconducting phase. Therefore, the films are heated up to T_{ann}= 600°C, kept for 5 min and cooled down to room temperature in 0.2 mbar of Ar. The total annealing procedure is as short as possible to avoid Mg-evaporation out of the film. In the temperature range between 350°C and 600°C, the sample is kept in a pulsed (5 Hz) Mg plasma for the same reason [7].

In principle, one likes to grow the film at temperatures as high as 650°C to achieve epitaxial superconducting films. However, this is not easy in the case of MgB_2 due to the evaporation of the magnesium. The films were deposited at temperatures ranging from room temperature to 300°C [11,7] (Table 5.1). The films deposited at room-temperatures had T_C values of 24-25 K. Higher $T_{C,0}$'s (about 26 K) were achieved when the films were grown at a substrate temperature of 200°C. Films prepared at 300°C, however, were not superconducting. At the deposition temperature of 300°C, the Mg pressure of MgB_2 growth window is from 10^{-8}-10^{-4} Torr (Section 4.1). The sticking coefficient of Mg decreases dramatically when the substrate temperature increases above 300°C (Section 4.1). If there is not enough Mg at the substrate to react with B, MgB_2 cannot be formed. These could explain the limiting success of *in-situ* growth of MgB_2 above 300°C.

Because the anneal step is very critical it has been studied in more details and presented in Table 5.1. Several processes are involved in the *in-situ* annealing: Mg evaporation, MgB_2 phase formation, nucleation and growth of crystallites and MgB_2 decomposition [19]. These processes are determined by the thermodynamics [20] and kinetics [21]. Finding the right balance in these processes by carefully adjusting the heating and annealing parameters is critical. In our experiments a mixture of Mg and B was formed in the as-deposited film. A high temperature annealing step was needed to ensure the formation of MgB_2. At high temperatures a decomposition of MgB_2 is expected [21]. To avoid or reduce it, a Mg plasma was used. Longer annealing also causes a decomposition of MgB_2 and therefore the absence of superconducting properties. If the annealing temperature is too high and/or the annealing time is too long, a low Mg pressure will result in the decomposition of MgB_2. Here, the

kinetic barrier for MgB_2 decomposition plays a particularly important role [21]. A short annealing step (5-10 min) at 600°C (Table 5.1) made the formation of superconducting phase possible. An increase of $T_{C,0}$ ($T_{C,0}$ ~ 27 K) was noticed in the films annealed at 600°C for 10 min in a Mg plasma, followed by a heat treatment at 500°C for 1 h in 0.22 mbar of Ar. X-ray diffraction peaks originating from MgB_2 were not observed in the X-ray diffraction patterns of our samples, but the films were superconducting. The films were probably polycrystalline with very small grain sizes (smaller than 5 nm) even after longer annealing, which is in line with the data available from the literature [22,5].

The T_C's of the films are suppressed compared to the bulk value. The reason for this suppression is under debate since the first publications on thin films appeared. This reduced T_C is at least partially attributed to the very small grain sizes of MgB_2, the presence of MgO inclusions and to possible impurities in the starting material. The Mg pressure locally supplied by this technique is not high enough to stabilize MgB_2 in the film at elevated temperatures and to ensure the formation of larger grains. This is probably caused by a very low sticking coefficient of Mg at elevated temperatures.

The films were grown on various types of substrates (Table 5.1) with different lattice misfit with MgB_2 films (Section 4.4). Since XRD data showed that the films were not epitaxially grown and the transition temperature was similar of all of the samples, it can be concluded that the type of substrate used is not very significant in this method of the deposition [1,11].

The highest T_C reported, using a Mg-enriched MgB_2 target, is obtained by *Xi et al.* [22]. They present a T_C of 34 K. The MgB_2 films were deposited on (0001) Al_2O_3 substrates from targets prepared by pressing Mg powder with MgB_2 powder without sintering. The Mg:MgB_2 molar ratio was varied between 4:1 and 2:1. The films were deposited at 250-300°C in an Ar atmosphere (99.999% gas purity). The energy density of the laser beam was 4 J/cm^2, with a repetition rate of 5 Hz. The deposited films were then annealed at 630°C for 10 min. The pressure during deposition and annealing was 120 mTorr. After the *in-situ* annealing, the films were cooled to room temperature in 20 Torr Ar. Also they could not observe any XRD peaks originating from MgB_2. The absence of XRD peaks in films made with this approach indicates that the grain size of MgB_2 is extremely small, in the order of nanometres. A longer annealing time will increases the grain size, but simultaneously increase the evaporation of Mg and decomposition of MgB_2. The cross section transmission electron microscopy images (TEM) of those samples, reported by *Xi et al.* [22], reveal a nanocrystalline mixture of textured MgO and MgB_2 with very small grain sizes.

Multilayer deposition

In an alternative fabrication procedure, multilayered films were grown from Mg and B targets on several substrates at room temperature (Table 5.1) [11]. The preablation and short annealing procedures were the same as described above. The highest $T_{C,0}$ of 28 K (Fig. 5.1) was obtained by depositing on MgO substrate, magnesium for 1 min at 10 Hz and boron for 3 min at 25 Hz alternatively (10 times). The total thickness of this multilayer was 180 nm. The grain-size is presumably still small, indicated by the absence of XRD peaks. Due to the fact that the two targets are metallic, instead of a composite and therefore purer, it is likely that fewer impurities are incorporated in the film. This could be the reason why the multilayer technique leads to a higher T_C. The non-epitaxial growth and the similar T_C on all three kinds of substrates implies that also in this method the substrate used did not play a crucial role in film growth.

Superconducting thin films were achieved, although according to the XPS results described in Section 4.3, it can be assumed that B_2O_3 films were formed between the Mg layers. Since the samples were annealed at 600°C to form the superconducting phase, it is conceivable that B_2O_3 melted partially during annealing (the melting point of B_2O_3 is 450°C), reacted with Mg and formed the MgB_2 phase with MgO inclusions, resulting in superconducting films with a reduced critical temperature.

5.2.2 MgB_2 deposition by the HPCVD method

Epitaxial MgB_2 films have been prepared at Penn State University by Hybrid Physical-Chemical Deposition (HPCVD) technique in the one-step approach [16,17].

The HPCVD system consists of a water-cooled vertical quartz tube reactor with the inner diameter of 37.5 mm [16,23]. A schematic presentation of the deposition set-up is given in Figure 5.2. A stainless steel susceptor (18 mm in diameter) is situated coaxially with the quartz tube. A single crystal substrate (5x5 mm^2) is placed on the top of the susceptor. Three pieces of bulk Mg (purity 99.95%, weighting about 0.3-0.4 g) are cut from a Mg ingot and placed in a retaining groove. The reactor is first purged with N_2 gas (purity 99.999%) and H_2 gas (purity 99.999%). The susceptor, the substrate and Mg pieces are heated inductively to 718°C in ambient H_2. At this temperature the local Mg pressure is about 11 mbar (see Fig. 4.1(a), Section 4.1). When the deposition temperature is reached a mixture of 1000 ppm B_2H_6 (diborane) in H_2 is introduced into the reactor to initiate the film growth. The total pressure in the reactor is maintained at 100 Torr throughout the process and the total gas flow was kept at 450 sccm

(standard cubic centimeter per minute) flow rate. The B_2H_6 gas mixture flow rate varied from 50 to 150 sccm. When the B_2H_6 gas is not flowing through the reactor, there is no film deposition because of the low sticking coefficient of Mg at high temperatures [14]. When the B_2H_6 gas begins to flow, a MgB_2 film starts to grow on the substrate. The deposition rate depends on the B_2H_6 supply, and increases from about 3 Å/s for a B_2H_6 gas mixture flow-rate of 50 sccm to about 10 Å/s for 150 sccm B_2H_6 gas mixture flow [24]. The film growth is terminated by switching off the B_2H_6 gas mixture before the bulk Mg pieces are completely evaporated, which takes about 10 min, for this size of Mg pieces used. The sample is then cooled in the H_2 carrier gas to room temperature in about 5-6 min. The film composition will be automatically maintained as MgB_2, as long as the Mg vapor pressure is high enough to keep the MgB_2 phase thermodynamically stable and the Mg:B ratio is higher than 1:2. The growth rate of MgB_2 is determined by the rate at which boron is incorporated in the film.

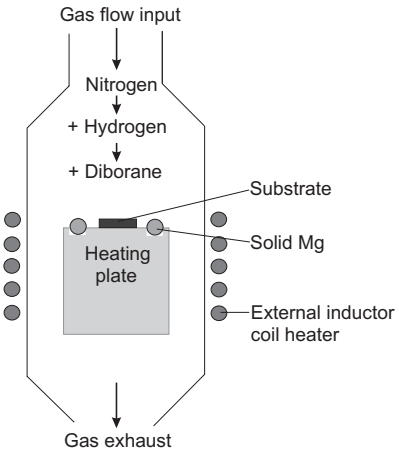

Fig. 5.2 *Schematic of the HPCVD set-up used for MgB_2 deposition (adapted from [17]).*

Films were deposited on (0001) Al_2O_3 (a = 4.765 Å) and (0001) 4H-SiC (a = 3.073 Å) substrates and characterized by XRD (Fig. 5.3). θ-2θ scans along the [*000l*] directions showed that apart from the substrate peaks, the only peaks observed arise from the (0001) planes of MgB_2. This indicates epitaxial MgB_2 films with the *c*-axis normal to the substrate surface. A *c* lattice parameter of 3.52 (1) Å was found for MgB_2 layer deposited on Al_2O_3 substrate and 3.51 (1) Å for MgB_2 film deposited on SiC.

It was observed by XRD that the hexagonal MgB_2 lattice is rotated by 30° with respect to the in-plane axes of Al_2O_3 (i.e., $\left[11\bar{2}0\right]MgB_2 \| \left[10\bar{1}0\right]Al_2O_3$ [25]) to reduce the lattice misfit to approximately 10% (Fig. 5.4; also described in Section

4.4). The *a* lattice constant of the films grown on Al_2O_3 was 3.10 (1) Å, which is a bit larger than the bulk value. The hexagonal lattice of MgB_2 with *a* = 3.09 (1) Å grows directly on top of the hexagonal lattice of SiC owing to the close lattice match between SiC and MgB_2, which was also observed by *Zeng et al*. [16].

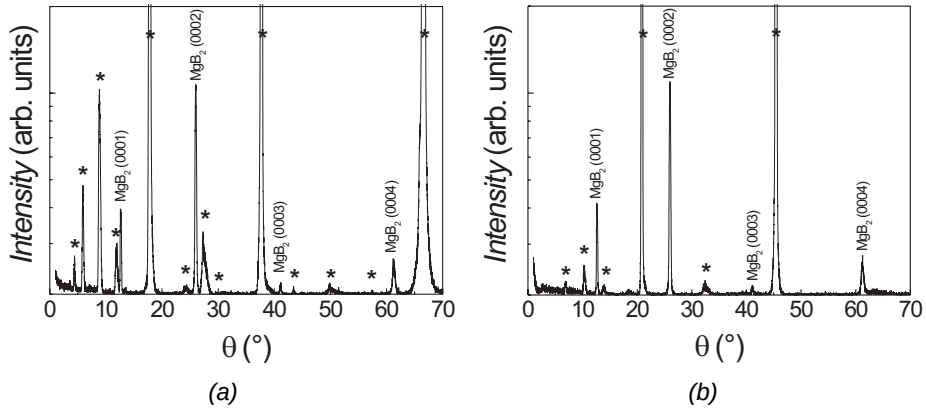

Fig. 5.3 *θ-2θ scan of the MgB_2 films deposited on (a) SiC and (b) Al_2O_3. The substrate peaks are marked by * (including the peaks originating from λ/2 and λ/3 in the primary beam).*

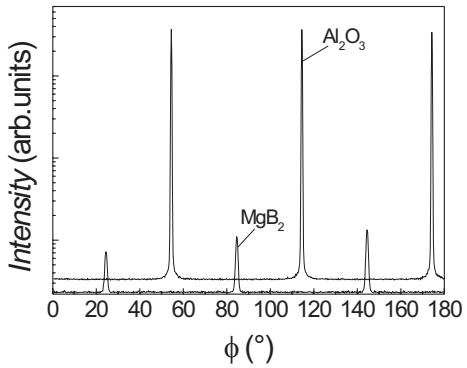

Fig 5.4 *ϕ-scan of three symmetry related reflections $(2,\bar{1},1)$ of the MgB_2 film and $(2,\bar{1},6)$ of the Al_2O_3 substrate. A 30° rotation of MgB_2 with respect to the a and b substrate axes is observed.*

The samples were further investigated by Scanning Electron Microscopy (SEM) and Atomic Force Microscopy (AFM). In Fig. 5.5 the SEM pictures of the typical morphologies of the samples prepared on SiC and Al_2O_3 are depicted. The samples are about 100 nm thick.

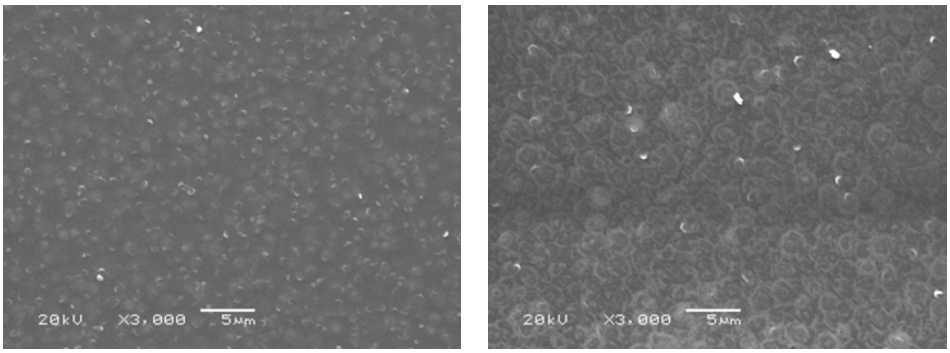

(a) *(b)*

Fig. 5.5 *SEM image of the samples made on (a) SiC and (b) Al_2O_3 substrates. Both of the samples were prepared with 150 sccm B_2H_6 flow.*

Hexagonal-shaped growth columns of different heights are observed, which is in accordance with results from [16], where presented AFM and SEM results show that the typical growth columns have dimensions ~ 100 nm. In Fig. 5.6 an AFM image of a typical morphology with hexagonal MgB_2 columns of the films deposited on SiC substrate is depicted.

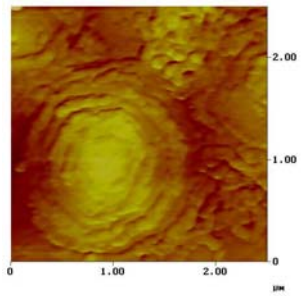

Fig. 5.6 *Typical AFM images of the samples deposited on SiC with B_2H_6 gas mixture flow rates of 100 sccm.*

Zeng et al. [16] observed by high-resolution transmission electron microscope (HRTEM) MgO regions in a thin layer near the MgB_2/Al_2O_3 interface, which can be the result of the reaction of the oxygen from the substrate with the film. In the case of SiC substrates no MgO regions are present. This is very well in agreement with the reactivity of MgB_2 with Al_2O_3 and SiC substrate presented in Table 4.6 (Section 4.4). The r.m.s. roughness depends on the substrates used. The r.m.s. roughness of the samples made on SiC is approximately 2.5 nm and for samples made on Al_2O_3 about 11 nm. The increased roughness of

the films deposited on Al_2O_3 can be attributed to the still significant lattice misfit even after the in-plane rotation of MgB_2 on this substrate as well as by the formation of MgO regions near the MgB_2/Al_2O_3 interface.

The MgB_2 grain sizes increase with higher B_2H_6 gas mixture flow rates from about 1.4 μm for the samples prepared with 50 sccm to about 2.2 μm for the samples made with 150 sccm B_2H_6 gas mixture flow. This increase is in agreement with the observation made by *Pogrebnyakov et al*. [24]. The boron supply increases by increasing the B_2H_6 gas mixture flow, which is reflected in the increase of the MgB_2 grain sizes.

The samples deposited on SiC showed a T_C of 41 K, which is ~ 1 K higher compared to the samples prepared on Al_2O_3 [24]. *Pogrebnyakov et al.* [24] observed that with increasing the film thickness from 42 to 300 nm the T_C increases from 40.3 to 41.8 K for the samples prepared on SiC, i.e., the increase of 3.7% is obtained. This trend is observed on both substrates, but the films on SiC have constantly a degree higher T_C than on Al_2O_3. The conclusion of their study on the correlation between strain, T_C and film thickness is that the T_C increases due to the tensile strain. *Ronser et al.* [26] have calculated the effect of the tensile strain, and found that a tensile strain causes an E_{2g} phonon softening, which leads to a stronger electron-phonon coupling and a higher T_C. The value from his calculation is consistent with results observed by *Xi et al*. [27]. According to the model of *Nix and Clemens* [28] when the crystallites meet during the film growth, the top of the crystallites snap together to reduce the surface energy, which produces a tensile strain in the film. The tensile strain increases with the film thickness until the film thickness reaches the order of the grain size and often it continues further until it finally relaxes. *Xi et al*. [27] observed by AFM the formation of hexagonally shaped growth columns that are not fully connected in the thinner films (thickness ~ 7.5 nm). They become fully coalesced when the film thickness becomes larger (~ 90 nm). The columnar growth and the coalescence could explain why the tensile strain increases with film thickness. It is reported in [24] that the *a* lattice parameter increases and the *c* lattice parameter decreases with the film thickness. This was reflected in the T_C values: T_C becomes higher when the *a* axis becomes longer, and at the same time the *c* axis becomes shorter. An increase of T_C by *c*-axis compression is predicted also by first-principle calculation in [29]. It can thus be concluded that the increase of T_C is due to the tensile strain.

5.2.3 Discussion

Superconducting MgB_2 thin films formed by the PLD and HPCVD methods, exhibit different structural properties.

Superconducting films prepared by PLD were deposited at low substrate temperatures, room temperature or 200°C, because it was not possible to create locally a very high Mg flux that would compensate for the Mg loss while depositing at higher temperatures. A high-temperature annealing step (~ 600°C) was needed to achieve the superconducting phase.

The two-step deposition resulted in films with reduced T_C's as compared to the bulk value. The absence of the MgB_2 peaks in the XRD measurements of the these samples, reduced T_C and TEM experiments of the similar samples from the literature [22,5] indicate that our films are polycrystalline with very small grain sizes (< 5 nm) of MgB_2 and a considerable presence of impurities (such as MgO). Since the films were not epitaxially grown, we did not observe a dependence on the type of the substrate used.

Epitaxially grown superconducting films were formed by the HPCVD method in an one-step deposition at high substrate temperatures (~ 700°C). In this method it was possible to form locally (close to the substrate) a very high Mg pressure by evaporation of solid Mg, possibly due to the very high ambient pressure (~ 100 Torr) as compared to the vacuum techniques.

The growth of these epitaxial films depends on the type of the substrates used. The films rotated for 30° with respect to the to the in-plane axes of Al_2O_3 (*c*-plane) to reduce the lattice misfit between the substrate and the film. The low misfit with SiC, on the other hand, allow the growth of MgB_2 without any rotation (Chapter 4, Table 4.5). The films were very smooth. The r.m.s. roughness ranges from ~ 2.5 nm for the samples prepared on SiC to ~ 11 nm for the samples made on Al_2O_3. The increased film roughness of the samples deposited on the Al_2O_3 substrates can be attributed to the about 20 times higher lattice misfit with this substrate as compared to SiC even after in-plane rotation of the films on Al_2O_3 substrates and the reaction with oxygen from the substrate, which forms MgO regions near the MgB_2/Al_2O_3 interface [16].

The films deposited on SiC had a T_C of about 41 K, whereas the films made on Al_2O_3 had a degree lower T_C. *Pogrebnyakov et al.* [24] observed that with increasing the film thickness the T_C increases. Their study on the correlation between the strain, T_C and film thickness concluded that the T_C increases due to the tensile strain in the film.

5.2.4 Outlook

In the HPCVD method a high Mg flux is achieved. This was needed to stabilize MgB_2 in the film as well as to overcome the low sticking coefficient of Mg at elevated temperatures. In the vacuum techniques independent control of the Mg and B fluxes is necessary to enable a high Mg flux. In experiments done

by *Ueda et al*. [14], where the superconducting MgB_2 films were grown by the MBE method, the high volatility of Mg limited the deposition temperature to about 320°C and required an extremely high Mg flux. In Ref. [30] it is reported that the desired phase is formed with Mg rates (fluxes) of about three times the nominal one. However, the higher Mg rates causes an excess of Mg in the film, which has harmful consequences on the superconducting properties either due to the proximity effect with normal Mg metal or the formation of nonstoichiometric $Mg_{1+x}B_2$.

In an alternative approach using vacuum deposition techniques towards the improvement of the MgB_2 thin film properties we propose a new concept for MgB_2 deposition (Fig. 5.7) [31], which combines two techniques: sputter deposition of boron and pulsed-laser deposition of magnesium. Using this approach the Mg/B flux ratio can be adjusted. The low heat conductivity of boron easily causes splashing during PLD of boron and, therefore, sputter deposition seems to be a better way of depositing this material.

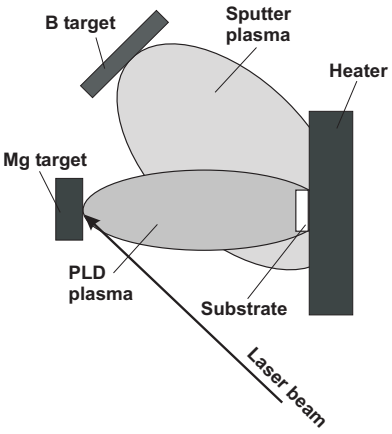

Fig. 5.7 *Schematic view of the combined PLD and sputter deposition technique.*

In this new concept, we are able to vary the Mg flux independently from the B flux by adjusting the laser frequency and the shape of the plasma. The high Mg flux is expected to allow higher deposition temperature, which is foreseen to lead to a better crystallinity of the films. The proposed approach is best combined with the earlier mentioned (in Chapter 4) high vacuum and gas mixture of Ar and H_2 (Ar + 4% H_2 (purity 99.9999%)).

Our attempts in achieving MgB_2 thin films by this method led to the following deposition parameters: The laser beam is focused on a 99.98% pure Mg target under an angle of 45°. The energy density on the target was 13 J/cm^2 to produce

a blue Mg plasma in 0.1 mbar of Ar + 4% H_2 mixture (purity 99.9999%) (Section 4.2). At the same time, a 99.9% pure boron target (2" in diameter) is sputtered at an RF power of 100 W. The sputter gun is fixed under an angle of 45° between the target normal and the substrate. In this configuration the Mg and B plasmas can collide, react and be deposited on the substrate.

The distance between the substrate and targets is optimized to position the substrate in the middle of both plasmas. As a result, the substrate was 7 cm far from the PLD target. The substrate temperature should be varied from 680°C to 700°C to try to achieve epitaxial growth of the films. The Mg and B fluxes have to be carefully tuned to ensure the reaction between them before Mg and B particles arrive at the substrate, to prevent Mg loss at such a high substrate temperature. Further experiments are needed to optimize the deposition parameters and achieve superconducting MgB_2 phase.

5.3. Superconducting properties of the films

5.3.1 PLD films

The films obtained by PLD from Mg-enriched MgB_2 targets and the mulilayers were superconducting with a critical temperature of up to 28 K (Fig. 5.1 and Fig. 5.8) and a superconducting transition of ΔT_C ~ 3 K.

The value of the residual resistance ratio RRR (R (300 K)/R (40 K)) for most of the samples was close to 1 (Fig. 5.8). From this value it is concluded that a lot of impurity scattering is present [32].

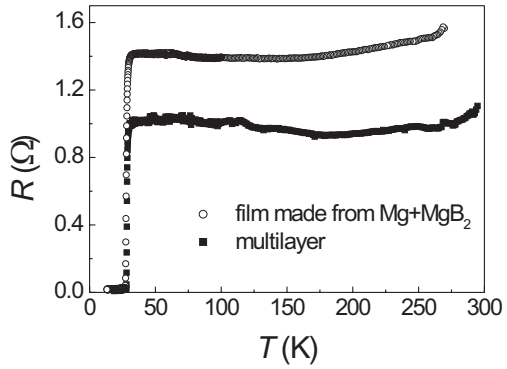

Fig. 5.8 *Resistance vs. temperature measurements of superconducting thin films made from Mg-enriched MgB_2 target ($T_{C,0}$ ~ 27 K) and multilayered film ($T_{C,0}$ ~ 28 K).*

As stated before, the films were polycrstalline, but the polycrystallinity does not hamper the supercurrent, since the grain boundaries in MgB_2 act as strong links [34,35]. This is also illustrated by the critical current density, which exceeds 10^6 A/cm^2 at 20 K in those films (presented in more detail in Chapter 6).

Fig. 5.9 presents the resistive transitions in applied magnetic fields of a sample fabricated in our experiments on a MgO substrate. The film of about 100 nm thickness was deposited for 3 min at 10 Hz laser frequency at 200°C and annealed 5 min at 600°C in a Mg plasma. The magnetic field was parallel (Fig. 5.9(a)) and perpendicular (Fig. 5.9(b)) to the substrate surface. The superconducting transition was rather sharp even in applied fields, which indicates a very strong flux pinning (see e.g., [35,36]). Upper critical fields (H_{C2}) as well as irreversibility fields (H_{irr}) were determined from Fig. 5.9. The upper critical field is defined as R (H_{C2}) = 0.9 R (T_C) (as in [37]) to make it less sensitive to noise on the upper parts of the curves, although this definition underestimates the actual upper value of the critical field. The irreversibility field has been defined as R (H_{irr}) = 0.1 R (T_C).

Fig. 5.10(a) shows the dependence of H_{C2} and H_{irr} versus T/T_C in two different field directions. The values of the irreversibility fields are quite close to the H_{C2} values due to the very sharp transition indicating a very strong flux pinning.

The difference of the H_{C2} values for parallel and perpendicular directions of the applied magnetic fields allowed the determination of the in-plane and out-of-plane coherence lengths. They are calculated from the Ginzburg-Landau equations close to T_C. The coherence length in the *a-b* directions is defined as:

$$-\frac{dH_{C2}^{\perp}}{dT} = -\frac{1}{T_C}\frac{\phi_0}{2\pi\xi_{ab}^2}, \tag{5.1}$$

where ϕ_0 is the flux quantum (= 2.07x10^{-15} Tm^2). In our case ξ_{ab} was substituted with ξ_{ab}^{eff} and has a value of 2.1 nm. The coherence length in the *c* direction is:

$$-\frac{dH_{C2}^{\parallel}}{dT} = -\frac{1}{T_C}\frac{\phi_0}{2\pi\xi_{ab}\xi_c}, \tag{5.2}$$

whereas in our case ξ_c was substituted with ξ_c^{eff} and found to be 0.9 nm. The substitution of the coherence lengths in two directions with their effective values is done because we could not determine the orientation of the MgB_2 grains from XRD as a consequence of their nanometer dimensions. Therefore, the measured values in two directions are associated to the substrate surface planes. The anisotropy of the coherence length presented as:

$$\gamma_\xi = \xi_{ab}/\xi_c \tag{5.3}$$

i.e. in our case $\xi_{ab}^{eff}/\xi_c^{eff}$ is found to be 2.3 close to T_C.

In Fig. 5.10(b) the anisotropy of the upper critical fields in two directions, defined as:

$$\gamma_{C2} = H_{C2}^{\parallel} / H_{C2}^{\perp} , \tag{5.4}$$

is illustrated. It has been calculated from the second order polynomial fits of the curves of H_{C2} in two directions of the applied magnetic fields. It decreases with an increase of the temperature from about 2.66 to 2.36 for the temperature range region close to critical temperature. The lower value of the anisotropy compared to the values obtained for single crystals [38-42] indicates that a significant misorientation of the grains in the film is present. However, the existence of the anisotropy shows that the grains are not completely randomly oriented.

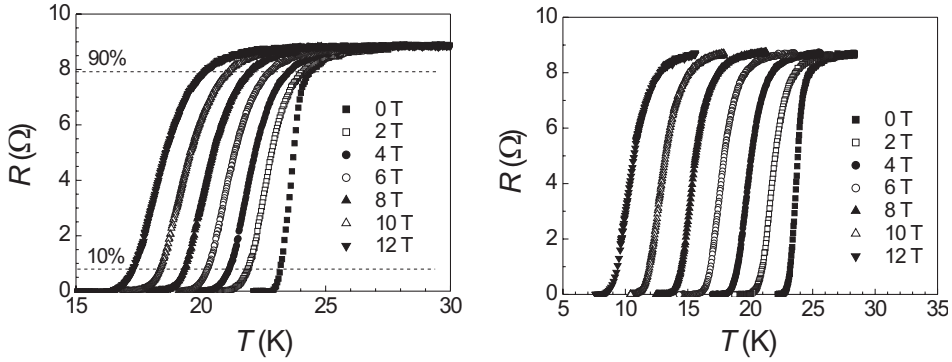

Fig. 5.9 *Resistive measurements in applied magnetic fields of MgB_2 film deposited from a Mg-enriched MgB_2 target on MgO substrate. (a) The field is parallel to the a-b substrate plane. The horizontal dashed lines correspond to 0.1 R (T_C) and 0.9 R (T_C) defining the irreversibility and the upper critical fields plotted in Fig 5.10(a); (b) The field is perpendicular to the a-b substrate plane.*

The electron mean-free path in the σ bands can be determined from H_{C2} measurements, since these measurements are probing the band with the stronger superconducting properties. The electron mean-free path (l) can be estimated from the equation:

$$\xi_{ab}(T) = 0.855(\xi_0 l)^{1/2} / (1 - T/T_C)^{1/2} . \tag{5.5}$$

We used the single crystal value of $\xi_{ab}(0) \approx 5$ nm for ξ_0 [42]. The coherence length at 0 K in the *a-b* plane was estimated from a linear fit of the H_{C2} in the magnetic field perpendicular to the *a-b* plane from Fig. 5.10(a) and from the Ginzburg-Landau relation to be 3.7 nm. This gives a value of about 3.7 nm for

the electron mean-free path. Since *l* is smaller than ξ_0 this film is considered to be in the dirty limit.

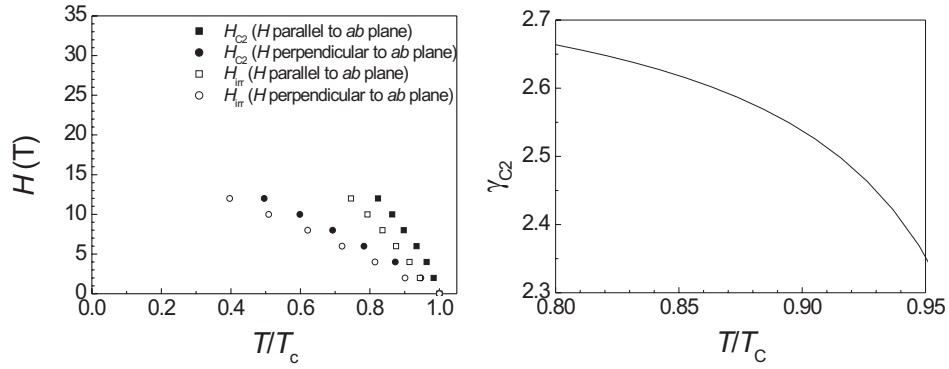

(a) *(b)*

Fig. 5.10 *(a) H_{C2} and H_{irr} of a sample in the fields in parallel and perpendicular directions to the a-b plane of the substrate; (b) Anisotropy of H_{C2} vs. T/T_C calculated from the fits of H_{C2} data.*

5.3.2 HPCVD films

The samples made by the HPCVD method had a very low resistance and a very sharp transition (ΔT_C ~ 0.1-0.3 K). The residual resistance ratio RRR (*R* (300 K)/*R* (40 K)) value was about 21 for the sample shown in Fig. 5.11. It was noticed that RRR ratios for HPCVD films range from 4 to 21 for different films. *Kim et al*. [43] suggest that according to their experiments and single-crystal studies [44], the RRR of stoichiometric MgB_2 should be ~ 5-7. They showed that the large RRR value of the inhomogeneous MgB_2 samples could be quantitatively explained by a two-phase model in which the two phases are Mg and MgB_2. Although we measured only resistance and not the resistivity it is anticipated that the top layer can contain more Mg due to the deposition procedure, i.e. it. This gives a large spread in the RRR values. As we will see later (in Chapter 7) it is not expected that Mg is incorporated in the grains, since large critical current values (~ mid-10^7 A/cm^2) are observed in nanobridges formed in the HPCVD films, despite a RRR value of 27 (Fig. 7.5, Section 7.3.2).

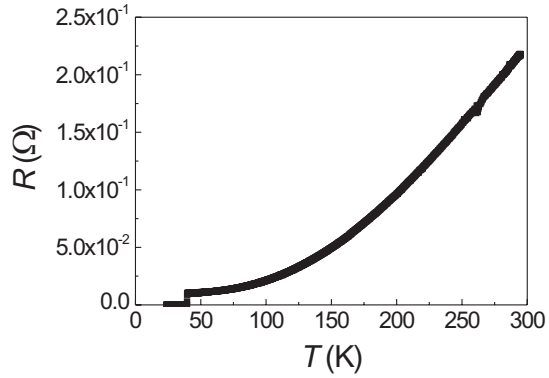

Fig. 5.11 *Resistance vs. temperature measurement of superconducting MgB_2 thin films deposited on Al_2O_3 prepared by the HPCVD method.*

In Fig. 5.12, resistive measurements in applied magnetic fields of an epitaxial MgB_2 film are depicted. The sample has been grown on an Al_2O_3 substrate with a 150 sccm B_2H_6 gas mixture flow rate. The sample was measured in fields parallel and perpendicular to the *a-b* plane of the films. The upper critical field is defined as R (H_{C2}) = 0.9 R (T_C) as in Section 5.3.1.

Fig. 5.13(a) presents the upper critical field as the function of T/T_C. A linear extrapolation of H_{C2} for the fields perpendicular to the *a-b* plane gives a value of 4 T at 0 K. The determination of $H_{C2}^{\parallel}(0)$ is more complicated. Since the measurements at higher fields were not possible, we can only make theoretical calculation for that range. We used the theoretical model [45] for the extrapolation of H_{C2} for the fields parallel to the *a-b* plane. The slope of the linear fit differs in the whole temperature range [45]. The theory predicts that there is a strong variation of the slope (positive curvature) near T_C, while at lower temperatures the slope is constant. Therefore, the range from 0.6 until 0.8 was chosen to fit it linearly. From this fit the $H_{C2}^{\parallel}(0)$ value of 25 T is estimated. For more precise determination of $H_{C2}^{\parallel}(0)$ and further analysis using the theoretical approach from [45], measurements in the higher magnetic fields are needed.

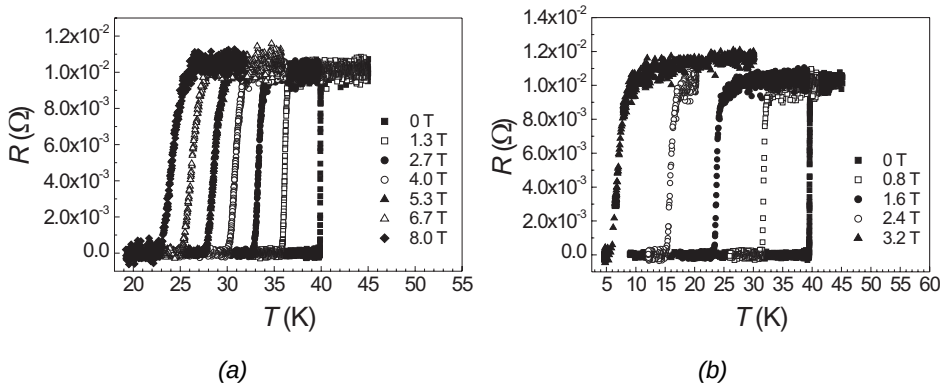

(a) *(b)*

Fig. 5.12 *Resistive measurements in applied magnetic fields of MgB_2 film deposited on Al_2O_3 substrate. (a) The field is parallel to the a-b film plane; (b) The field is perpendicular to the a-b film plane.*

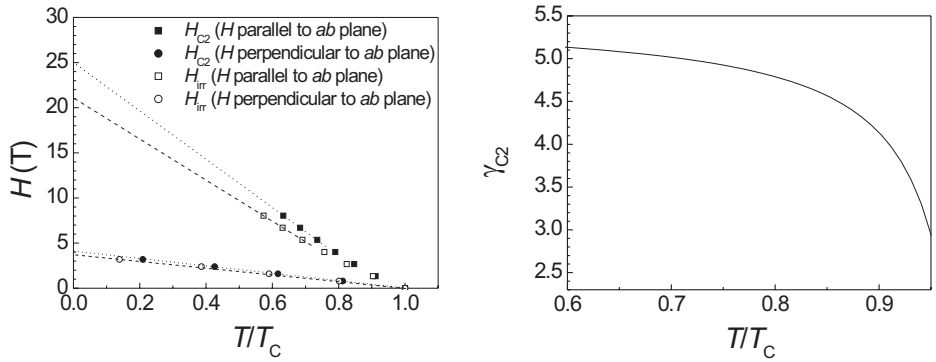

(a) *(b)*

Fig. 5.13 *(a) Linear fit of H_{C2} and H_{irr} of sample in the fields in parallel and perpendicular directions to the a-b plane; (b) Anisotropy of H_{C2} vs. T/T_C* calculated from the fits of H_{C2} *data.*

The irreversibility field H_{irr} together with H_{C2} for both directions of applied magnetic field is presented in Fig. 5.13(a). It has been defined as R (H_{irr}) = 0.1 R (T_C) as in Section 5.3.1. and H_{irr} (0) values are rather close to H_{C2} (0) indicating strong flux pinning. H_{irr} (0) in the field parallel to the *a-b* plane has a value of 21 T, whereas with applied fields perpendicular to the *a-b* plane is about 3.8 T.

In Fig. 5.13(b) the anisotropy of the upper critical fields in two directions is presented. It has been calculated from the linear fits of the H_{C2} in two directions of the applied magnetic fields (eq. (5.4)). It shows the usual temperature

dependence behavior as for single crystals [38-42], for which the anisotropy parameter increases from ≈ 3 at T_C up to 5-6 at 0 K.

The coherence lengths in the *a*-*b* and *c* planes are calculated from the Ginzburg-Landau equations close to T_C (given in Section 5.3.1, eq. (5.1)-(5.2)) and have values of 8.7 nm and 2.1 nm, respectively. The anisotropy of the coherence length defined as in equation (5.3) is found to be 4.1 close to T_C.

The electron mean-free path is estimated (in the same way as in Section 5.3.1, eq. (5.5)) to be about 17 nm, which is much larger compared to ξ_0 and therefore this film is in the clean limit.

5.3.3 Discussion

The electrical properties of the films made by the PLD and HPCVD method differ as a consequence of their different structural properties.

The films made by PLD had reduced T_C's compared to the epitaxial HPCVD films with the bulk-like T_C value. The presence of a considerable amount of impurities in the PLD films could also be the reason for the reduced RRR value as compared to the HPCVD films.

The electron-mean free path calculated from the resistive measurements in applied magnetic fields showed that the HPCVD films are in the clean limit, whereas the PLD films are in the dirty limit. This reveals that PLD films contain more impurities, which is also indicated by the reduced T_C.

The anisotropy of the coherence length present in the PLD films illustrates that grains are not randomly oriented in the film. The anisotropy of the HPCVD films has a similar value as anisotropy in the single crystal and a similar temperature behavior [38-42], which suggests that the grains in the films are well oriented in a preferred direction. XRD data shows that they are *c*-axis oriented. Two-band model [45-47] predicts a strong variation of the anisotropy with the temperature. This is observed in our samples too (for the PLD (Fig. 5.10(b)) and the HPCVD (Fig. 5.13(b)) samples). The irreversibility field values are close to the H_{C2} values for both films and in both directions indicating a strong flux pinning.

5.4 Conclusions

In this Chapter the preparation and properties of superconducting MgB_2 thin films made by the PLD and HPCVD methods are discussed. In has been shown that the complicating factors, such as high sensitivity of Mg and B to oxidation

and the high Mg vapor pressure, can be overcome to realize superconducting MgB_2 thin films.

Superconducting films have been achieved by two-step *in-situ* pulsed-laser deposition. The films were first formed at lower temperature (room-temperature or 200°C) followed by a high-temperature annealing step necessary to achieve a superconducting phase. The high Mg vapor pressure makes a one-step process at high temperature not possible, unless extremely high Mg flux can be applied during deposition, which was not achievable by this technique. The films were prepared from a Mg-enriched MgB_2 target (where additional Mg is used to compensate for loss of volatile Mg), as well as Mg and B multilayers. The films had transition temperatures of maximally 28 K.

The influence of the substrate temperature, annealing procedure and purity of the starting materials are found to be significant in obtaining the superconducting films. The films deposited at 200°C had the highest T_C, while deposition at 300°C already resulted in non-superconducting films, possibly due to lack of Mg present in the film caused by the low sticking coefficient of Mg at elevated temperature. The annealing procedure was found to influence the value of T_C. Additional annealing of the sample at 500°C for 1 h leads to better results than just quenching from 600°C. These MgB_2 films are polycrystalline with grain sizes smaller than 5 nm, since no XRD peaks could be observed. The multilayered films using Mg and B targets showed an increased T_C compared to the ones made from Mg-enriched MgB_2 target, which can be attributed to the higher purity of the targets.

The reduced transition temperature as compared to the bulk value (39 K) is possibly due to the small MgB_2 grain-size, impurities present in the starting material and MgO inclusions formed in the films.

Another approach in the growth of superconducting MgB_2 films is the use of the Hybrid Physical-Chemical Deposition (HPCVD) technique [16,17]. A very high Mg flux and its reaction with a B_2H_6 gas mixture allow the deposition at elevated temperatures (720-760°C) in one step of very smooth, epitaxial MgB_2 thin films. They showed a bulk-like value of the critical temperature. X-ray diffraction showed that the films are single-crystal-like with *c*-axis perpendicular to the substrate surface. The films deposited on Al_2O_3 (c-plane) were rotated by 30° with respect to the *a*-*b* axis of the substrate to reduce the lattice misfit between the substrate and the film, whereas no rotation on SiC is observed due to the very small lattice misfit.

The experiments done on determination of the upper critical fields (H_{C2}) on the samples prepared by the PLD and HPCVD methods showed that the value of the irreversibility field is rather close to the value of the upper critical fields in both samples indicating strong flux pinning. The anisotropy of the upper critical fields had similar temperature dependence, but in the case of the HPCVD films

the anisotropy is more pronounced and almost reaches the value determined for single crystals. This indicates that HPCVD films are very well oriented. The coherence lengths in both samples differ for in-plane (*a*-*b*) and out-of-plane (*c*) directions as a consequence of strong anisotropy of the σ band. The estimated values of the electron mean-free path in both samples showed that the sample prepared by the PLD technique is in the dirty limit. This is in agreement with the reduced critical temperature of the PLD samples. On the other hand, the sample prepared by the HPCVD method is in the clean limit.

The films made by both techniques can be used for fundamental studies of the superconducting properties of MgB_2. The HPCVD films are more suitable for the devices fabrication due to their high smoothness and good superconducting properties.

References:

[1] A. Brinkman *et al*., Supercond. Sci. Technol. **16**, 246 (2003).
[2] W. N. Kang, H. J. Kim, E. M. Choi, C. U. Jung and S. I. Lee, Science **292**, 1521 (2001).
[3] S. D. Bu *et al.,* Appl. Phys. Lett. **81**, 1851 (2002).
[4] N. Hur *et al.,* Appl. Phys. Lett*.* **79**, 4180 (2001).
[5] C. B. Eom *et al*., Nature **411**, 558 (2001).
[6] A. Brinkman *et al.*, Physica C **353**, 1 (2001).
[7] D. H. A. Blank *et al*., Appl. Phys. Lett*.* **79**, 394 (2001).
[8] S. R. Shinde *et al*., Appl. Phys. Lett. **79**, 227 (2001).
[9] H. M. Christen *et al*., Physica C **353**, 157 (2001).
[10] S. N. Ermolov *et al*., JETP Lett*.* **73**, 557 (2001).
[11] D. Mijatovic *et al.*, Physica C **372-6**, 1258 (2002).
[12] Mi. Jergel *et al*., Physica C **383**, 287 (2003).
[13] A. Saito, A. Kwakami, H. Shimakage and Z. Wang, Jpn. J. Appl. Phys. **41,** L127 (2002).
[14] K. Ueda and M. Naito, Appl. Phys. Lett. **79**, 2046 (2001).
[15] W. Jo *et al.,* Appl. Phys. Lett. **80,** 3563 (2002).
[16] X. H. Zeng *et al*., Nature Materials **1**, 1 (2002).
[17] J. Rowell, Nature Materials **1**, 6 (2002).
[18] W. N. Kang, E. M. Choi, H. J. Kim, H. J. Kim and S. I. Lee, cond-mat/ 0209226 (2002).
[19] X. X. Xi *et al.,* J. Supercond.: Incorp. Novel Magn. **16**, 801 (2003).
[20] Z. K. Liu, D. G. Schlom, Q. Li, X. X. Xi, Appl. Phys. Lett. **78**, 3678 (2001).
[21] Z. Y. Fan, D. G. Hinks, N. Newman and J. M. Rowell, Appl. Phys. Lett. **79**, 87 (2001).
[22] X. X. Xi *et al.,* Supercond. Sci. Technol. **15**, 451 (2002).
[23] X. X. Xi *et al.,* Supercond. Sci. Technol. **13**, 3233 (2003).
[24] A. V. Pogrebnyakov *et al*., Appl. Phys. Lett. **82**, 4319 (2003).
[25] W. Tian *et al*., Appl. Phys. Lett. **81**, 685 (2002).
[26] H. Rosner, J. M. An, W. E. Pickett and S. L. Drechsler, Phys. Rev. B **66**, 024521 (2002).
[27] X. X. Xi, *Progress in the Deposition of MgB_2 Thin Films*, oral presentation at EUCAS conference (2003).
[28] W. D. Nix and B. M. Clemens, J. Mat. Res. **14**, 3467 (1999).
[29] T. Yildirim and O. Guelseren, J. Phys. Chem. Solids **63**, 2201 (2003).
[30] K. Ueda, and M. Naito, J. Appl. Phys*.* **93**, 2113 (2003).
[31] D. Mijatovic *et al*., IEEE Trans. on Appl. Supercond. **13**, 3245 (2003).
[32] A. Brinkman, *Charge transport in double-barrier and magnesiumdiboride*

Josephson junctions, PhD. Thesis, University of Twente, Enschede, The Netherlands.
[33] D.C. Larbalestier *et al*., Nature **410**, 186 (2001).
[34] D. K. Finnemore, J. E. Ostenson, S. L. Bud'ko, G. Lapertot, and P. C. Canfield, Phys. Rev. Lett. **86**, 2420 (2001).
[35] J. Evetts, *Concise Encyclopedia of Magnetic and Superconducting Materials*, Pergamon Press, 1st ed., (1992).
[36] E. H. Brandt, Reports in Physics **58**, 1465 (1995).
[37] A. Gurevich *et al*., Supercond. Sci. and Techol. **17**, 278 (2004).
[38] M. Angst *et al*., Phys. Rev. Lett. **88**, 167004, (2002).
[39] G. K. Perkins *et al*., Supercond. Sci. Technol. **15**, 1156 (2002).
[40] A. V. Sologubenko *et al*., Phys. Rev. B **65**, 180505 (2002).
[41] M. Zehetmayer *et al*., Phys. Rev B **66**, 052505 (2002).
[42] P. C. Canfield *et al.,* Physica C **385**, 1 (2003).
[43] K. H. Kim *et al*., Phys. Rev. B **66**, 020506(R) (2002).
[44] M. Xu *et al*., Appl. Phys. Lett. **79**, 2779 (2001); K. H. P Kim *et al*., Phys. Rev. B **65**, 100510 (2002); S. Lee *et al*., J. Phys. Soc. Jpn. **70**, 2255 (2001).
[45] A. A. Golubov and A. E. Koshelev, Phys. Rev. B **68**, 104503 (2003).
[46] P. Miranović, K. Machida and V.G. Kogan, J. Phys. Soc. Jpn. **72**, 221 (2003).
[47] T. Dahm and N. Schopohl, Phys. Rev. Lett. **91**, 017001 (2003).

Weak links in MgB_2 thin films

6

Abstract

Weak links in MgB_2 thin films, such as Josephson junctions and nanobridges, have been realized as a significant step towards application of MgB_2 in electronic devices.

Using the ramp-type Josephson junction configuration two superconducting MgB_2 layers made by the PLD method were separated by a thin MgO barrier layer. Their current-voltage characteristics follow the behavior described by the resistively shunted junction model, albeit with an excess current of about 30% of the critical current I_C. A suppression of 70% of I_C was achieved in applied magnetic fields. Shapiro steps were observed when irradiating the junctions with 10.0 GHz microwaves and the dependence of the step height on applied rf current is well described by a current-source model. Reference samples prepared without the MgO layer showed strong-link behavior with large I_C values.

Nanobridges of widths down to 100 nm were formed in epitaxial MgB_2 thin films prepared by the HPCVD method. They had very high critical current densities of about $5x10^7$ A/cm^2 at 4.2 K.

6.1 Introduction

The exploration of suitable weak link configurations in MgB_2 thin films is an important aspect towards the realization of electronic devices. This Chapter focuses on two types of weak links: ramp-type Josephson junctions and nanobridges formed in MgB_2 thin films. The fabrication and properties of these weak links are presented here. Less anisotropy, fewer material complexities, strong links between grain boundaries [1,2] and a longer coherence length ($\xi \sim 5$ nm) compared to high-temperature superconductors (HTS) make MgB_2 feasible to realize good Josephson junctions.

Besides the larger critical temperature of MgB_2 as compared to the low-T_C materials, a further positive aspect is the larger charge carrier density of MgB_2 as compared to the high-T_C materials, which is deemed to be beneficial, e.g., for the noise properties of Josephson devices. Furthermore, taking into account the multiband nature of superconductivity, which has as a consequence the existence of two different gaps in MgB_2, large I_CR_N products are feasible, as was recently pointed out by *Brinkman et al*. [3]. For tunneling in the direction of the *a*-*b* plane of MgB_2 an I_CR_N product of 5.9 mV at T = 4.2 K is predicted and 4.0 mV for tunneling in the *c*-axis direction.

Films prepared by PLD (as described in Chapter 5) were used for the realization of ramp-type Josephson junctions. Our first realizations of such types of MgB_2 Josephson junctions showed a modulation of the critical current of the junctions in a magnetic field and the appearance of Shapiro steps by applying microwave irradiation, as will be described in detail below.

Fabrication of nanobridges is an alternative method for the formation of weak links. Nanobridges were formed in epitaxial thin films grown by the HPCVD method (in more details given in Chapter 5). The high quality films had a very high critical current density of about 5×10^7 A/cm^2 at 4.2 K.

The weak links can be further incorporated in a superconducting loop forming SQUIDs as will be presented in the next Chapter.

6.2 Ramp-type Josephson junctions based on PLD thin films

A Josephson junction consists of two electrodes separated by a barrier layer, which can be an insulator or a normal metal. Ramp-type junctions [4] have been developed for high-T_C superconductors to obtain electrical transport through the barrier of the junction in the direction of the *a*-*b* plane of the crystal lattice in thin films grown with the *c*-axis perpendicular to the substrate surface.

Advantages of using this configuration for MgB_2 Josephson junctions are that possible degradation of superconducting properties at the surface of MgB_2 will not be reflected in the junction and that the junction area can be made small [5]. Degradation of the superconducting properties at the surface can occur due to several reasons such as an Mg deficiency in the top part of the film or the presence of a Mg capping layer depending on the thin film growth procedure. Since one of the dimensions of the junction is determined by the film thickness, the width of the junction can be varied to result in small junction areas.

6.2.1 Fabrication

To fabricate a Josephson junction in a ramp-type configuration, first a superconducting film is deposited on a substrate and structured by photolithography and Ar ion milling. Then, a ramp is etched in this film and finally the barrier (an insulator or a normal metal) and a top electrode of a superconducting film is deposited on top of it and patterned again by photolithography and ion milling to its final design (see Fig. 6.1(a)).

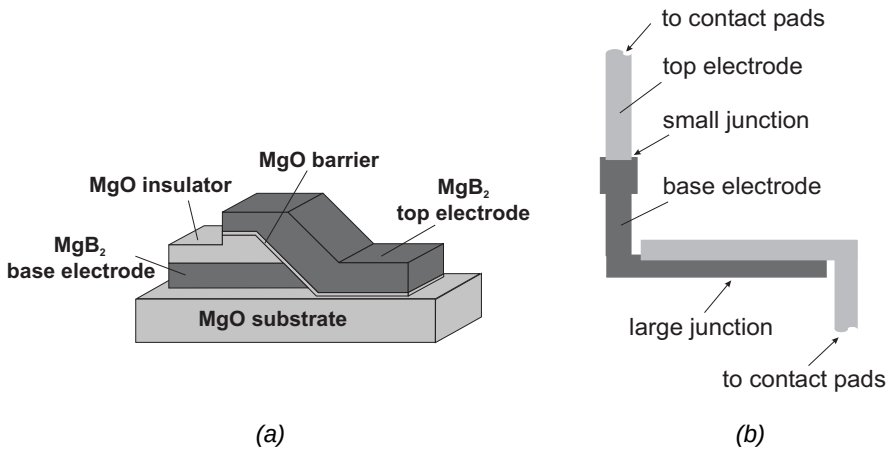

Fig. 6.1 *(a) Schematic presentation of a MgB_2 ramp-type Josephson junction with a MgO barrier layer; (b) Schematic presentation of the top view of the ramp-type junctions.*

A typical fabrication process for MgB_2 ramp-type junctions was as follows [6]: the first step was deposition of a bilayer of MgB_2 (200 nm) and MgO (100 nm) *in-situ* by PLD on a MgO substrate. The MgB_2 film was prepared from an Mg-enriched MgB_2 target in the way described in Chapter 5 (Section 5.2.1). In short, deposition took place at 200°C in 0.17 mbar Ar pressure for 6 min at 10

Hz, using a 4 J/cm^2 energy density of laser at the target. Subsequently, the MgB_2 layer was annealed at 600°C for 5 min in a Mg plasma, generated by ablation from a Mg target in 0.22 mbar Ar. After cooling down to 200°C, the MgO insulation layer was formed by ablating from an Mg target in an oxygen pressure of 0.5 mbar for 50 s at 10 Hz, using an energy density of 4 J/cm^2. Afterwards, the film was cooled down to room temperature keeping the pressure in the chamber unchanged.

Then, a beveled edge (ramp) was defined by photolithography and argon ion beam milling, under an angle of 45°. With a beam-voltage of 500 V the etching rate of the bilayer is about 8 nm/min. Due to the difference in etching rate between the photoresist and the MgO-MgB_2 bilayer, a slope of the ramp of about 20° is obtained, as determined by AFM.

After removing the photoresist, a 12 nm MgO barrier-layer was deposited by ablating Mg for 6 seconds at 10 Hz with an energy density of 4 J/cm^2, in 0.5 mbar O_2 at 200°C. Subsequently, a 200 nm MgB_2 counter-electrode was deposited in the same way as the base electrode. The sample was then patterned by photolithography and ion milling to define the junctions with an overlap of the counter electrode of 3 μm. Fig. 6.1(a) presents a schematic drawing of the junction configuration. The first MgO layer (100 nm) was used to assure that no contact between top and base electrode was made and that all electronic transport is established only through the junction. To contact the base electrode with the contact pads a ramp-type junction with a much larger area than the previously described junction was fabricated on the other side of the base electrode (Fig. 6.1(b)). The large junction area on this side allows a very high critical current to pass through this junction as compared to I_C that passes through the smaller junction and in this way it assures that the measured *I-V* characteristic belongs only to the small ramp-type junction.

6.2.2 Electrical characteristics

The electrical transport properties of the junctions were measured in a four-point configuration in a shielded cryostat. The transition temperatures of both electrodes were typically 23 K. This reduced critical temperature as compared to the bulk value is attributed to the small MgB_2 grain size and to impurities of the starting material as well as in the film (as discussed in Chapter 5). The amount of impurities in the electrodes could be increased compared to the as-grown films described in Chapter 5 (Section 5.2) due to the oxygen needed for fabrication of the barrier layer.

Resistively Shunted Junction (RSJ)-like current-voltage characteristics were obtained up to 16 K, albeit with an excess current. Above this temperature, the

supercurrent was suppressed by the thermal noise. Figure 6.2 displays the *I-V* characteristic of a 7 μm wide junction at T = 3.6 K, exhibiting an excess current of 30%.

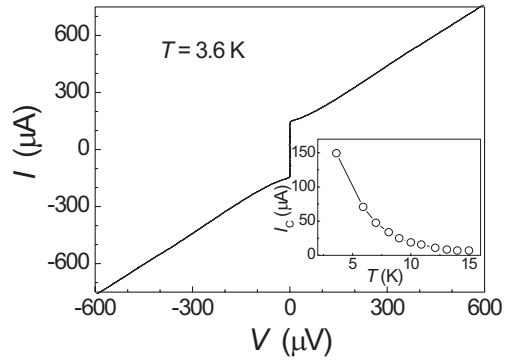

Fig. 6.2 *I-V characteristics of a 7 μm wide junction at T = 3.6 K. The inset shows the critical current vs. temperature dependence.*

At 4.2 K the I_C-value is 130 μA (using a voltage criterion of 5 μV) and taking the slope of 20° of the junction into account for the determination of the junction area, a corresponding critical current density in order of 1 kA/cm^2 was estimated. The normal state resistance R_N is almost temperature-independent and has a value of about 1 Ω. The I_CR_N product is thus 130 μV at T = 4.2 K. In the inset of Fig. 6.2 the dependence of the critical current on temperature is presented.

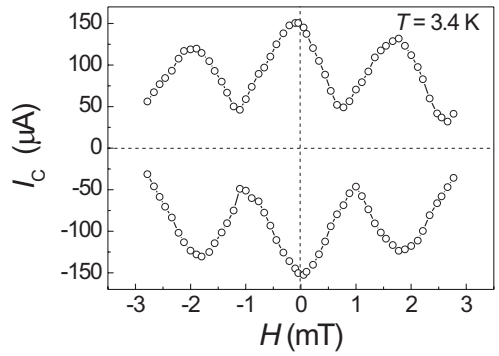

Fig. 6.3 *Modulation of the critical current by a magnetic field applied perpendicular to the current direction and parallel to the substrate, measured at T = 3.4 K.*

The influence of the thermal noise is expressed by the noise parameter Γ defined as $\Gamma = 2\pi k_B T/I_C\phi_0$, where k_BT is thermal energy, k_B is the Boltzmann

constant (k_B = 1.38x10^{-23} J/K) and $I_C\phi_0/2\pi$ is Josephson coupling energy. It is in the order of 10^{-3} at 4.2 K and in order of 10^{-1} at 16 K for those junctions.

The Josephson penetration depth is defined as $\lambda_J = \sqrt{\hbar/2e\mu_0 dJ_C}$ [7], where *d* is the barrier thickness plus twice the London penetration depth. For the junction described above λ_J is in the order of 10 μm. Since the width of the junction is smaller than $4\lambda_J$, the junction is in the small junction limit, which implies that a non-uniform current distribution due to self-field effects is not expected [8].

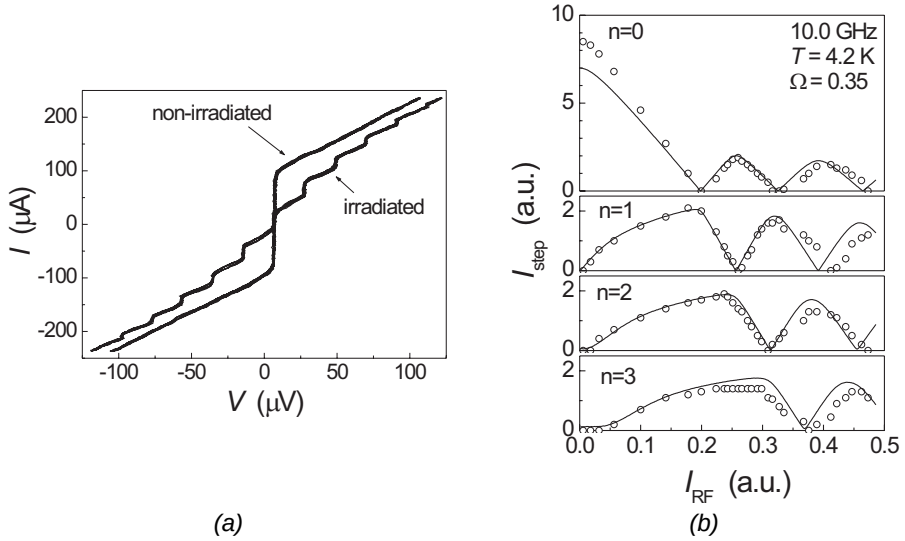

Fig. 6.4 *(a) Current-voltage characteristics of a 7 μm wide junction with and without 10.0 GHz microwave irradiation at T = 4.2 K; (b) The amplitude of the supercurrent and the first three Shapiro steps versus applied microwave irradiation (10.0 GHz) at T = 4.2 K. The solid line shows a fit using the current-source model.*

The application of a magnetic field *H* perpendicular to the current direction and parallel to the substrate resulted in a modulation of the critical current (Fig. 6.3) [6]. A suppression of the critical current by up to 70% was observed. The I_C(H)-dependence differs from the Fraunhofer dependence that is expected for a small junction with a uniform current distribution, with the large amplitude of the side-peaks and the incomplete suppression of the critical current being signatures of a non-homogeneity of the barrier. This non-homogeneity originates most likely from the roughness of the ramp area after the etching of the ramp, which will show an imprint in the surface roughness of the deposited film.

A complete suppression of the supercurrent and the formation of Shapiro steps at multiples of V = 20.7 μV were observed by irradiating the junction with 10.0 GHz microwave fields at T = 4.2 K (Fig. 6.4(a)) [6]. The voltages at which the current steps appear are as expected from the frequency of the applied radiation ν_f: $V_n = (h/2e)\nu_f n$, with $2e/h$ = 483.6 MHz/μV. The modulation of the height of the Shapiro steps as a function of applied RF current is presented in Figure 6.4(b). To describe the junction under microwave irradiation, the RSJ-model is extended with an RF current-source term with a large source-impedance [8]. It is assumed that the RF source impedance is large as compared to the junction impedance. With this current-source model a good fit to the experimental data was obtained. It is noted that the fitting parameters were the same for all the Shapiro steps Ω = 0.35. The fitting parameter Ω represents the normalized frequency f_{RF}/f_c, where $f_c=(2e/h)I_CR_N$ [5]. The critical current value I_C = 100 μA and the normal resistance value R_N = 0.8 Ω for this junction, as determined from the I-V curves (Fig. 6.4(a)), giving an I_CR_N product of 80 μV. This corresponds reasonably well with the I_CR_N product of 60 μV that can be derived from the Ω = 0.35 fit to the high frequency properties. The good fit to the Shapiro step heights shows that the current source model very well describes the microwave properties of the MgB_2 ramp-type junctions [5].

To determine the effects of the interfaces between the MgO-barrier and the electrodes on the junction transport properties, reference samples were prepared following the same fabrication procedure, except for the deposition of the barrier-layer. It has been shown, e.g., in high-T_C Josephson junction technology [9], that a barrier is formed at the interface between the electrodes, due to structural damage invoked by the ion-milling. In contrast, for our MgB_2 ramp-type contacts this ion-milling procedure did not lead to weak link behavior. Critical currents up to 31 mA were obtained for 5 μm wide contacts at T = 4.2 K, which corresponds to a critical current density of $3x10^6$ A/cm^2. This is comparable to J_C values of nanobridges made in a single film (presented in Chapter 7, Section 7.2.2). This implies that the interface region has good superconducting properties and will not affect the transport characteristics of the Josephson junctions. Furthermore, it indicates that the ramp-type contact presents a useful configuration for via-contacts in future multilayer circuits.

From the values described above, it is concluded that the 12 nm MgO barrier forms the weak link in our Josephson junctions. It is not a pure tunnel barrier, since a 12 nm thick true tunnel barrier would have resulted in a much smaller I_C and a normal state resistance that is much larger than the observed 1 Ω. The theoretically attainable I_CR_N product of MgB_2 tunnel junctions was in more detail investigated by *Brinkman et al.* [3]. The observed values lie well below the theoretical expectation, even taking into account the reduction of I_CR_N due to the reduced T_C. The presence of shunting channels (i.e., non-tunneling channels) in

the barriers that causes a decrease of R_N can explain the reduction of $I_C R_N$. The presence of shunting channels is furthermore consistent with the observation of excess current in the *I-V* curves. The non-ideal critical current modulation by magnetic field is a further indication for the resulting non-uniform current distribution over the junction. Taking into account that these junctions were made in the films on their early stage of development, they have already shown dc and ac Josephson effect by the modulation of the Josephson current of applied magnetic fields as well as the appearance of Shapiro steps under applied microwave irradiation.

From the junction geometry a capacitance C = 30 fF is estimated. This value together with a low value for R_N of about 1 Ω, explains the non-hysteretic character of the *I-V* curves. The estimated value for the Stewart-McCumber parameter β_C in the order of 0.01 corresponds as well to the absence of hysteresis.

Although *in-situ* grown MgB_2 thin films are smoother compared to *ex-situ* ones and hence more suitable for Josephson junction fabrication, the surface roughness of the PLD films still considerably influences the quality of the barrier. Improving the smoothness of the base electrode will enhance the barrier quality, and subsequently enhance the uniformity of the current through the junction and improve the reproducibility of the junction parameters. The shunting channels present in the MgO barrier, caused by the roughness of the film surface and the etching process, reduce the $I_C R_N$-product as compared to the theoretical prediction. A smoother base electrode would reduce inhomogeneities and shunting channels in the barrier and be beneficial in the realization of high-quality insulating barriers.

Additionally, epitaxial or at least *c*-axis oriented films are preferred, as this enables the fabrication of Josephson junctions in the *a-b* directions, which is expected to result in the highest $I_C R_N$-product. To achieve an epitaxial growth of the top electrode, the barrier material should fulfill the following requirements: lattice misfit between MgB_2 and the barrier material should be as low as possible, the barrier material should be grown epitaxially on the base electrode at temperatures lower than the degradation temperature of MgB_2 and the barrier material should be compatible with a high deposition and/or annealing step in the deposition of the top electrode.

6.3 Nanobridges made in HPCVD films

6.3.1 Nanobridges as weak links

Apart from barrier-layer type Josephson junctions, nanobridges can be utilized as weak links, which can be used to form a SQUID [7]. A number of papers on low-T_C superconductor SQUIDs based on nanobridges were published (e.g. [10-12]) and the first reports of SQUIDs based on nanobridges in high-T_C superconductors appeared in [13-15].

In Fig. 6.5 the forces acting on the vortices in a nanobridge are schematically presented. A transport-current that passes through the bridge induces a magnetic field, which can penetrate the superconductor in the form of Abrikosov vortices if the field is larger than the lower critical field H_{C1}. Two of such vortices, with opposite orientation, will then be created simultaneously at the edges of the bridge [16]. An edge-pinning force F_{pin} will act on the vortices. By increasing the transport current the Lorentz force F_L acting on the vortex will overcome this pinning. Consequently, for bias currents exceeding the critical current, the vortices will move towards each other and finally annihilate. During the vortex motion an electric field is induced in the direction of the transport current and energy dissipation will take place.

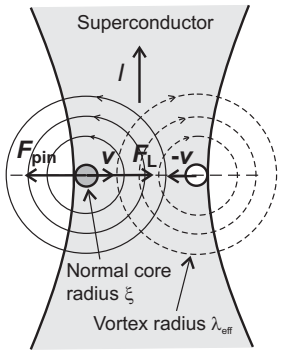

Fig. 6.5 *Schematic drawing of the forces acting on two Abrikosov vortices in a nanobridge (from [5]).*

The Abrikosov vortices have a normal core of the size of the coherence length radius (ξ). *Eskildsen et al.* [17] measured on MgB_2 single crystals from the vortex core the value of the coherence length in the *a*-*b* plane for the π band and found this to be about 50 nm. They estimated from the BCS expression the coherence length in the same plane for the σ band to be 13 nm, which is well in

agreement with the coherence length obtained from H_{C2} measurements (see for review [18]). On the other hand, the most common number for ξ used in calculations is about 5 nm, as reported in [19]. The normal core area in the bridge will act as a Josephson weak link for superconducting bridges that are smaller than a few times ξ. In this case a specific relationship exists between the supercurrent and the phase change of the macroscopic wave function over the weak link [20]. Wider bridges can show a significant current-phase relationship as well, provided the width of the bridge is comparable to, or smaller than, the effective London penetration depth $\lambda_\perp$ [21]. The most used values for the bulk penetration depth for MgB_2 vary from 140 to 180 nm ([19] and for review Ref. [22]), yielding an effective penetration depth, $\lambda_\perp = \lambda_L \coth(d/2\lambda_L)$ of 230 to 360 nm for films with a thickness d of 200 nm. This current-phase relationship was exploited to fabricate the first MgB_2 SQUIDs ([23] and Chapter 7).

6.3.2 Fabrication

To investigate the properties of the MgB_2 nanobridges, the nanobridges were formed in films prepared by the HPCVD method (as described in Section 5.2.2). Prior to these experiments, nanobridges incorporated in SQUIDs were made on the PLD film, as it will be in more details presented in the next Chapter.

Films with a thickness of about 100 nm were deposited on SiC substrates with a 100 sccm B_2H_6 gas mixture flow rate. They were rather smooth with a typical r.m.s. roughness of 4 nm as measured by AFM. Prior to the film structuring a 25 nm gold layer was deposited by RF sputter deposition to protect the film from degradation of the superconducting properties caused by the sensitivity of MgB_2 to water [24].

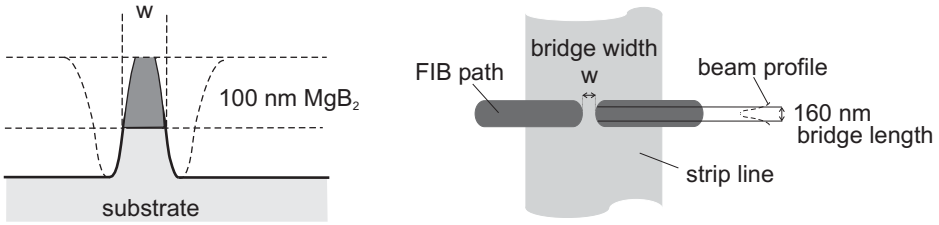

(a) *(b)*

Fig. 6.6 *(a) Schematic cross-section of the nanobridges made by FIB. (b) Top view of the strip line with a FIB path and the nanobridge.*

First, the coarse structures of the nanobridges together with the contact leads were defined by standard photolithography and argon ion-beam milling. The ion milling under an angle of 45° occurs at an etching rate of approximately 5 Å/s with an acceleration voltage of 500 V. Subsequently, nanobridges were structured into a stripline, 50 μm long and 5 μm wide, by direct Focused Ion Beam (FIB) milling. Using a 25 kV Ga^+ beam with a diameter of 50 nm (Full Width at Half Maximum) and a beam current of 40 pA, trenches are etched in the MgB_2 films at a rate of 0.30 mm^3/C. The density of the Ga^+ ions has a Gaussian distribution in the central part of the beam. The dimensions of the fabricated nanobridges are shown in Fig. 6.6. The width (w) defined as Full Width at Half Maximum (FWHM) was variable, the height of the nanobridges is approximately 100 nm and the length is about 160 nm. The dimensions of the bridge are determined from the known beam profile and analysis of Scanning Electron Microscopy images.

6.3.3 Electrical characteristics

The electrical characteristics of the nanobridges were measured in a four-point configuration in a shielded cryostat, like the properties of Josephson junctions described in Section 6.2.2. The films with nanobridges showed unchanged values of T_C (~ 40 K) as compared to the films before structuring.

The typical current-voltage characteristics above 10 K resemble the *I-V* characteristics presented in Fig. 6.7(a). In this Figure the non-hysteretic current-voltage characteristics of a 140 nm wide nanobridge at 22 K is shown. Below 10 K a small hysteresis appears in some cases, which can differ from bridge to bridge. The nanobridges showed a very high critical current density of $5x10^7$ A/cm^2 at 4.2 K. This value of critical current density is comparable to the highest one reported in bulk material [18].

To investigate how critical current density changes with small variations in the nanobridges width, we compared J_C of 100 nm and 140 nm wide nanobridges. The dependence of the critical current vs. temperature for two different nanobridges is illustrated in Fig. 6.7(b). Using SRIM (Stopping and Range of Ions in Matter) software, version SRIM-2000.40 [25,26], which can calculate the penetration depth of ions in MgB_2 films, we obtained the value of about 20 nm. This is consistent with the data presented in Fig. 6.7(b) and can explain a small difference in J_C value for both nanobridges in a way that the effective area, through which the current is passing, is smaller than the one estimated from FIB profile due to the damages caused by Ga ions. However, from the considerable spread in the J_C data for other nanobridges of the same

widths one may rule out that the fit of this 20 nm Ga ion damages into the effective area could be coincidental.

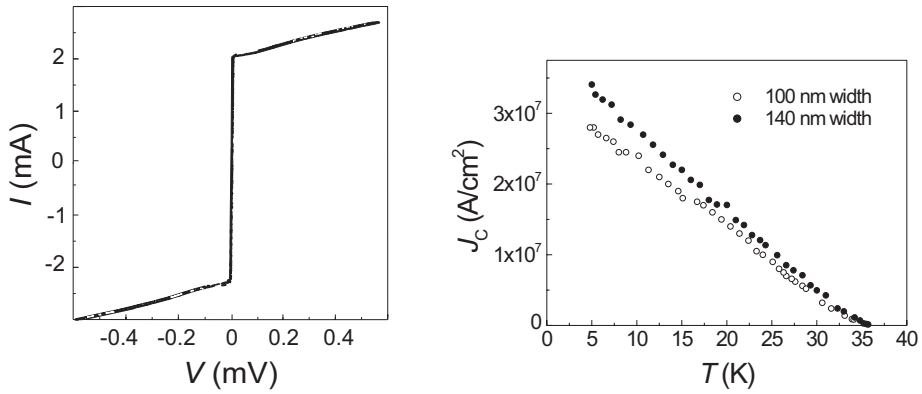

Fig. 6.7 *(a) Current-voltage characteristics of a 140 nm wide nanobridge at T = 22 K; (b) Critical current vs. temperature for nanobridges of 100 nm and 140 nm width.*

The depairing current density can be estimated for the single band case by $J_0 = 4B_C / \left[3\sqrt{6}\mu_0\lambda\right]$, where B_C is a thermodynamic critical field defined as $B_C = \phi_0 / 2\sqrt{2\pi}\lambda\xi$, ϕ_0 = *h/2e* is the flux quantum, λ is the penetration depth and ξ is the coherence length [27]. For MgB_2, by taking λ_{ab} (0) ~ 62 nm (as calculated in Chapter 7, Section 7.4.2) and $\xi_{ab}(0)$ ~ 5 nm [18], J_0 can be estimated to be ~ $2x10^9$ A/cm^2. The highest J_C's of the HPCVD films are in the order of 10^7 A/cm^2 (as shown in Fig. 6.7(b)). The J_C value in nanobridges is limited by the flux flow motion and not by the depairing mechanism, which explains the lower J_C value than the depairing current density.

6.4 Conclusions and outlook

The fabrication of MgB_2 weak links in the form of Josephson junctions and nanobridges presents an important step for further implementation of MgB_2 into electronics and superconducting sensors.

Our work on ramp-type Josephson junctions based on PLD films resulted in the modulation of the junction's critical current in applied magnetic field and the appearance of Shapiro steps by applied microwave irradiation.

The potential of achieving RSJ-behavior and relatively high operating temperatures make MgB_2 ramp-type junctions very suitable for electronic

circuits. To achieve the potentially large $I_C R_N$ - product in MgB_2 tunnel junctions, which is of interest for electronic application, the quality of thin films with respect to smoothness, film epitaxy as well as an artificial barrier-layer quality has to be improved.

Considerable improvements of the junction properties can be expected by using smooth, epitaxially grown thin films with bulk-like critical temperature values for the fabrication of the Josephson junctions. Suitable films would be the films prepared by the HPCVD techniques (as described in Section 5.2.2), since they fulfill the above-mentioned requirements. It is expected that a low surface roughness (about 2 nm) would result in the absence of shunting channels (pinholes) that would considerably improve the properties of the junctions.

As a preliminary experiment to demonstrate the properties of a weak link made in such film, nanobridges with 100 nm and 140 nm widths were fabricated. They had very high critical current densities in order of mid-10^7 A/cm^2, which is very promising for the use of this material in electronic devices and close to depairing current density values indicating strong vortex pinning in the films.

An important issue in the realization of Josephson junctions based on HPCVD films is the determination of a suitable barrier material. In the case of all-MgB_2 Josephson junctions, the barrier material should be crystalline with lattice parameters close to the MgB_2 lattice parameter to ensure the epitaxial growth of the top MgB_2 electrode. On the other hand, the growth temperature for the barrier material should not exceed the decomposition temperature of MgB_2.

One of the suitable candidates for the barrier material concerning its lattice match with MgB_2 would be hexagonal (alpha) AlN with the *a*-axis length being 3.110 Å and a big energy gap of 6.2 eV at 300 K [28]. *He et al.* [29] found that MgB_2 is inert with respect to AlN up to 700-800°C (Table 2.2, Section 2.4.1). Therefore, it is to be examined in the future if this material can be grown epitaxially below 800°C and which technique would be suitable for it, for instance the HPCVD method or PLD using an Al target and a nitrogen ambient gas.

Another suitable barrier material could be TiB_2 with a hexagonal *a*-axis length of 3.028 Å (Table 4.5, Section 4.4) [23]. *Zhai et al*. [23] have successfully grown epitaxial TiB_2 thin films at 600°C by PLD. The films had very smooth surfaces and TiB_2's good electrical conductivity makes it a promising material for MgB_2-based superconductor-normal metal-superconductor junctions.

References:

[1] D. C. Larbalastier *et al.*, Nature **410**, 186 (2001).
[2] Y. Bugoslavsky, G. K. Perkins, X. Qi, L. F. Cohen and A. D. Caplin, Nature **410**, 563 (2001).
[3] A. Brinkman *et al.*, Phys. Rev. B **65**, 180517 (R) (2002).
[4] J. Gao, W.A.M. Aarnink, G. J. Gerritsma, and H. Rogalla, Physica C **171**, 126 (1990).
[5] A. Brinkman, *Charge transport in double-barrier and magnesiumdiboride Josephson junctions*, PhD thesis, University of Twente, Enschede, The Netherlands (2003).
[6] D. Mijatovic *et al.*, Appl. Phys. Lett. **80**, 2141 (2002).
[7] K. K. Likharev, *Dynamics of Josephson Junctions and Circuits*, Taylor & Francis (1992).
[8] See *e.g.* A. Barone and G. Paterno, *Physics and Application of the Josephson effect*, Wiley, New York, 1982; K.K. Likharev, *Dynamics of Josephson Junctions and Circuits*, Gordon and Breach, New York (1986).
[9] B. H. Moeckly and K. Char, Appl. Phys. Lett. **71**, 2526 (1997).
[10] Y. Uzawa *et al*., Appl. Phys. Lett. **61**, 967 (1992).
[11] M. Faucher *et al*., Physica C **368**, 211 (2002).
[12] S. K. Lam and D. L. Tilbrook, Appl. Phys. Lett. **82**, 1078 (2003).
[13] D. H. A. Blank *et al*., IEEE Trans. Appl. Supercond. **5**, 2786 (1995).
[14] M. V. Pedyash, D. H. A. Blank, H. Rogalla, Appl. Phys. Lett. **68**, 1156, (1996).
[15] M. V. Pedyash, D. H. A. Blank, J. H. de Muijnck, H. Rogalla, IEEE Trans. Appl. Supercond. **7**, 2764 (1997).
[16] H. Rogalla, *High-T_C Josephson contacts. Preparation and properties*, Habilitation thesis, University of Giessen, Germany (1986).
[17] M.R. Eskildsen *et al*., Phys. Rev. Lett. **89**, 187003 (2002).
[18] C. Buzea and T. Yamashita, Supercond. Sci, Technol. **14**, R115 (2001).
[19] D. K. Finnemore, J. E. Ostenson, S. L. Bud'ko, G. Lapertot, P. C. Canfield, Phys. Rev. Lett. **86**, 2420 (2001).
[20] K. K. Likharev, Rev. Mod. Phys. **51**, 101 (1979).
[21] L.G. Aslamazov and A.I. Larkin, Sov. Phys. JETP **41**, 381 (1975).
[22] A. A. Golubov, A. Brinkman, O. V. Dolgov, J. Kortus, and O. Jepsen, Phys. Rev. B **66**, 054524 (2002).
[23] A. Brinkman *et al*., Appl. Phys. Lett. **79**, 2420 (2001).
[24] H. Y. Zhai, H. M. Christen, C. Cantoni, A. Goyal and D. H. Lowndes, Appl. Phys. Lett. **80**, 1963 (2002).
[25] J. F. Ziegler, J. P. Biersack and U. Littmark, *The stopping and range of ions in solids*, Pergamon Press, New York (1985).

[26] http://www.srim.org
[27] S. Y. Xu *et al*., Phys. Rev. B **68**, 224501 (2003).
[28] http://www.semiconductors.co.uk/nitrdes3189.htm#AlN
[29] T. He, R. J. Cava and J. M. Rowell, Appl. Phys. Lett. **80**, 291 (2002).

7

Superconducting Quantum Interference Devices (SQUIDs) based on MgB_2 nanobridges

Abstract

An essential step for future electronic devices based on MgB_2 is the fabrication of superconducting quantum interference devices (SQUIDs). All-MgB_2 SQUIDs based on focused-ion-beam patterned nanobridges have been made in MgB_2 thin films prepared by the PLD and HPCVD method.

The SQUIDs made in PLD films showed modulation voltages of up to 30 μV at 10 K. Voltage modulation was observed up to 20 K. These bridges, with a length scale smaller than 100 nm, have critical current densities of $7x10^6$ A/cm^2 at 4.2 K.

The 140 nm wide nanobridges of the SQUIDs made in the HPCVD films had an outstanding critical current of $5x10^7$ A/cm^2 at 4.2 K. Those SQUIDs showed modulation voltages of up to 25 μV at 27 K. Voltage modulation was observed until almost 38.8 K. Noise measurements on the magnetometer give a white noise level of 76 $\mu\phi_0/\sqrt{Hz}$ at 34.5 K in the frequency range from 0.1 Hz until 1 Hz. This gives an effective flux noise of 1 pT/$\sqrt{Hz}$.

7.1 Introduction

Superconducting Quantum Interference Devices (SQUIDs) consist usually of two Josephson junctions combined in a superconducting loop. In this early stage of MgB_2 development, the fabrication of the reproducible Josephson junctions with good properties is complicated. Apart from Josephson junctions, nanobridges can be used as the weak links in a SQUID [1], which are easier to form for the preliminary experiments. A lot of reports have been published on SQUIDs made in low-T_C superconductors (e.g., [2,3]) and in high-T_C superconductors (e.g., [4-6]).

In a superconducting ring, the total phase-change of the superconducting wave function when going around the loop is quantized in multiples of 2π. With the nanobridges incorporated in the ring, the phase-change is composed of two contributions. The first is due to the current flow through the nanobridges; $\Delta\varphi_1(I_1)$ and $\Delta\varphi_2(I_2)$, with I_1 and I_2 the currents through bridges 1 and 2, respectively, and the second is associated with the applied magnetic flux ϕ in the ring. With this, the quantization-condition becomes $\Delta\varphi_1-\Delta\varphi_2+2\pi(\phi/\phi_0) = 2\pi k$, with k an integer number and ϕ_0 the elemental flux quantum ($\phi_0 = 2.07\times10^{-15}$ Tm^2). The ring carries a dc-supercurrent for bias currents $I_{bias} = I_1+I_2$, for which this condition can be fulfilled. By varying the applied flux, the maximal attainable I_{bias} to fulfill the quantization-condition is modulated with a period ϕ_0. This critical current will be maximal when the enclosed flux equals n times ϕ_0 and is, generally speaking, minimal for $\phi = (n+1/2)\ \phi_0$, $n \in$ N.

The MgB_2 thin films used for the SQUID fabrication are prepared by PLD from Mg-enriched MgB_2 target and by the HPCVD method, as described in Chapter 5. Nanobridges fabricated in these films (as presented in Chapter 6) are incorporated into superconducting loops forming SQUIDs. The fabrication and electrical properties of these SQUIDs are discussed in this Chapter.

7.2 dc-SQUIDs made in PLD films

7.2.1 Fabrication

The MgB_2 thin films were prepared on MgO substrates from a Mg-enriched MgB_2 target, as described in Section 5.2.1. They are deposited at room temperature and subsequently annealed at 600°C and they were 200 nm thick. The transition temperature T_C of the as-deposited films is 24 K. These films are polycrystalline, which does not hamper the supercurrent, since the grain boundaries in MgB_2 act as strong links [7,8]. Nanobridges were fabricated by FIB

as described in Chapter 6. The nanobridges were incorporated in superconducting loops making the SQUIDs.

Typically, the SQUID and contact-paths were patterned in two steps [9]. First, the coarse structures, including the square-washer SQUID-ring and the contact leads were defined by standard photolithography and argon ion-beam milling. With an acceleration voltage of 500 V, the ion milling under an angle of 45° occurs at an etching rate of approximately 5 Å/s. The SQUID consists of a square-washer of 20x20 µm inner and 70x70 µm outer dimension and a 5x55 µm slit, as is shown in Fig. 7.1(a). Further, the structure contains two striplines, 30 µm long and 5 µm wide, into which nanobridges were structured by direct Focused Ion Beam (FIB) milling. Using a 25 kV Ga^+ beam with a diameter of 50 nm (Full Width at Half Maximum) and a beam current of 40 pA, trenches are etched in the MgB_2 films at a rate of 0.30 mm^3/C. The density of the Ga^+ ions has a Gaussian distribution in the central part of the beam. The nanobridges are made by letting two beam profiles partly overlap, which results in a reduced height of the bridge, as compared to the original film thickness. The dimensions of the fabricated nanobridges are shown in Fig. 7.1(b); the width is about 70 nm (FWHM) and the height of the nanobridges is approximately 150 nm. The length of the bridges is 150 nm. The dimensions of the bridge are determined from the known beam profile and analysis of Scanning Electron Microscopy images (Fig. 7.1(c)).

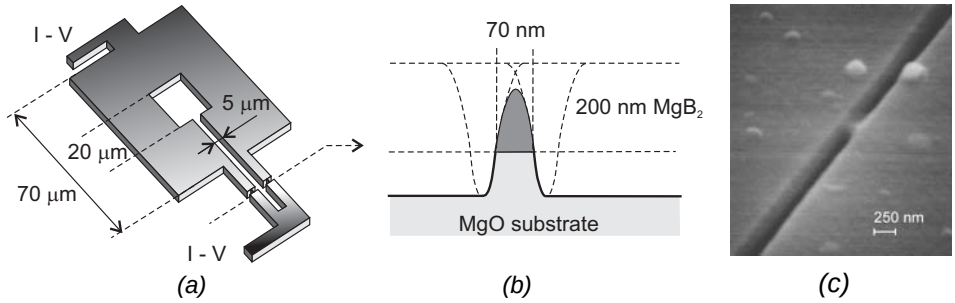

Fig. 7.1 *(a) Schematic layout of the SQUIDs; (b) Schematic cross-section of the nanobridges [9]; (c) Scanning Electron Microscope image of an MgB_2 nanobridge (70x150 nm) [9].*

7.2.2 Electrical properties

The electrical transport properties of the ring-structure were measured in a four-point configuration in a shielded variable-temperature flow-cryostat. The transition temperature of the structures was typically found to be 22 K, comparable to the original T_C value of the unpatterned film. In Fig. 7.2(a), a typical example of the measured SQUID current-voltage characteristics is shown for the two extremal values of the enclosed magnetic flux of the SQUID, at a temperature T = 19 K. Above T = 12 K the current-voltage characteristics are non-hysteretic, with a parabolic shape of the voltage branch as it is expected for the rounded bridges [10]. Below 12 K a hysteresis appears, as can be seen in the inset of Fig. 7.2(a) where a current-voltage characteristic at 10 K is shown. This hysteresis is presumed to arise from the considerable heating of the bridges by the large bias-currents needed at these temperatures. In Fig. 7.2(b), the measured critical current dependence on temperature is depicted. For a rounded bridge edge, as is the case here, the critical current is expected to be proportional to λ^{-2} and ξ^{-1}, as described in [11]. In this Figure the BCS fit is presented as well as the theoretical fit where the values for penetration depth are calculated from the two-band model [12], in the dirty case in the *a*-*b* plane. Both fits show a rather good agreement with the measured values. This can be explained by the fact that the PLD sample is in the dirty limit (as determined from the electron mean free path obtained from the upper critical field measurements given in Section 5.3.1 and the reduced value of T_C). This can cause the converging of the two superconducting gaps into one and enables the use of the BCS theory. A two-band model in the *a*-*b*-plane for the dirty case where still two gaps exist [12] fits well too. In that case, the MgB_2 grains should be oriented in a preferred direction, but the absence of the XRD peaks disallows the determination of the grains orientation. The presence of anisotropy in the H_{C2} measurements (Section 5.3.1) shows that some degree of grain orientation exists, but the direction and the quantity cannot be determined.

The critical current of the SQUID at T = 4.2 K is 1.5 mA [9]. With an estimated bridge cross-section of 70x150 nm this results in a critical current density of 7×10^6 A/cm^2. This large value implies that the nanostructuring by the use of a Ga focused ion beam is very well possible while maintaining large critical current densities. This important information shows that the chemical reactivity and volatility of the magnesium do not pose problems in the nanostructuring. Furthermore, it is noted that the structures are very stable over time and show constant properties after thermal cycling or exposure to moisture.

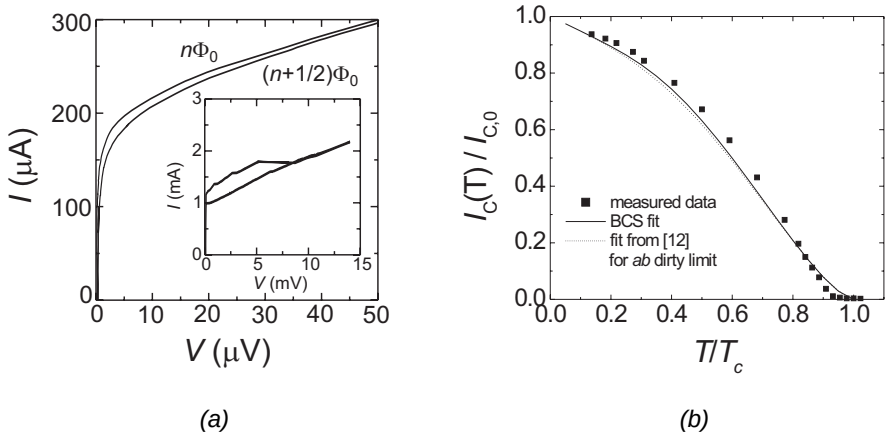

(a) *(b)*

Fig. 7.2 *(a) Current-voltage characteristics of a SQUID at T = 19 K for different values of the enclosed magnetic flux. In the inset, a hysteretic current-voltage characteristic is shown for T = 10 K, (b) Critical current of the SQUID as function of temperature. The solid line shows the fit from the BCS theory and the dotted line presents the fit from [12] for the dirty case in the a-b plane.*

If we assume the applicability of the RSJ-model on the nanobridges of a dc-SQUID, the lowest noise of the dc-SQUID could be achieved if the parameter β_L, defined as:

$$\beta_L = \frac{2I_{C,bridge}L}{\phi_0} \tag{7.1}$$

is in the order of 1 [13]. L is the SQUID inductance and $I_{C,bridge}$ is the critical current of each individual bridge, which is assumed to be the same for both bridges.

The SQUID inductance is the sum of the geometrical inductance and the kinetic inductance. The geometrical inductance is estimated by the FastHenry program [14] to be 60 pH. The kinetic inductance is defined as:

$$L_{kin} = 1.25 \cdot 10^{-6} \frac{\lambda^2}{d} \frac{2l}{w}, \tag{7.2}$$

where λ is the London penetration depth, d the film thickness, l is the length of the superconducting stripline and w is the width of the strip. For the SQUID presented in Fig. 7.1 kinetic inductance is about 1 pH, using a penetration depth value of 62 nm (that we obtained from the measurements shown in Section 7.4.2).

At the temperature of 19 K, the $I_{C,bridge}$ value is 0.06 mA (Fig. 7.2(b)). This gives a β_L value of 3.5. The modulation of the critical current in RSJ-model defined as:

$$\Delta I_C = \frac{2I_{C,bridge}}{1+\beta_L} \tag{7.3}$$

would give a modulation depth in current of about 22%. The measured modulation depth at this temperature is, however, about 5%. The reason for this discrepancy could be the use of the RSJ-model, which is not fully applicable to the nanobridges, since the behavior of the nanobridges is dominated by flux motion [10]. Effects of pinning and the vortex dynamics are not included in the basic RSJ-model [10].

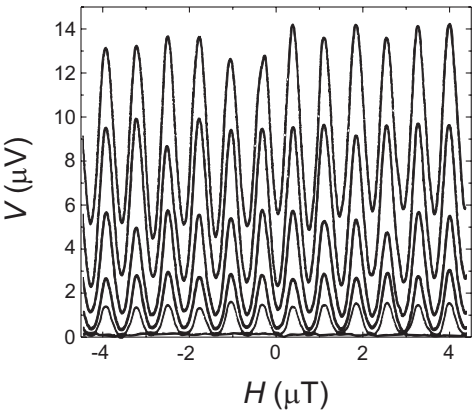

Fig. 7.3 *SQUID voltage modulation by applied magnetic field at 15 K, at different values of the current bias [9].*

In Fig. 7.3, the voltage modulation of the SQUID at different constant bias currents is shown as a function of the applied magnetic field. The period of the modulation in Fig. 7.5 is 0.74 μT. With a period of ϕ_0 for the SQUID critical current modulation by applied magnetic flux, an effective SQUID area, $A_{eff} = \phi_0/H$, of 2.8×10^3 μm^2 is obtained, which is in well accordance with the actual SQUID dimensions, taking flux-focusing by the superconducting washer into account [14]. Above the temperature at which the current-voltage characteristics become hysteretic, the voltage modulation shows the same temperature dependence as the critical current. A modulation voltage of 30 μV was observed at 10 K. Voltage modulation was observed up to 20 K [9].

7.3 dc-SQUIDs made in HPCVD films

7.3.1 Fabrication

MgB_2 thin films (5x5 mm^2) prepared by the HPCVD method (as described in Section 5.2.2) were structured in the similar way as the samples made by PLD (Section 7.2.1).

The thickness of the films was about 100 nm. They were deposited on SiC with 50 sccm and 100 sccm B_2H_6 gas mixture flow rates. They were rather smooth with r.m.s. roughness of about 2 nm for the sample with 50 sccm B_2H_6 gas mixture flow rate and about 5 nm for the sample with 100 sccm B_2H_6 gas mixture flow rate. Prior to the film structuring a 25 nm gold layer was deposited by RF sputter deposition to protect the film from degradation during structuring caused by the sensitivity of the MgB_2 to water [15,16].

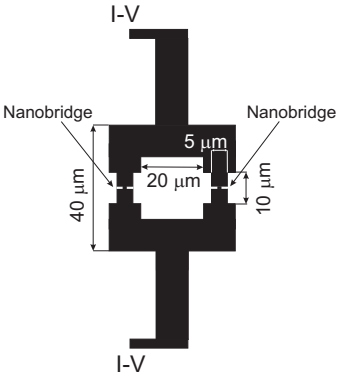

Fig. 7.4 *Schematic layout of the SQUIDs made in the HPCVD films.*

First, the coarse structures (Fig. 7.4), including the square-washer SQUID-ring and the contact leads were defined by standard photolithography and argon ion-beam milling followed by the fabrication of the nanobridges (Fig. 7.4) by FIB. This was done in the same way as for the samples made by PLD (Section 7.2.1). Nanobridges of 140 nm or 100 nm widths were structured in the 5x10 μm^2 strip lines.

7.3.2 Electrical properties

The measurements were performed in the same way as for SQUIDs made in the PLD films (Section 7.2.2). The residual resistance ratio (RRR) of the

SQUID with 140 nm wide nanobridges was about 27 (Fig. 7.5). The high RRR ratio can be attributed to the presence of extra Mg (as discussed in Chapter 5, Section 5.3.2), but the high J_C (as it will be shown later) indicates that the extra Mg is not obstacles for the current flow, i.e., it is not incorporated in the MgB_2 grains.

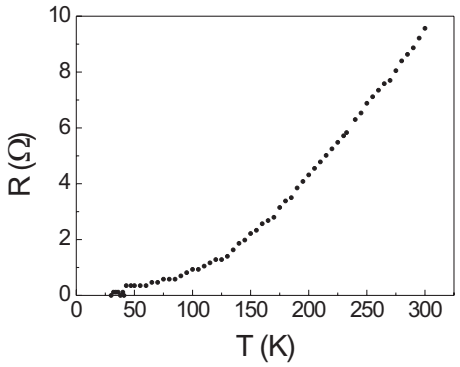

Fig. 7.5 *R-T measurements of the SQUID with 140 nm wide nanobridges.*

In Fig. 7.6, a typical example of the measured SQUID current-voltage characteristics at a temperature T = 35.2 K is depicted. Above T = 15 K the current-voltage characteristics are non-hysteretic. The darkened area just above I_C indicates the SQUID modulation range as the curve was recorded with a sweeping magnetic field of a few flux quanta. Below 15 K a thermal hysteresis appears in some SQUIDs, as can be seen in the inset of Fig. 7.6 where a current-voltage characteristic at 7 K is shown. Most of the SQUIDs did not show any hysteresis in the whole temperature region. The reason why in some SQUIDs hysteresis does not appear is not completely understood at this stage of the experiments.

The critical current of the SQUID at T = 4.2 K is 14 mA. With an estimated bridge cross-section of 140x100 nm^2 this results in a high critical current density of $5x10^7$ A/cm^2 in the bridge, which indicates the good film quality in the bridges and SQUID.

The RSJ-model is used to estimate a modulation depth in the *I-V* characteristics, as in Section 7.2.2 (eq. (7.1)-(7.3)). The geometrical SQUID inductance for the SQUID presented in Fig. 7.4 was calculated by the software FastHenry [17] and it has a value of 48 pH. The kinetic inductance for the SQUID with 140 nm wide nanobridges is estimated to be about 0.75 pH. At 35.2 K, $I_{C,bridge}$ is 0.15 mA, which gives a β_L value of 7. This would give a current modulation depth of about 12%. The measured modulation depth, on the other hand, is about 2%, which shows that also in this case the RSJ-model cannot be

used for the approximation of the current modulation depth of the SQUIDs based on the nanobridges.

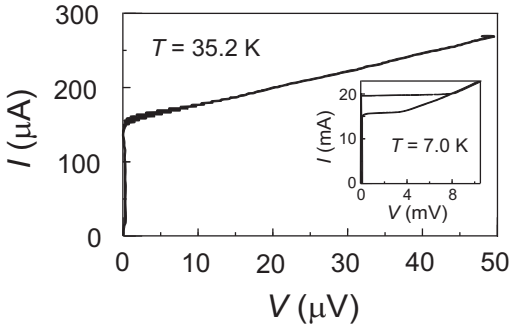

Fig. 7.6 *Current-voltage characteristics of the SQUID with 140 nm wide nanobridges at T = 35.2 K for different values of the enclosed magnetic flux. In the inset, a hysteretic current-voltage characteristic at T = 7 K is shown.*

In Fig. 7.7 the measured temperature dependence of the critical current for the SQUIDs with 140 and 100 nm wide nanobridges are depicted. For a rounded bridge edge, as is the case here, the critical current is expected to be proportional to product of λ^{-2} and ξ^{-1}, as described in [10]. Given the temperature dependence for λ from the two-band model [12] and the experimental fit for coherence length $\xi \sim (1-T/T_C)^{0.59}$ in the *a-b* plane in the clean limit [18], the measured I_C vs. T dependence can be very well fitted for both SQUIDs, as shown in Fig. 7.7.

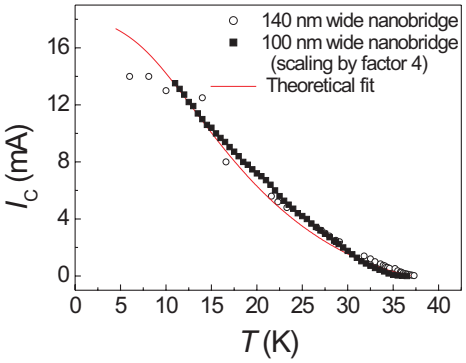

Fig. 7.7 *I_C vs. T dependence of the SQUIDs with 100 nm and 140 nm wide nanobridges. Solid line represents the theoretical fit for I_C.*

In Fig. 7.8, the voltage modulation of the SQUID at different constant bias currents is shown as a function of the applied magnetic field. Estimating the *B*/*I* – ratio of the coil to be ~ 1.4 μT/mA. One magnetic flux quantum ϕ_0 corresponds to 1.4 mA (the current supplied through the coil), which gives a period of magnetic field of 1.6 μT. An effective SQUID area of about 1.3×10^3 μm^2 is obtained (calculated in the same way as in Section 7.2.2), which is in well accordance with the actual SQUID dimensions, taking flux-focusing by the superconducting washer into account [19]. Voltage modulation was observed up to 38.8 K, meaning that the SQUID could easily operate at rather high temperature (around 37 K). A maximum voltage modulation of 8 μV_{p-p} and a maximum voltage transfer of 25 $\mu V/\phi_0$ by applied magnetic field has been observed up to 37 K (Fig. 7.8), which presents an outstanding value for MgB_2 SQUID operation.

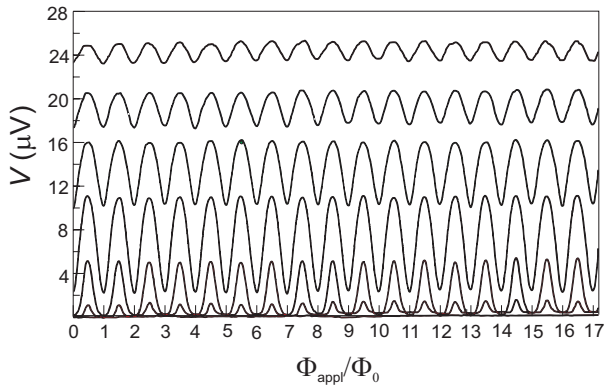

Fig. 7.8 *SQUID voltage modulation by applied magnetic field at 37 K for the SQUID with 140 nm wide nanobridges, at different values of the current bias. Voltage modulation shows maximum value of 8 μV_{p-p} and a maximum flux to voltage transfer of 25 $\mu V/\phi_0$.*

Fig. 7.9 illustrates the voltage and current modulation vs. temperature for the SQUIDs with 100 nm and 140 nm wide nanobridges. The voltage modulations were measured for both SQUIDs and the current modulations were calculated using the RSJ model and the measured values of critical current (using the eq. (7.1)-(7.3)). Although there is a discrepancy with the RSJ-model (as discussed above), it is used up to a certain extent for the qualitative analysis of the temperature dependence of the current and voltage modulation. It can be noticed that qualitatively current and voltage modulations of the same SQUIDs have the same temperature dependence in the high-temperature region. However, in the low-temperature region the current and voltage dependences differ. In the calculation of the current modulation the effects of pinning and the vortex dynamics are not taken into account, which might explain the discrepancy

between the current modulation and the voltage modulation behavior in the low-temperature region. For more precise results the temperature dependence of the penetration depth from the two-band model [12] should be included in the calculation of the current modulation. To explain the difference in the voltage modulations of the SQUIDs with 100 nm and 140 nm wide nanobridges (Fig. 7.9) more experiments are needed.

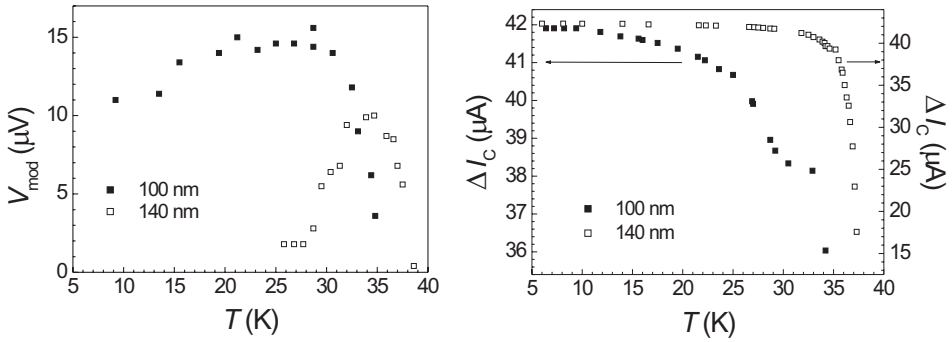

Fig. 7.9 *(a) Measured voltage modulation vs. temperature of the SQUID with 100 nm and 140 nm wide nanobridges; (b) Calculated current modulation vs. temperature of the same SQUIDs.*

7.4 dc-SQUIDs with directly coupled pick-up loop

7.4.1 Fabrication

An inductively shunted MgB_2 dc-SQUID magnetometer is structured in a 100 nm thick MgB_2 film with dimensions of 5x5 mm^2. The film was made by the HPCVD method on SiC substrate with 150 sccm B_2H_6 gas mixture flow. The r.m.s. roughness was about 4 nm. It is structured in a similar way as the SQUIDs described in Section 7.3.1. The coarse structure is made by standard photolithography and the nanobridges are fabricated by FIB. In Fig. 7.10 a schematic presentation of the inductively shunted dc-SQUIDs based on nanobridges is presented. There are five SQUIDs coupled to the same inductance shunt (Fig. 7.10(a)). Two nanobridges of 100 nm widths were fabricated in the striplines (Fig. 7.10(b)).

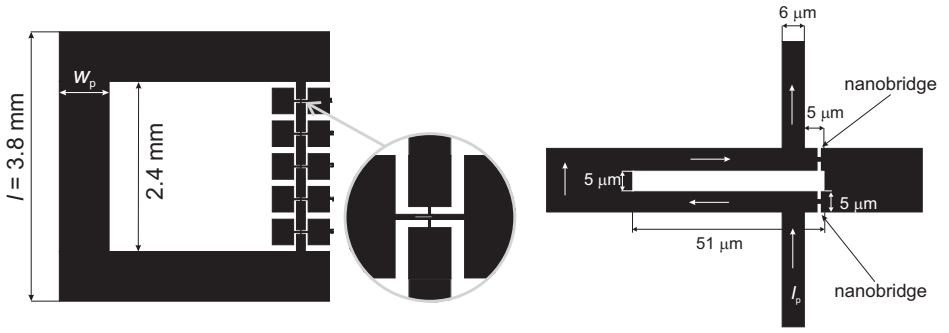

Fig. 7.10 *The design of directly coupled pick up loop of dc-SQUID. (a) The design of the whole magnetometer with a magnification of the striplines; (b) Magnified striplines with their dimensions and nanobridges.*

7.4.2 Magnetometer properties

Fig. 7.11 represents the non-hysteretic current-voltage characteristics of the magnetometer (SQUID) at 34.5 K. The I_C value is 0.6 mA, which is about two times higher than for the SQUID with the nanobridges of the same widths presented in Section 7.3.2 (Fig. 7.7). This can be attributed to the different sample and different deposition conditions. The sample used for magnetometer fabrication, is prepared with a higher B_2H_6 gas mixture flow rate. This influenced the increase of the MgB_2 grains (as discussed in Section 5.2.2) and subsequently the presence of less grain boundaries and fewer impurities. Therefore, it can be anticipated that the nanobridges are not positioned across the grain boundaries and less impurities reduce the obstacles in the current flow. However, more experiments are needed to confirm these anticipations.

Voltage modulation vs. temperature is shown in the inset of Fig. 7.11 and it is similar to the temperature dependences of the voltage modulations presented in Fig. 7.9(a). The maximum of the voltage modulation (~ 6 $\mu V_{p\text{-}p}$) was in the temperature range of 32 to 35 K and therefore the noise measurements were done at 34.5 K. In Fig. 7.12 the voltage modulation in applied magnetic field is depicted.

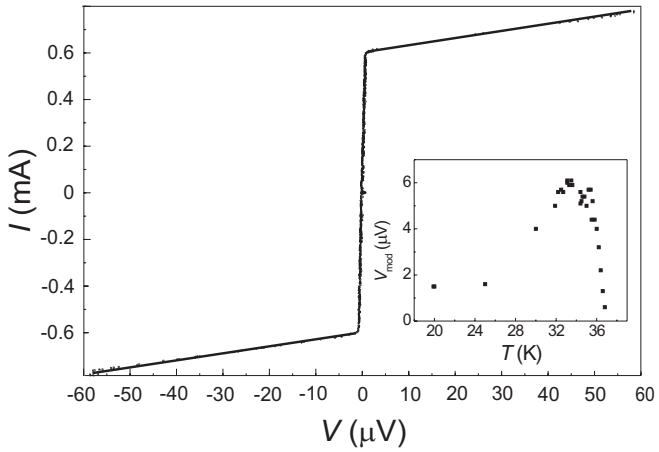

Fig. 7.11 *Current voltage modulation of the magnetometer at T = 34.5 K. The inset shows temperature dependence of the voltage modulation.*

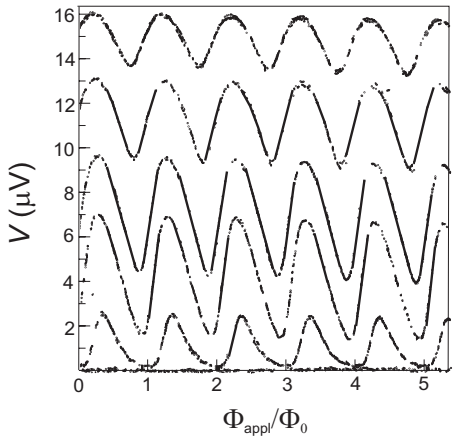

Fig. 7.12 *SQUID voltage modulation by applied magnetic field at T = 34.5 K at different values of the bias current.*

The bias current was adjusted to maximize the voltage modulation. The period of the voltage modulation was temperature dependent. This was recorded and used for estimation of the effective area of the SQUID magnetometer and the penetration depth value at 0 K.

The effective magnetic field noise $S_B^{1/2}(\omega)$ of a dc-SQUID is given by the ratio of the effective flux noise $S_\phi^{1/2}(\omega)$ and the effective sensing area A_{eff} as:

$$S_B^{1/2}(\omega) \propto \frac{S_\phi^{1/2}(\omega)}{A_{eff}} \tag{7.4}$$

$S_\phi^{1/2}$ (ω) increases approximately with $L^{3/2}$, with L being the SQUID inductance [20]. A low SQUID inductance and large effective area are required to obtain minimum effective magnetic field noise. A simple method to combine a low L and a large A_{eff} is to shunt the SQUID by a large area shunt inductance as it is done here. In this way, the current I_p (screening current) induced by the applied flux in the shunt inductance (L_p), with area A_p, is directly coupled to the low inductance SQUID loop.

The effective sensing area A_{eff} of the magnetometer is given by [20]:

$$A_{eff} = \frac{L_c A_p}{L_p + L_c} + A_{sq} \tag{7.5}$$

The coupling inductance L_c is defined as $L_c = \phi_c / I_p$, with ϕ_c being the magnetic flux coupled to the SQUID loop due to the screening current I_p. A_{sq} is the effective flux focusing area of the SQUID itself, without the inductive shunt. The value of coupling inductance is comparably small to the shunt inductance. By taking $A_{sq} << A_p$ and $L_c << L_p$, the eq. (7.5) is simplified to:

$$A_{eff} \propto \frac{L_c}{L_p} A_p . \tag{7.6}$$

From this equation it implies that a large pick-up loop is required to have a large effective area.

The pick up inductance L_p is given by [21]:

$$L_p = \frac{2\mu_0 (l - 2w_p)}{\pi} \left(\ln \frac{l - 2w_p}{w_p} + 0.5 \right), \tag{7.7}$$

with l the side length and w_p the width of the loop (see Fig. 7.10). This equation well describes the inductance of the square washer if w_p/l < 1/5 [21]. The dimensions of our magnetometer washer satisfy this condition. L_p is 2.6 nH for our magnetometer.

The effective flux focusing area of planar loops is defined as [14]:

$$A_p = Cl(l - 2w_p), \tag{7.8}$$

with C being a constant in the order of unity. For our magnetometer it has a value of 9.1 mm^2.

The coupling SQUID inductance L_c is a contribution of slit inductance L_{slit} (geometrical inductance) and kinetic inductance L_{kin}. The slit inductance is approximated by the expression [22,23]:

$$L_{slit} = 0.4\pi \frac{K(k)}{K'(k)} \cdot 10^{-6} \cdot l_{slit} , \tag{7.9}$$

where l_{slit} is the slit length and $k=s/(s+2w)$, with s the slit width and w the width of the superconducting strips. K represents the complete elliptic integral of the first kind and K' is its complementary function $K'=K(1-k^2)$. The ratio $K(k)/K'(k)$ is approximated by:

$$\frac{K(k)}{K'(k)} = \left[\frac{1}{\pi}\ln\left(2\frac{1+\sqrt{k_c}}{1-\sqrt{k_c}}\right)\right]^{-1} \tag{7.10}$$

for $0.7 \le k_c \le 1$, with $k_c\sqrt{1-k^2}$.

Taking into account that after structuring *s* had a value of 4 μm and *w* was 6 μm and l_{slit} was 51 μm, L_{slit} is estimated to be 37 pH.

L_{kin} is approximated as [20]:

$$L_{kin} = 1.25\cdot 10^{-6}\frac{\lambda^2}{d}\frac{2l_{slit}}{w}, \tag{7.11}$$

with λ the London penetration depth and *d* the film thickness. L_{kin} is in our case $L_{kin} \sim 2\text{x}10^2\ \lambda^2$ (T).

The flux induced by the current I_p covers about 80% of the area enclosed by the striplines (Fig. 7.10(b)) and therefore the coupling inductance L_c is 80% of the sum of L_{slit} and L_{kin} values. Using the L_c, L_p and A_p values in eq. (7.6) effective area becomes: $A_{eff} = A_{eff}(0) + \text{const}\ \lambda^2$ (for λ expressed in m). Modulation of the current applied through the coil was measured and using the conversion factor from applied current to the external field we calculated the effective area as $A_{eff} = \phi_0/H_{ext}$. The temperature dependence of the A_{eff} is presented in Fig. 7.13. The penetration depth value at 0 K is estimated from the fit of this dependence. In this fit the temperature dependence of the penetration depth from the two-band model in the *a-b* plane in the clean limit [12] was used. The estimated value for λ at 0 K is 62 nm.

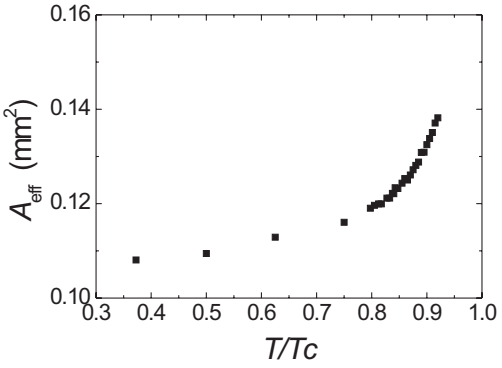

Fig. 7.13 *Temperature dependence of the magnetometer effective area.*

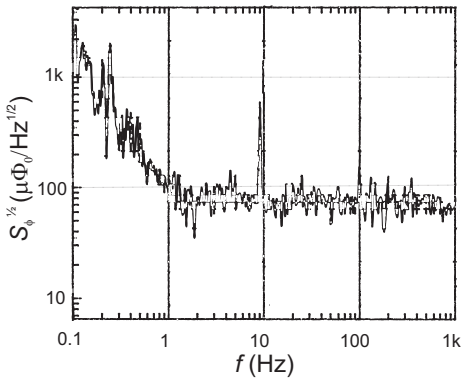

Fig. 7.14 *Noise measurements of the magnetometer with 100 nm wide nanobridges in the frequency range of 0.1 Hz to 1 kHz.*

In Fig. 7.14 the effective input flux noise $S_\phi^{1/2}(\omega)$ measured at 34.5 K is shown. In flux locked loop mode, a white noise level of 76 $\mu\phi_0/\sqrt{Hz}$ ($S_B^{1/2}$ = 1 pT/√Hz) is measured above 1 Hz up to 1 kHz. Below 1 Hz, a 1/f noise characteristic appears.

The white noise level of the SQUID with 100 nm wide nanobridges, which is not incorporated in magnetometer (Section 7.3) was 30 $\mu\phi_0/\sqrt{Hz}$ at 28.7 K. This lower noise level can be attributed to the different sample and different MgB_2 grain sizes, i.e., different quality of the nanobridges and to the lower temperature of measurements. We estimated that the effective area for this SQUID is about $1.3x10^3$ μm^2 (Section 7.3.2), which gives an effective magnetic noise value of about 23 pT/√Hz. The sensitivity of that SQUID is not enough to measure the magnetic signal evolving from human heart activity. The magnetometer has, on the other hand, a larger effective area, i.e., lower effective magnetic field noise, which gives a value of 1 pT/√Hz. This value illustrates that the magnetometer can be used to record adult magnetocardiogram (MCG) [24]. For HTS magnetometers, lower sensitivity values were reported (~ 20-100 fT/√Hz at 1 Hz at 77 K, see e.g., [25,26]) fabricated on larger samples (1-4 cm^2). Using larger MgB_2 samples, the magnetic field noise level in inductively shunted dc SQUIDs is expected to be lower than reported here. In our case the sensitivity is in the limits of the required one, but the larger the pick-up loop, i.e., the use of the larger samples would give even higher sensitivity.

The critical current of our nanobridges (100 nm wide) is very large i.e., it varies from 7 to 1000 μA in the temperature range of 37.8 till 33.5 K. Maximum peak-to-peak voltage modulation of our magnetometers was 6 μV from 35 until 32 K (inset in Fig. 7.11). This is a small value as compared to the dc-SQUIDs

based on HTS material (see e.g., [27]). A small voltage modulation is influenced by such a large critical current. A higher peak-to-peak voltage modulation is needed to improve the signal-to-noise ratio. To achieve that, smaller and more reproducible nanobridges are needed.

7.5 Conclusions

SQUIDs based on nanobridges were fabricated in MgB_2 thin films made by the PLD and HPCVD techniques.

Superconducting structures were realized on a length scale smaller than 100 nm in *in-situ* fabricated MgB_2 films made by PLD. The nanobridges have critical current densities of $7x10^6$ A/cm^2 at 4.2 K indicating good superconducting properties of the films and nanostructures. MgB_2 ring-structures incorporating nanobridges display Josephson quantum interference effects, which forms the basis for the creation of all-MgB_2 SQUIDs. Voltage modulation was observed up to 20 K, which makes them already operable on those temperatures that can be achieved with cryocoolers.

Nanobridges in the SQUIDs formed in epitaxial MgB_2 thin films were down to 100 nm wide. The bridges showed a very high critical current density of $5x10^7$ A/cm^2 at 4.2 K indicating very good film quality of the thin films and nanostructures. These SQUIDs showed an outstanding voltage modulation in applied magnetic field. It was observed until 38.8 K. This allows the operation of the SQUIDs at about 30 K, which is a considerably higher operating temperature than the operating temperature of the SQUIDs made in the PLD films.

The white noise level measured on MgB_2 magnetometer was 76 $\mu\phi_0/\sqrt{Hz}$ measured from 1 Hz to 1 kHz and the effective field noise was 1 pT/$\sqrt{Hz}$ at 34.5 K, which is sensitive enough for recording adult MCG. At this early stage of MgB_2 thin film device development this is a satisfactory result and illustrates that by improving the device quality MgB_2 is a very promising material for electronic applications.

References:

[1] K. K. Likharev, *Dynamics of Josephson Junctions and Circuits*, Taylor & Francis (1992).
[2] M. Faucher *et al*., Physica C **368**, 211 (2002).
[3] S. K. Lam and D. L. Tilbrook, Appl. Phys. Lett. **82**, 1078 (2003).
[4] D. H. A. Blank *et al*., IEEE Trans. Appl. Supercond. **5**, 2786 (1995).
[5] M. V. Pedyash, D. H. A. Blank, H. Rogalla, Appl. Phys. Lett. **68**, 1156 (1996).
[6] M. V. Pedyash, D. H. A. Blank, J. H. de Muijnck, H. Rogalla, IEEE Trans. Appl. Supercond. **7**, 2764 (1997).
[7] D. C. Larbalestier *et al.*, Nature (London) **410**, 186 (2001).
[8] D. K. Finnemore, J. E. Ostenson, S. L. Bud'ko, G. Lapertot, P. C. Canfield, Phys. Rev. Lett. **86**, 2420 (2001).
[9] A. Brinkman *et al*., Appl. Phys. Lett. **79**, 2420 (2001).
[10] H. Rogalla, *High-T_C Josephson contacts. Preparation and properties*, Habilitation thesis, University of Giessen, Germany (1986).
[11] M. Tinkham, *Introduction to Superconductivity*, McGraw-Hill, New York, (1996).
[12] A. A. Golubov *et al*., Phys. Rev. B **66**, 054524 (2002).
[13] C. Tesche and J. Clarke, J. Low Temp. Phys. **29**, 301 (1977).
[14] M. B. Ketchen, W. J. Gallagher, A. W. Kleinsasser, S. Murphy, *SQUID '85 – Suprconducting Quantum Interference Devices and their Applications*, Walter de Gruyter & Co., Berlin (1985).
[15] H. Y. Zhai *et al*., Supercond. Sci. Technol. **14,** 425 (2001).
[16] D. K. Aswal *et al*., Physica C **363**, 208 (2001).
[17] FastHenry, version 3.0 by M. Kamon, L. M. Silveira, C. Smithhisler and J. White (1996).
[18] S.-Y. Xu, Qi Li and X. X. Xi, *Experimental dependence of the coherence length measured at Penn State University*, private communication.
[19] D. Mijatovic *et al*., unpublished
[20] H. Hilgenkamp, *High-T_C dc SQUID magnetometers,* PhD thesis*,* University of Twente, The Netherlands (1995).
[21] M. B. Ketchen, IEEE Trans. Magn. **23**, 3040 (1991).
[22] L. N. Smith, D. W. Jillie and H. Kroger, IEEE Trans. Magn. **21**, 874 (1985).
[23] K. C. Gupta, R. Garg, R. Chadha, *Computer aided design of microwave circuits*, Artech House, Dedham (1981).
[24] A. P. Rijpma, *Fetal hear monitor,* PhD thesis*,* University of Twente, The Netherlands (1995).
[25] D. Koelle *et al*., Appl. Phys. Lett. **63**, 2271 (1993).

[26] R. Cantor, L. P. Lee, M. Teepe, V. Vinetskiy and J. Long, IEEE Trans. Appl. Supercond. **5**, 2927 (1995).

[27] A. Jansman, *High-T_C dc SQUID for use in a background filed,* PhD thesis, University of Twente, The Netherlands (1995).

Summary

Magnesium-diboride (MgB_2) has been synthesized for the first time in the 1950's, but its superconducting properties were discovered almost 5 decades later. It has a superconducting transition temperature of T_C = 39 K, which enables electronic circuits based on this material to operate at a much higher temperature (~ 25 K) than low-temperature superconductors, using compact cryocoolers. MgB_2 is simpler, cheaper and more stable over time as compared to high-temperature superconductors, with less anisotropy allowing efficient vortex pinning. This, together with the advantageous properties, like a relatively long coherence length and a high critical current density makes this material attractive for a number of applications as well as for fundamental studies, like the two-band superconductivity.

Superconducting MgB_2 thin films are of great interest for such basic studies and electronic application. Ideally, epitaxial MgB_2 thin films with a bulk-like value of T_C are desired, which implies that deposition at high temperatures (usually above 600°C) is needed. The high Mg vapor pressure, the low Mg sticking coefficient at elevated temperatures as well as the high Mg and B sensitivity to oxygen are challenging factors in the thin film deposition. These need to be overcome, especially in obtaining smooth and single-phase films suitable for multilayer structures used in superconducting electronics.

Superconducting MgB_2 thin films, presented in this thesis, were prepared in two ways: by pulsed-laser deposition (PLD) and by Hybrid Physical-Chemical Vapor Deposition (HPCVD).

The films deposited by PLD became superconducting after a two-step deposition process: deposition at low temperature (at room temperature or 200°C) followed by a high-temperature (~ 600°C) annealing step. These films were deposited from an Mg-enriched MgB_2 target and as multilayers alternatingly from Mg and B targets. The extra Mg and a high laser repetition rate were used to compensate for Mg loss, which is a consequence of the Mg volatility. The films showed $T_{C,0}$-values up to 28 K. The reduced transition temperature as compared to the bulk value is attributed to the small MgB_2 grain-sizes (smaller than 5 nm), impurities present in the starting material and MgO inclusions formed in the films. The electron mean-free path value determined for those films confirmed that they are in the dirty limit. The films were polycrystalline with very small grain sizes and therefore the choice of the substrate was not significant for the films prepared by this method.

In the HPCVD method evaporation of solid Mg and a high ambient pressure (~ 100 Torr) assured higher Mg fluxes than in the PLD method, which enables the fabrication of the superconducting films in one-step at elevated temperatures (~ 720°C), resulting in bulk-like values for T_C. X-ray diffraction data showed that the films grew epitaxially on both SiC and Al_2O_3 substrates. The films grown on Al_2O_3 rotated by 30° to reduce the lattice misfit, and literature reports indicate that MgO regions were formed at the MgB_2/Al_2O_3 interface. On the other hand, MgB_2 grew without any rotation on SiC due to the low misfit and no reaction was observed. The films were rather smooth (r.m.s. roughness was ~ 2.5-11 nm) depending on the substrate used, which makes them suitable for further structuring. The electron mean-free path value of those films showed that they are in the clean limit.

The PLD and HPCVD films were used for the fabrication of weak links in the form of Josephson junctions and nanobridges, which presents an important step for further implementation of MgB_2 into electronics and superconducting sensors.

Ramp-type Josephson junctions based on the PLD films showed a modulation of the junction's critical current in applied magnetic field and the appearance of Shapiro steps by applied microwave irradiation. These modulations on the polycrystalline films illustrate that the grain boundaries act as strong links, not critically affecting the superconducting phase coherence of the film area. Further improvement in the junction's properties can be achieved using epitaxial films with bulk-like values of T_C.

Weak links in form of nanobridges (down to 100 nm width) were made in the HPCVD films as a preliminary experiment to demonstrate the properties of a weak link made in epitaxial films. Critical current densities of those nanobridges were in order of mid-10^7 A/cm^2 at 4.2 K. This reveals a very good quality of the thin films and nanostructures.

Superconducting Quantum Interference Devices (SQUIDs) based on nanobridges were realized in the PLD and HPCVD films. The nanobridges prepared in the PLD films have critical current densities of $7x10^6$ A/cm^2 at 4.2 K indicating good superconducting properties of the films and nanostructures. Voltage modulation was observed up to 20 K, which makes them already operable at temperatures attainable with relatively small cryocoolers. The SQUIDs made on the HPCVD films had also a critical current density of $5x10^7$ A/cm^2 at 4.2 K. They showed an outstanding voltage modulation in applied magnetic field, observed until 38.8 K. This allows the operation of the SQUIDs at about 30 K.

The white noise level measured on an inductively shunted MgB_2 magnetometer was 76 $\mu\phi_0/\sqrt{Hz}$ in the frequency range from 1 Hz to 1 kHz and the effective flux noise was 1 pT/$\sqrt{Hz}$ at 34.5 K, which is sensitive enough for recording an adult magnetocardiogram MCG. This preliminary result is very promising for the use of MgB_2 thin film based devices in bio-magnetic measurements.

Samenvatting (Summary in Dutch)

Hoewel magnesium-diboride al in de jaren vijftig voor het eerst gesynthetiseerd werd, zijn de supergeleidende eigenschappen pas vijf decennia later ontdekt. De overgangstemperatuur T_C is 39 K. Dit biedt de mogelijkheid om elektronische schakelingen die zijn gebaseerd op dit materiaal te gebruiken bij hogere temperaturen (~25 K) dan voor lage temperatuur supergeleiders het geval is, zodat compactere cryokoelers gebruikt kunnen worden. Daarnaast is MgB_2 eenvoudiger van samenstelling, goedkoper en chemisch stabieler dan hoge temperatuur supergeleiders en is het bovendien meer isotroop, zodat efficiëntere vortex pinning mogelijk wordt. Bovenstaande argumenten, samen met de relatief lange coherentie lengte en hoge kritieke stroomdichtheid maken dat dit materiaal interessant is voor verschillende toepassingen. Verder is het, bijvoorbeeld door de tweebandige supergeleiding, zeer interessant voor fundamenteel onderzoek.

Supergeleidende dunne lagen gemaakt van MgB_2 zijn zeer bruikbaar voor zulke fundamentele studies en elektronische toepassingen. Idealiter hebben epitaxiaal gegroeide MgB_2 dunne lagen een T_c die de bulk waarde benadert. Dit betekent dat de depositie van zulke films bij hoge temperaturen (~ 600 °C) moet plaatsvinden. De hoge dampdruk van Mg, de lage adhesie coëfficiënt van Mg bij deze hoge temperaturen en de gevoeligheid van Mg en B voor zuurstof vereisen maatregelen om gladde films te produceren, die bovendien uit slechts één fase bestaan. Dit soort films zijn nodig voor meerlaags structuren die gebruikt worden voor supergeleidende elektronica.

De supergeleidende MgB_2 films die worden gepresenteerd in dit proefschrift zijn gefabriceerd volgens twee methoden: door middel van gepulste laserdepositie (*Pulsed Laser Deposition: PLD*) en door middel van hybride fysisch – chemische damp-depositie (*Hybrid Physical – Chemical Vapor Deposition: HPCVD*).

De films die gegroeid zijn volgens de PLD methode worden supergeleidend bij een tweestaps depositie proces: de film wordt gegroeid bij een lage temperatuur (kamertemperatuur of 200 °C), gevolgd door een gloeistap bij hoge temperatuur (600 °C). De films zijn gegroeid middels gebruikmaking van een Mg-rijk MgB_2 target of worden gegroeid als multilagen waarbij Mg en B targets zijn afgewisseld. De extra Mg en een hoge pulssnelheid van de laser zijn gebruikt om te compenseren voor het Mg verlies tijdens depositie, welke een gevolg is van het feit dat Mg gemakkelijk verdampt. De films die gegroeid zijn volgens deze methode hebben T_C waarden tot 28 K, wat vergeleken met bulk materiaal laag is. Dit is het gevolg van de kleine korrelgrootte van het MgB_2 (kleiner dan 5 nm), verontreiniging in het uitgangs-materiaal en MgO vorming in de films. De gemiddelde vrije weglengtes van de elektronen voor deze films bevestigen dat de films zich in de 'vuile' limiet bevinden. De geproduceerde films zijn polykristallijn en hebben een zeer kleine korrelgrootte en daarom is de keus van het substraat niet van invloed op de kwaliteit.

De verdamping van vast Mg en de hoge omgevingsdruk (~ 100 Torr) in de HPCVD methode leveren een hogere Mg flux op dan bij de PLD methode. Dit maakt het mogelijk om de supergeleidende films te maken in een éénstaps proces bij hogere temperatuur (~ 700 °C). Dit resulteerde in T_c waarden die overeenkomen met bulk materiaal. X-ray diffractie laat zien dat de films epitaxiaal groeien op zowel SiC als Al_2O_3 substraten. Omdat de roosterconstanten van MgB_2 en Al_2O_3 niet overeenkomen groeit de MgB_2 film onder een hoek van 30° ten opzichte van het Al_2O_3 substraat. Bovendien wordt volgens de literatuur MgO gevormd op het grensvlak tussen MgB_2 en Al_2O_3. Daarentegen groeit MgB_2 zonder rotatie op SiC omdat de roosterconstanten dichter bij elkaar liggen en is er geen reactie waargenomen op het MgB_2/SiC grensvlak. Beide films zijn voldoende glad (r.m.s. ruwheid was ~2.5 – 11 nm afhankelijk van het substraat), wat verdere structurering mogelijk maakt. De gemiddelde vrije weglengte van de elektronen laat zien dat deze films zich in de 'schone' limiet bevinden.

Om het potentieel te demonstreren van de implementatie van MgB_2 in elektronica en supergeleidende sensoren zijn PLD en HPCVD films gebruikt om zwakke koppelingen te maken. Deze zwakke koppelingen zijn gemaakt in de vorm van Josephson juncties en nanobruggen.

'Ramp-type' Josephson juncties gemaakt over een geëtste helling en gebaseerd op PLD films hadden een modulatie van de kritieke stroom in

magnetisch veld en verschijning van Shapiro stappen onder microgolf bestraling. Dit is een indicatie dat de korrelgrenzen bij polykristallijne films een sterke koppeling vormen, waarbij de supergeleidende fasecoherentie nauwelijks wordt beïnvloed. Verbetering van de eigenschappen van de juncties kan bereikt worden door gebruik te maken van epitaxiale films die T_C waarden hebben die vergelijkbaar zijn met bulk materiaal.

Om de eigenschappen te demonstreren van zwakke koppelingen in een epitaxiale film zijn nanobruggen gestructureerd (tot ongeveer 100 nm) in een HPCVD film. De kritieke stroomdichtheden van deze nanobruggen lagen in de orde van mid-10^7 A/cm^2 bij 4.2 K. Dit geeft aan dat deze dunne films en nanostructuren van zeer goede kwaliteit zijn.

SQUIDS gebaseerd op nanobruggen zijn gefabriceerd van zowel PLD als HPCVD films. De nanobruggen geprepareerd in de PLD films hebben kritieke stroomdichtheden van 7x10^6 A/cm^2 bij 4.2 K, wat aangeeft dat de films en nanostructuren goede supergeleidende eigenschappen bezitten. Spanningsmodulatie is waargenomen tot 20 K, zodat deze films bruikbaar zijn in combinatie met kleine cryokoelers. Ook de SQUIDs gefabriceerd van de HPCVD films hadden een kritieke stroomdichtheid van 5x10^7 A/cm^2 bij 4.2 K. Bovendien is spanningsmodulatie in magnetisch veld waargenomen tot een uitzonderlijk hoge temperatuur van 38.8 K. Dit maakt de toepassing van deze SQUIDS mogelijk tot ongeveer 30 K.

Het witte ruisniveau is gemeten aan een inductief geshunte MgB_2 SQUID magnetometer en bedraagt 76 $\mu\phi_0/\sqrt{Hz}$ in het frequentiebereik van 1 Hz tot 1 kHz. De effectieve magnetische fluxruis is 1 pT/$\sqrt{Hz}$ bij 34.5 K, hetgeen gevoelig genoeg is om een magnetocardiogram (MCG) van een volwassene te registreren. Dit eerste resultaat is veelbelovend voor het gebruik van MgB_2 dunne films in biomagnetisme studies.

Acknowledgments

I would like to thank all people who contributed to this work in different ways and whose help and support made the realization of this thesis possible.

First, I would like to express all my gratitude to my promotors, Prof. Horst Rogalla and Prof. Dave Blank for giving me an opportunity to do my PhD study at University of Twente in Low Temperature Division and MESA$^+$ Institute for Nanotechnology, to work with such a novel material as MgB_2 and thank for their trust in my ability to finalize this project. Dave, your ideas, experience and motivating suggestions helped me a lot in working with such an interesting compound.

I would like to thank my co-promotors, Guus Rijnders and Hans Hilgenkamp, for their encouragements, enthusiasm, help and support in these experiments, but also in overcoming the difficult moments that brings the last part of writing the thesis. Thank you also for the detailed reading and corrections on my thesis.

Special thanks to Prof. Xi, Alexej and Ben from Penn State University (USA), whose kindness resulted in a fruitful collaboration and my enjoyable visit of this University.

I would like to thank all members of Low Temperature Division with whom I shared pleasant times during these years, I have collaborated with and whose help was precious for the success of my experiments. Alexander, it was a pleasure working with you in the lab. Thank you for the great help in electronic measurements and the elucidating discussions. Sasha, your theoretical insight in

MgB_2 and enlightening discussions helped me a lot in understanding this material.

Frank, I am indebt to you for your technical help in working with pulsed-laser deposition systems and patience in adaptation of the system for the combined-PLD and sputter deposition techniques. Dick, thank you for your excellent job with FIB, electronic measurements, time spent working with me in the weekends and lots of valuable advices.

Victor, it was a pleasure sharing the office with you for several years and I would like to thank you for extending my chemistry knowledge, help in AFM and stimulating discussions. I am grateful to Gerrit and Sybolt for XRD, Ingrid and Victor Tan for help in electronic measurements and Harry for taking care of the liquid helium.

The measurements of the upper critical field of MgB_2 samples would not be possible without the willingness, assistance and kindness of the people from T2, especially Harald, Sander, Mark and Andries. Mark, the discussions with you about the results helped me very much in interpretation of them. Harald, thank you also for the help in translating Summary of my thesis in Dutch.

Ans and Inke thank you very much for all administrative work. It was nice seeing you always with a smile. I would also like to thank all other stuff members and graduate students.

Thanks also to Albert van den Berg from the Analytical Material Laboratory of $MESA^+$ for XPS measurements.

Louis, our discussion at COLA conference in Crete, Greece and your plasma-physicist experience helped me a lot in better understanding of an Mg and MgB_2 plasma.

I am grateful to my friends Irina and Francesca Romana for being my *paranimfen* at the dissertation ceremony and being supportive all the time. Special thanks to my friends Nataša, Chiara, Agnès, Irene, Caroline, Cristina, Laura, Betty, Crystal, Marijke, Danijela, Dessy, Lisa, Yuk, Victor, Tommaso, Charu, Javier, Harald, Dick, Richard, Niels, Zoran and Johannes for making my stay in the Netherlands enjoyable.

Желим да се захвалим родитељима и деди на свесрдној помоћи и подршци у свим лепим и тешким тренуцима током израде доктората. Хвала што сте увек били уз мене! Захваљујем се овом приликом Давору и Ивану на драгоценим саветима и Николи и Блажи на подршци и разумевању. Желим и да се захвалим тетки, сестрама, Димитријевићима и свим мојим пријатељима из Новог Сада, а посебно Ивани, Милици, Сандри, Александри и Саши што смо остали у контакту за сво време мог боравка у Холандији и што су учинили мој долазак у Нови Сад сваки пут врло пријатним.

List of publications

1. **D. Mijatovic**, A. Brinkman, H. Hilgenkamp, H. Rogalla, G. Rijnders and D.H.A. Blank, “Pulsed-laser deposition of MgB_2 and B thin films”, Appl. Phys. A, in press, (2004).

2. A. Brinkman, **D. Mijatovic**, H. Hilgenkamp, G. Rijnders, I. Oomen, D. Veldhius, H. Rogalla, and D.H.A. Blank, “The road to Magnesium-diboride thin films, Josephson junctions and SQUIDs”, Supercond. Sci. Technol. **16**, 246 (2003).

3. **D. Mijatovic**, A. Brinkman, I. Oomen, D. Veldhius, G. Rijnders, H. Hilgenkamp, H. Rogalla, and D.H.A. Blank, “MgB_2 thin films and Josephson devices”, IEEE Trans. on Appl. Supercond. **13**, 3245 (2003).

4. **D. Mijatovic**, A. Brinkman, I. Oomen, G. Rijnders, H. Hilgenkamp, H. Rogalla, and D.H.A. Blank, “Magnesium-diboride ramp-type Josephson junctions”, Appl. Phys. Lett. **80** (12), 2141 (2002).

5. **D. Mijatovic**, A. Brinkman, G. Rijnders, H. Hilgenkamp, D. H. A. Blank, H. Rogalla, “Superconducting thin films of MgB_2 by pulsed laser deposition”, Physica C **372-376**, 1258 (2002).

6. **D. Mijatovic**, G. Rijnders, H. Hilgenkamp, D. H. A. Blank, H. Rogalla, “Growth studies of $Ba_{1-x}(K_x)BiO_{3-\delta}$ thin films by pulsed-laser deposition”, Physica C **372-376**, 596 (2002).

7. A. Brinkman, D. Veldhuis, **D. Mijatovic**, G. Rijnders, D.H.A. Blank, H. Hilgenkamp, H. Rogalla, "Superconducting Interference Devices (SQUIDs) based on MgB_2 nanobridges", Appl. Phys. Lett. **79** (15), 2420 (2001).

8. D.H.A. Blank, H. Hilgenkamp, A. Brinkman, **D. Mijatovic**, G. Rijnders and H. Rogalla, "Superconducting Mg-B films by pulsed-laser deposition in an in-situ two-step process using multi-component targets", Appl. Phys. Letters **79** (3), 394 (2001).

9. A. Brinkman, **D. Mijatovic**, G. Rijnders, V. Leca, H.J.H. Smilde, I. Oomen, A.A. Golubov, F. Roesthuis, S. Harkema, H. Hilgenkamp, D.H.A. Blank and H. Rogalla, "Superconducting thin films of MgB_2 on Si by pulsed laser deposition", Physica C **353** (1-2), 1 (2001).

10. A. Omerzu, **D. Mijatovic**, D. Mihailovic, "Revealing of the re-entrant spin-glass phase in TDAE-C_{60} with linear and non-linear AC susceptibility measurements", Synthetic Met. **121** (1-3) Sp. Iss. SI Mar 15, 1155 (2001).

11. **D.B. Mijatovic**, Z.N. Popovic, J. Janjic, F. Skuban, M.I. Avramov, "Dissolution Rate of Some Chalogenides Containing Copper", Journal of Res. in Physics **28** (1), 81 (1999).

12. **D.B. Mijatovic**, Lj. Maskovic and M. Pantic, "Coefficient of Electron Diffusion in a Single-Crystal Thin Film", SPIE Proceedings 3841, Superconducting and Related Oxides: Physics and Nano-engineering III, (SPIE, Bellingham), 359 (1998).

13. **D.B. Mijatovic**, Lj. Maskovic and Z. Skrbic, "The influence of deformation on elastic properties of polymer materials", Solid State Phenomena **61-62,** 115 (Scitec Publication) (1998).

14. Lj. Maskovic and **D.B. Mijatovic**, "The role of solitons in biopolymers", Pol. Acad. Journal, Belgrade, Yugoslavia, **3** (1), 1 (1998).

15. B.S. Tosic, U.F. Kozmidis-Luburic, Lj. Maskovic and **D.B. Mijatovic**, "Long-wave range Electrons in Ultrathin Quantum Wires", Pol. Acad. Journal, Belgrade, Yugoslavia, **2** (2), 1 (1997).

16. Lj. Maskovic and **D.B. Mijatovic**, “The Dependence of Polymer Thermodinamic Properties on the Mass Distribution”, Pol. Acad. Journal, Belgrade, Yugoslavia, **2** (2), 15 (1997).